UC Berkeley
UC Berkeley Electronic Theses and Dissertations

Title

Structure and Dynamics of Cu and Cu-Ag Nanocrystal Catalysts during Electrochemical CO2 Reduction

Permalink

https://escholarship.org/uc/item/0f090711

Author

Osowiecki, Wojciech Tomasz

Publication Date

2019

Peer reviewed|Thesis/dissertation

Structure and Dynamics of Cu and Cu-Ag Nanocrystal Catalysts
during Electrochemical CO$_2$ Reduction

By

Wojciech Tomasz Osowiecki

A dissertation submitted in partial satisfaction of the

requirements for the degree of

Doctor of Philosophy

in

Chemistry

in the

Graduate Division

of the

University of California, Berkeley

Committee in charge:

Professor A. Paul Alivisatos, Chair
Professor Peidong Yang
Professor Alexis Bell

Spring 2019

Structure and Dynamics of Cu and Cu-Ag Nanocrystal Catalysts
during Electrochemical CO_2 Reduction

Copyright 2019

By

Wojciech Tomasz Osowiecki

Abstract

Structure and Dynamics of Cu and Cu-Ag Nanocrystal Catalysts
during Electrochemical CO_2 Reduction

by

Wojciech Tomasz Osowiecki

Doctor of Philosophy in Chemistry

University of California, Berkeley

Professor A. Paul Alivisatos, Chair

In recent years, the CO_2 reduction reaction (CO_2RR) has been a popular topic in the field of electrocatalysis for its potential to help in mitigating climate change effects. As renewable energy sources such as solar and wind are rising in the market, there is a growing need for energy storage due to the intermittency of production. Renewable energy can be stored in batteries, but chemical bonds offer energy densities that are orders of magnitude higher. CO_2 reduction is one of the electrocatalytic reactions that can store electrons in chemical bonds, simultaneously decreasing the amount of harmful greenhouse gas and creating useful fuels and chemical feedstocks. However, this vision is only possible if new catalysts for CO_2 reduction are developed, because currently the efficiency and selectivity of the reaction are not high enough to allow for an industrially-viable technology.

Due to the fundamental restrictions between the bonding strengths of CO_2RR intermediates, complex nano-engineered catalysts are particularly well suited for achieving substantially better catalytic selectivity as compared to state-of-the-art Cu bulk materials. Creating high-energy facets with low-coordination atoms as well as alloying Cu with other metals are among widely pursued strategies, and for such objectives, we find small (<10 nm) synthetically-tunable nanocrystals to be promising candidates. That said, industrially-viable catalysts must not only be efficient and selective but also stable. Ironically, the very properties that offer favorable catalytic performance also render the material prone to morphological restructuring, namely sintering, under the operating conditions. We believe that in order to prevent sintering in the future, it needs to be studied first, so we directly focus on this issue by systematically probing the reaction conditions during electrocatalysis. We hope that this topic will be further investigated as the complexity of the experimental parameters calls for efforts of the same magnitude as to what has been done to understand the CO_2RR selectivity and reaction mechanism.

Chapter 1 discusses the opportunities and challenges of electrocatalysis in the 21st century. We draw some analogies to other fields where an understanding of the theoretical limits as well as an ambitious pursuit of chemical reaction control were needed to create industrially-viable technologies. We then motivate the need of for a fundamental understanding of morphological changes occurring during electrocatalysis in light of these considerations.

Chapter 2 describes the synthesis, characterization, and thermodynamic understanding of different morphologies of Cu-Ag bimetallic nanocrystals. Cu and Ag do not alloy, so the bulk Cu-Ag materials used for catalysis possess monometallic domains of a specified size, but with nano-colloidal synthesis, it is possible to bring Cu and Ag into a more intimate contact which may give rise to a change in material properties. As such, we have synthesized a new structure, the nanocrescent, and its formation, based on thermodynamic principles, is explained.

Chapter 3 presents the catalytic performance of Cu-Ag bimetallic nanocrystals for CO_2RR and compares it with that of physical mixtures of monometallic Cu and Ag particles. This chapter illustrates precisely why an understanding of sintering and its prevention are crucial, as the studied structures undergo a complete morphological restructuring and can no longer be confidently distinguished as distinct particles. Nevertheless, we observe a significant shift in catalytic selectivity as compared to pure Cu nanocrystals. Cu-Ag materials decrease the activity towards undesired H_2 production and increase the efficiency of oxygenates formation.

Chapter 4 focuses directly on the issue of electrochemical sintering by studying the behavior of Cu nanocrystals under the standard conditions of CO_2RR as well as a range of control experiments. We hypothesize some possible driving factors that could lead to the morphological restructuring and aim at distinguishing between them by changing variables such as the gas environment or pH. Ligand presence is probed with spectroscopic techniques, and morphological structures are imaged with electron microscopy. The presented set of evidence demonstrates that CO, a CO_2RR intermediate, plays an important role in the sintering process by changing nanoparticle surface properties, leading to the formation of larger single-crystal facets.

To my loving wife, parents, and sister.

Table of Contents

List of Figures

List of Tables

Acknowledgements

Everyone says that getting a Ph.D. is hard, but I wish I had embraced this truth a bit earlier in my graduate career. As I look back, I see plenty of struggle that might have been reduced if I was more willing to accept life as it is. Regardless, this time has been marked by tremendous personal and scientific growth enabled by friends, mentors, and colleagues. I am grateful to belong to the UC Berkeley community and embrace it with all of its flaws and imperfections.

I want to thank my advisor, Paul Alivisatos, for turning me into an independent scientist and thinker, even at the cost of countless frustrations and mistakes. I admire him for genuinely believing that the journey matters more than the destination as well as for his exceptional scientific intuition and perceptiveness. This dissertation would also not have been possible without the mentorship of Alexis Bell who taught me about the chemical engineering knowledge necessary for my project and who welcomed me to his student community. I learned a lot from them.

I have been assisted and supported by so many people that I cannot list them all, but I would like to mention a few that stand out in my memory: Xingchen Ye, Jacob Kanady, Wendy Gu, Ezra Clark, Peter Lobaccaro, Karthish Manthiram, and Karen Bustillo. All of them took their time to help me, although I was at the beginning of my career and could not contribute similarly to their work. I am thankful for their generosity.

My work would not have been completed without a few undergraduate students whom I had the privilege to mentor: David Koshy, Richard Lin, Gaurav Kamat, and Jasper Nussbaum. In my opinion, research should always be a collaborative effort, and I am glad that I could share this experience with them.

Naturally, my journey was greatly influenced and enriched by my friends and family. I thank Chris Kaplan, Steven Lyle, and Tom Osborn Popp for being there for me from the very beginning of graduate school. I am grateful for my family in Poland, always supporting me and willing to listen to innumerable stories of research struggles. But most importantly, I feel incredibly lucky to meet and to fall in love with my now wife, Pratima Satish. She has been a source of constant support, and I would not hesitate to go through the last five years again if only to be with her.

Chapter 1. Introduction: The need for fundamental understanding of morphological changes occurring during electrocatalysis

Reproduced in part with permission from: A. Paul Alivisatos and Wojciech T. Osowiecki, "Introductory Perspectives." In *Electrochemical Engineering: From Discovery to Product*; Alkire, R. C., Bartlett, P. N., Koper, M., Eds.; Advances in Electrochemical Sciences and Engineering; Wiley-VCH: Weinheim, 2019; pp 1–5. Copyright 2019 by Wiley.

1.1 Electrocatalysis in the 21st century

The challenges of the current world dictate opportunities for researchers, especially those interested in seeing their work incorporated in significant technological innovations of the future. In the 21st century, supplying energy to the ever-growing global population in a sustainable manner is, without doubt, one of the most critical issues. Nowadays, the vast majority of energy is derived from fossil fuels whose combustion and release of carbon dioxide into the atmosphere are amongst the primary causes of perilous global climate change.

Fortunately, there are a growing number of renewable energy sources decoupled from environmentally costly fossil fuel combustion, such as solar and wind, coming up on the market (Figure 1.1). In this new economy, scientists should be encouraged to think of electrons as crucial and readily available chemical reagents. Just like the fossil fuel industry turned oil into a ubiquitous precursor to many compounds and products, now electrons will be involved in crucial processes such as fuel generation and energy storage. Indeed, the ability to store energy in chemical bonds solves one of the greatest challenges for renewables, namely their transience. As opposed to conventional coal and gas-fired power plants, solar cells and wind turbines are bound by daily and seasonal production cycles. While many propose to stabilize the electric grid with batteries, it should be remembered that chemical bonds store energy 100 times more efficiently than modern-day batteries.[1]

Furthermore, transportation and chemical industries remain one of the most challenging sectors for decarbonization due to their mobility and high energy demand, respectively. Marine, aviation, rail, and heavy-duty road vehicles are especially difficult to electrify. This challenge presents itself as a big opportunity for processes that can store electrons in chemical bonds and allow quick energy release on demand, i.e., fuel production.[2] Instead of digging up fossil fuels from the ground, the same chemicals can be created using renewable electricity in various electrocatalytic processes.

Annual electricity generating capacity additions and retirements
gigawatts
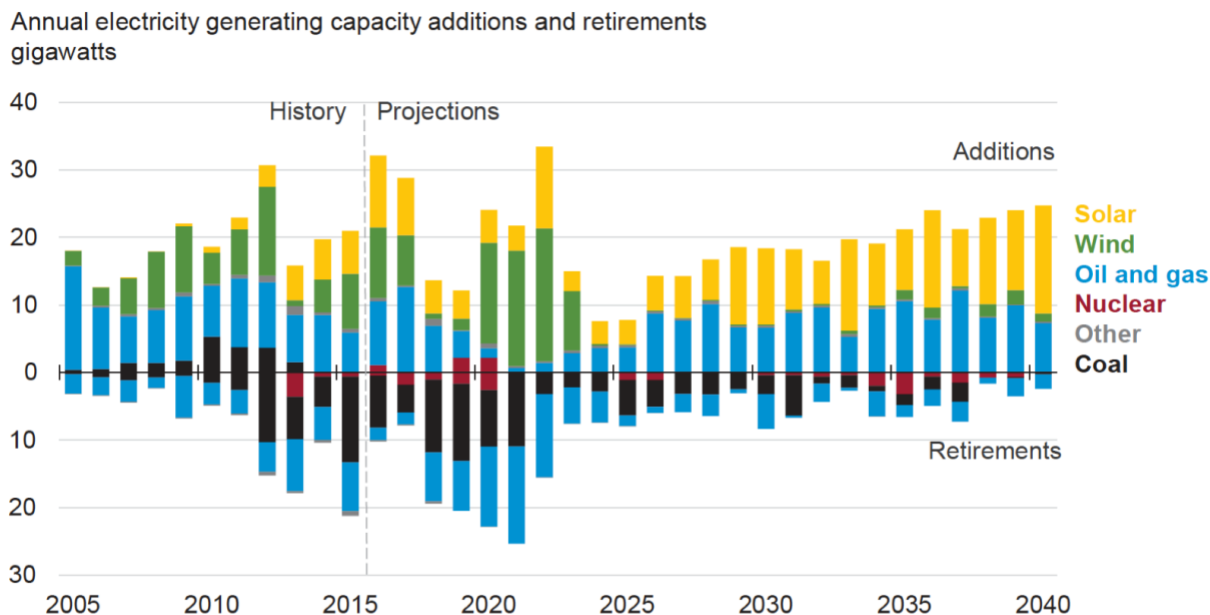
U.S. Energy Information Administration   #AEO2017 | www.eia.gov/aeo

Figure 1.1. Annual electricity generating capacity additions and retirements
Most of the wind capacity is expected to be built before the scheduled expiration of the production tax credit in 2023, although wind is likely to remain competitive without the credits. Substantial cost reductions and performance improvements strongly support continuous solar generation growth. Source: U.S. Energy Information Administration (2017).

Electrocatalysis can be defined as electrochemical reactions that start from dissociative chemisorption or a reaction step in which the surface of the electrode is involved.[3] There are many similarities between heterogeneous catalysis and electrocatalysis, but the latter always involves an electrolyte and requires an applied electric potential that affects reaction rates and the electrochemical double-layer.[4] Every electrochemical process must involve both reduction and oxidation to balance the charge transfer. Reduction occurs on the cathode and oxidation occurs on the anode. The simplest example of an electrocatalytic reaction that can be used for fuel production is water-splitting.[5] Potential applied to both electrodes changes the electronic properties of the electrode surfaces allowing for the binding of the reaction intermediates that will turn into products: H_2 and O_2. H_2 production is often called a hydrogen evolution reaction (HER; $2H^+ + 2e^- \rightarrow H_2$) and O_2 production is called oxygen evolution reaction (OER; $2H_2O \rightarrow O_2 + 4H^+ + 4e^-$).

1.2 Electrochemical CO_2 Reduction

While water splitting is the simplest system that could allow for storing electrons in chemical bonds as fuel, hydrogen has the lowest volumetric energy density, and its storage, especially for mobile applications, remains problematic.[1] Carbon dioxide conversion presents itself as an interesting alternative because reducing CO_2 can lead to more energy-dense and profitable products, such as ethylene, ethanol or methanol. Furthermore, fossil fuel combustion has released a dangerous amount of CO_2 into the atmosphere over the centuries and combining the need for energy storage with the ability to use CO_2 as a useful reagent is very appealing.[6] If

executed appropriately, one can envision a carbon-neutral economy that allows for some fossil fuel combustion as long as it offset by a subsequent conversion of CO_2 into useful chemicals and fuels using available renewable electricity (Figure 1.2).
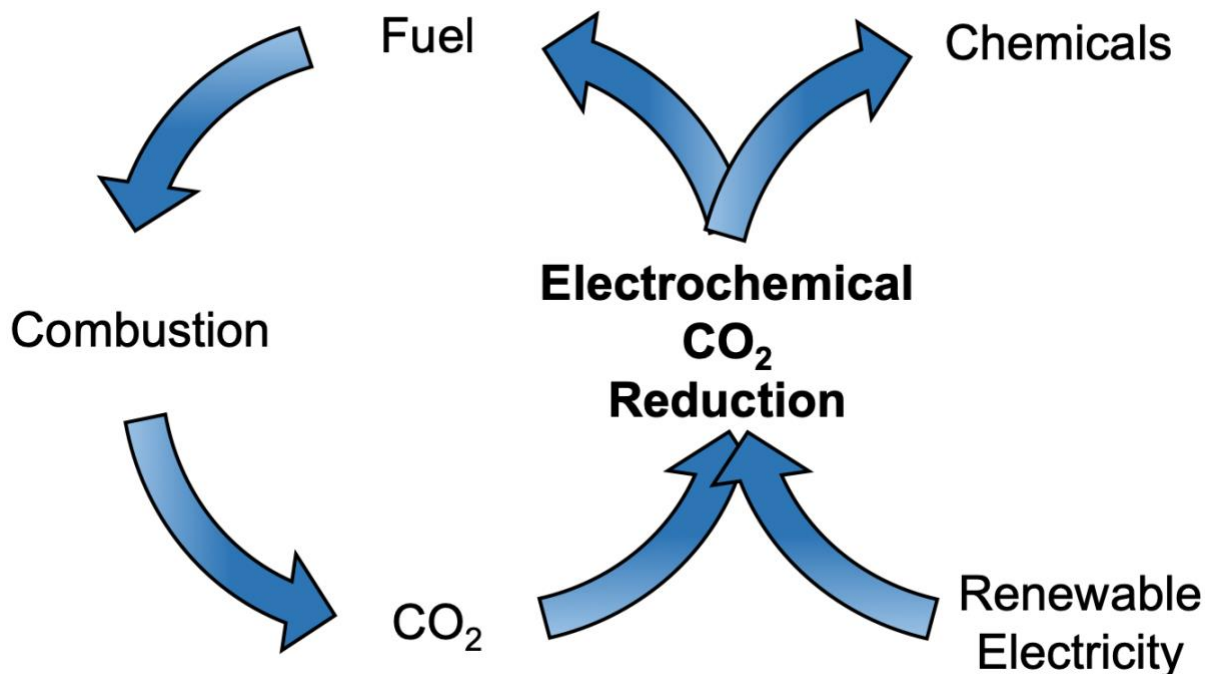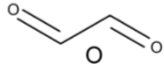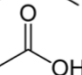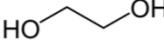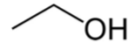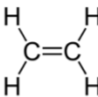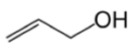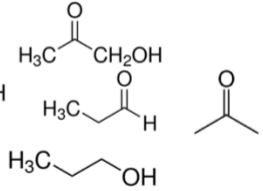
Figure 1.2. Carbon-neutral cycle
By utilizing electricity from renewable sources such as solar and wind, electrochemical CO_2 reduction can convert the greenhouse gas back into useful fuels and chemicals, providing for necessary energy storage and addressing climate change.

As opposed to H_2O, CO_2 can be reduced into several different chemicals, which presents itself as a big challenge and a big opportunity of this reaction. As the ultimate goal is the creation of an industrially-viable process, one needs to consider the issues of profitability and practicality while choosing the optimal products. To start with, we can consider how many electrons it takes to make a given molecule, the resulting energy density, the cost and the market size. Overall, at least 16 different products have been reported in the literature[7] and they are often divided by the number of carbon atoms contained in the molecule: C_1, C_2 or C_3 (Table 1.1). It turns out that C_2 and C_3 species are significantly more profitable than C_1 and two chemicals seem particularly enticing: ethanol as liquid fuel and ethylene as a precursor to many other materials. Both are widely used in the industry and with the right economics as well as reaction efficiency, they would be cheaper than current sources.[6]

Table 1.1. Products of CO₂ reduction along with the number of electrons needed to produce each one and the number of containing carbon atoms

e^-	C_1	C_2	C_3
2	CO HCOOH		
4	HCHO		
6	CH_3OH		
8	CH_4		
10			
12			
14			
16			
18			

An industrially-viable version of electrochemical CO₂ reduction reaction (CO₂RR) requires gas-phase electrolyzers, which are not limited in their output current densities by the solubility of CO₂ in water.[8] However, for lab-scale testing that focuses on catalyst development and fundamental understanding on the reaction, a water-based system can be appropriate, primarily for its relative simplicity and a better ability to study the surface of the catalyst (Figure 1.3). Gas-phase systems require a so-called triple interface, where a catalyst interacts simultaneously with the electrolyte and the gas stream, which is harder to probe experimentally and model theoretically.
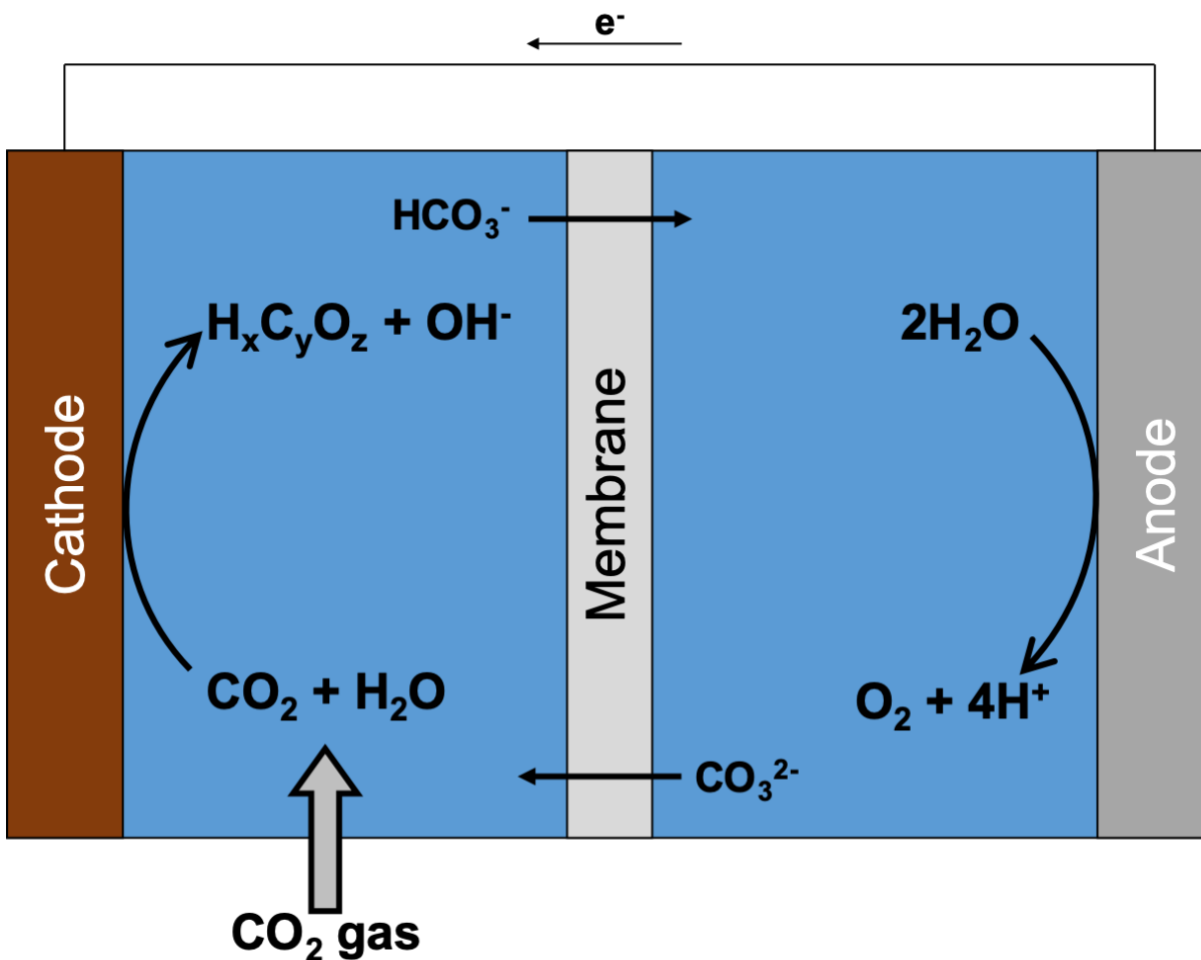
Figure 1.3. Schematic illustration of a lab-scale CO₂ reduction cell
Electrolyte solution contains a bicarbonate buffer to stabilize pH at around neutral, which is an optimal region for the catalytic conditions as well as the stability of many tested catalysts.[9]

1.3 Breaking the scaling relationships: a need for nanostructured catalysts

In electrocatalysis, the results are dramatically shaped by the properties of the catalytic surface, and CO₂RR is no exception. While C_2 and C_3 products are most enticing from a techno-economic standpoint, there is only one metal that has been shown to catalyze their production: copper. While practically all viable elements have been tested for CO₂RR reactivity, the other metals either do not produce anything or can only yield two-electron reduction species: carbon monoxide and formate.[10] The reason for the unique behavior of Cu surfaces is exemplary in understanding the crucial factors determining electrocatalytic selectivity and activity. Cu happens to have a near-optimal, intermediate binding energy to CO, a crucial CO₂RR intermediate, necessary to create all other products except formate.[11] As CO₂ gets reduced to CO, it can either bind too strongly to the surface, poisoning it and stopping further activity, or it can immediately detach from it because the interaction with a given metal is too weak. Cu, however, binds CO in the appropriate regime that allows for further reduction as well as C-C coupling required for the formation of C_2 products.[12] The principle of maximum electrocatalytic activity occurring for the

regime when binding is neither too weak nor too strong is often called the Sabatier principle and illustrated by the so-called "volcano plots" (Figure 1.4).
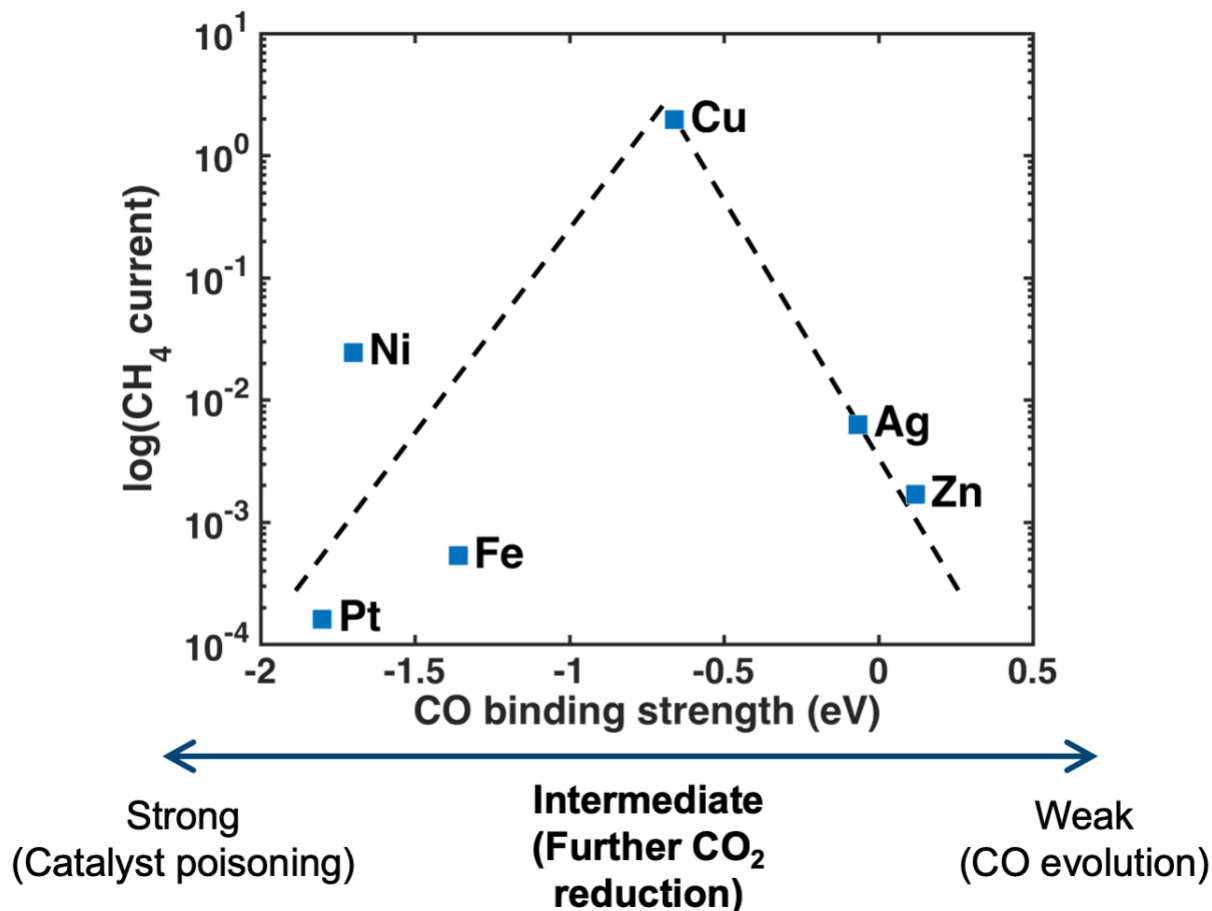
Figure 1.4. Binding strength of CO to various metals illustrating the "volcano plot"
CO binding strength can elucidate catalytic activity, represented here as current density in mA/cm², to further-reduction products such as CH₄. Binding strength data re-plotted from Kuhl et al.[13]

While Cu catalyzes the production of a variety of useful chemicals, it, unfortunately, yields them all simultaneously, with poor selectivity, due to the complexity of the multi-step multi-electron processes. In an industrial setting, the separation cost of these products would be prohibitively expensive and wasteful, creating a need for more controllable and efficient Cu-based catalysts.

In our belief, in order to achieve the desired goal of high selectivity towards a single C_2 product, one should primarily focus on two issues: 1) *theoretical efficiency limits*, and 2) *control*. We find useful analogies between the field of CO_2 reduction and other fields focused on getting the most out of materials: solar cells, batteries, or photoluminescent nanocrystals (NCs). In all these cases the first discoveries showed very modest performance, but it was crucial to probe the fundamental theoretical limits in order to understand whether a further scientific investment will pay back by eventually surpassing already-existing technologies and creating new markets. Solar cell efficiencies are always compared to the famous Shockley–Queisser (SQ) limit.[14] Although it

concerns only a single p-n junction, the number of 33% has motivated researchers and engineers to search for continuous improvements. Likewise, by performing thermodynamic analysis, one can understand what materials are most promising for future battery research.[15]

In electrochemistry, theoretical efficiency limits can be calculated using standard reduction potentials.[4] From the perspective of thermodynamics, conversion of carbon dioxide to fuels such as ethanol should not be very energetically costly. For example, the standard reduction potentials for ethanol and ethylene are +0.09V and +0.08V vs. RHE, respectively.[7] In reality, a large (> 0.8 V) overpotential, η, is needed to obtain an appreciable amount of reaction products, leading to electrochemical energy conversion efficiencies of less than 30%.[16,17] From a theoretical standpoint, the overpotential originates from the relative stability of various adsorbed intermediates.[18,19] Overpotential is formally defined as the difference between the thermodynamically determined standard reduction potential, U_{eq}, and the potential at which the reaction is experimentally observed, U_{expt}.[4] It can be also described as the most positive free energy change, ΔE_{max}, at the rate-determining step during one of the charge transfers between reaction intermediates[20], such that:

$$\eta = U_{eq} - U_{expt} = U_{eq} + \frac{\Delta E_{max}}{e} \tag{1.1}$$

where e is the elementary charge. The relationship between current and applied potential is described by the Butler–Volmer equation, which simplifies to the Tafel equation for large η, as in the case of CO_2 reduction:[4]

$$\eta = A \log\left(\frac{i}{i_0}\right) \tag{1.2}$$

which shows an exponential relationship between the observed current, i, and the applied overpotential, with A being the Tafel slope dependent on how many electrons participate in the rate-determining step and i_0 the exchange current.

The substantial overpotential required to conduct the reaction shows that the state-of-the-art Cu-based materials are still far from being the most optimal catalysts for CO_2RR. When there is only one crucial intermediate, such as H* for hydrogen evolution reaction (i.e., $2H^+ + 2e^- \rightarrow$ H_2), it is possible to finetune its adsorption and desorption strengths on the catalyst such that $\eta \approx$ 0.[2] However, as there are many intermediates present during CO_2RR,[12,21] it is impossible to optimize the binding property of one without affecting all the others, because for d-band metals, the binding strengths generally correlate linearly.[22] This phenomenon has been called the "*scaling relationships*".

If there is no single element that displays the optimal binding strength to all relevant intermediates, the only hope of ever achieving a significantly better efficiency for CO_2RR lies in attempts of breaking the scaling relationships. This approach ties into the goal of having an atomistic control over the catalysts where relevant active sites are nano-engineered to possess the desired properties and an ability to change the reaction kinetics of the successive steps, somewhat similar to the remarkable precision of enzymes. The linear relationships between the binding of species like *CO, *CHO, or *COOH can in principle be modified by using a nanocrystal catalyst

with unusual surface motifs, such as low coordination numbers,[23,24] high-energy facets,[25,26] alloying,[18,27,28] or tethered active ligands.[11,18,29] The other potential advantages of using nanocrystals catalysts are high surface area and the ability to disperse them onto three-dimensional mesh supports that will be required for current densities on the order of 1 A/cm^2 expected for an industrially-viable technology. Overall, the field of CO_2RR can achieve efficiency closer to the theoretical thermodynamic limit only with the use of highly engineered and optimized nano-structures.

1.4 Catalyst change, deactivation, and loss of control

While precise nano-engineering is required to break the scaling relationships and achieve significantly more selective and efficient CO_2RR catalysts, the need for control over the material does not end with its synthesis. Catalysis is inherently a dynamic process, and invariably all catalysts will deactivate, on time scales ranging from seconds to years.[30] That being said, the deactivation rate is a crucial factor of determining an actual value of a material for an industrial process, and it must not be disregarded. As such, special attention shall be paid to all changes occurring to catalysts, as without proper understanding, there is little hope of preventing or delaying the deactivation.

Unfortunately, the very properties that make nano-structures promising for electrocatalysis, such as high-energy facets and coordinatively-unsaturated atoms, make them extremely prone to morphological restructuring and deactivation under catalytic conditions. In cases such as CO_2 reduction, there is enough energy provided to the system that it pushes towards more thermodynamically-favorable states, namely less surface area and higher coordination numbers. The process of such morphological change has been commonly described in the literature as *sintering*.[31-33]

Sintering has often been associated with high-temperature processes operating for an extended period of time, but, perhaps surprisingly, it can occur at room temperature in electrocatalytic systems. Strong electric field shifting the redox potential, just like temperature, can provide enough energy into the system to induce its reconstruction (likewise, electrochemical cell potentials depend on temperature).[34] It has been observed for systems such as proton exchange membrane fuel cells, and as these devices use very expensive Pt nanoparticles, it is considered a severe problem.[35,36] For Cu-based nanocrystals, the restructuring has also been observed under a variety of catalytic conditions, often with the help of *in situ* studies,[37-39] but for some reason, it has not been investigated as much in the CO_2RR literature despite being routinely noted, especially for objects smaller than 10nm in diameter.[40-42] As the morphological change invariably modifies the properties of the catalyst, likely in an unwanted way, we believe that the phenomenon of electrochemical sintering under CO_2RR conditions deserves more attention and should be probed for mechanistic understanding. Only with deepened understanding, we can hope to meet extremely ambitious demands placed on a material to make it capable of converting CO_2 into a C_2 product with high efficiency, selectivity, and stability.

1.5 Cu-based bimetallic catalysts for electrochemical CO_2 reduction

As discussed in Section 1.3, Cu is the most versatile and promising catalyst for industrially-viable CO_2 reduction being the only metal that generates of C_2 and C_3 products in any appreciable amount. Nevertheless, the efficiency and selectivity observed on Cu catalysts are still far from industrial expectations. One of the most promising ways of improving the catalytic performance has been mixing Cu with other metals in the hope of breaking the scaling relationships between binding energies of relevant intermediates.[43] Bringing a secondary metal can change the chemical environment of Cu atoms and modify the surface binding propensity towards hydrogen and oxygen (Figure 1.5). As the continued interaction of bound *CO is necessary for the production of C_2 and C_3 species, a site that favors H and O bonding can stabilize desired *CHO or *COH intermediates. In effect, a scaling relationship between *CO and *COH/*CHO absorption observed for monometallic surfaces can be broken.[43]
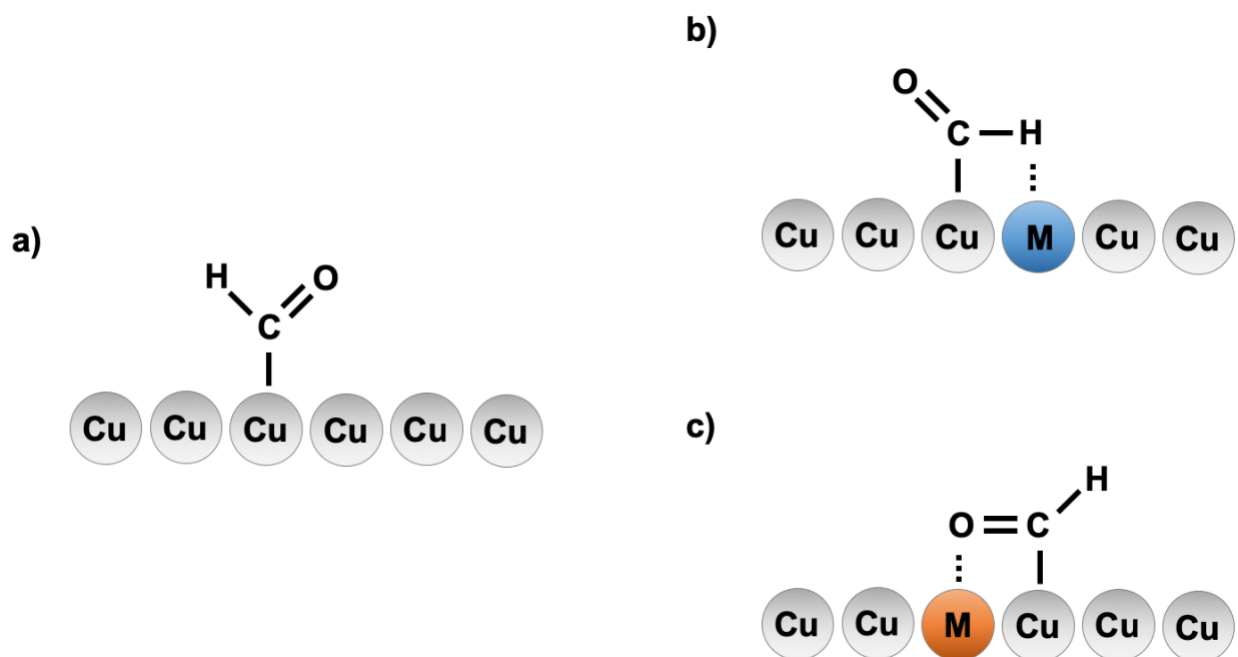
Figure 1.5. Schematic illustration of *CHO binding
*a) pure Cu surface b) bimetallic surface with a metal that has stronger H binding that Cu does c) bimetallic surface with a metal that has stronger O binding that Cu does. For b) and c), the binding of *CHO is enhanced as compared to a)*

The scaling relationships can also be broken by adding a metal with lower binding strength to both H and O. While potentially counter-intuitive, the addition of Ag has been reported to increase the selectivity of CO_2 reduction past CO and to improve the production of C_2 and C_3 species over C_1.[17,44–46] Most of the proposed mechanisms of this catalytic enhancements can be divided into two categories: 1) tandem and 2) electronic and strain effects (Figure 1.6).
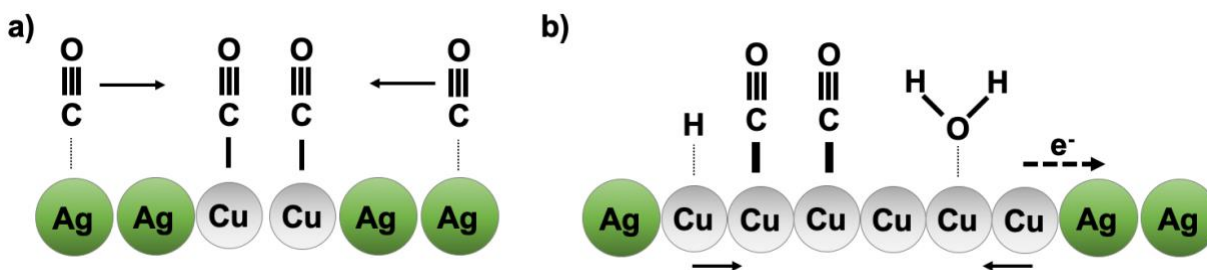
Figure 1.6. Schematic illustration of catalytic enhancement from mixing Cu with Ag
a) Tandem effect. CO generated on Ag moves to Cu due to binding differences. b) Electronic and strain effects can change Cu binding energies for important intermediates such as CO as well as competitors like H_2O.

The tandem effect, also known as the spillover effect, is perhaps easiest to rationalize. Since Ag has very weak binding to CO and will not reduce the molecule further, CO will detach from the surface and can theoretically be attracted towards Cu with stronger binding energy to it. As the higher concentration of Cu increases the chances of C-C coupling, a source of CO shuttled towards the catalyst should improve the production of C_2 species over C_1 as well as increase the overall process efficiency. This explanation has been used by some researchers,[47,48] while others claimed to find no evidence of such a mechanism.[45]

In the absence of the spillover effect, one can propose that the presence of Ag modifies the intrinsic binding properties of nearby Cu atoms. Clark *et al*. conducted careful X-ray studies to propose that the Cu-Ag surface is strained by the larger Ag atoms.[45] Such strain would lead to a decrease in oxophilicity and favor binding of CO over H_2O, which could explain the decrease in H_2 production observed for Cu-Ag electrodes. An alternative hypothesis for the modification of binding energies is the electron transfer between Cu and Ag, which makes Cu atoms electron-depleted and could also be responsible for the enhancement in CO binding.[49] The last hypothesis for the superior catalytic performance of Cu-Ag catalysts proposes the stabilization of Cu_2O due to Ag electronegativity.[46] Cu_2O is supposed to produce more C2 products than Cu(0), but such observed effects have always been transient as invariably Cu will reduce to the metallic state under the applied negative bias required for the CO_2 reduction, even in the presence of Ag atoms in the vicinity.

While the presence of Ag in Cu-based CO_2 reduction has been shown to be beneficial, it is important not to forget that Cu and Ag do not form a proper alloy. As such, in all bulk materials, there are phase-pure domains of Cu and Ag that are routinely 10nm or larger.[45] Nanostructuring of the surface could offer a higher degree of control over the catalysis in order to improve the efficiency and selectivity. A synthesis of Cu-Ag bimetallic nanocrystals with monometallic domains that are smaller than the bulk limit of 10+ nm, such as the one described in Chapter 2, could allow for probing whether the size of Cu and Ag domains matters significantly for the catalysis and whether we observe more behavior deviating from the expectations set by pure Ag and Cu foils, which will be discussed in Chapter 3.

Chapter 2. Synthesis and thermodynamic analysis of Cu-Ag nanocrystals

2.1 Cu-Ag bimetallic nanomaterials

The physical properties of metals, such as binding energies or plasmon resonance, can be significantly modified by forming nanoscale alloys and intermetallics.[50,51] While there are many theories developed for predicting the stability of a given bulk alloy as well as its structural and electronic properties,[52,53] the behavior of nanomaterials cannot be understood without considering surface and interface effects.[54] From a theoretical standpoint, bimetallic nanocrystals are particularly intriguing and challenging due to the complexity of the formation energy landscape. Atoms of two metals order in a variety of patterns, ranging from single-phase homogeneous systems with either random or ordered mixing to multi-phase heterogeneous systems with segregated domains. The segregation can be further differentiated into structures, where atoms either order in uniform layers such that only one metal is present on the surface (core-shell) or instead form regions of many components present on the surface (e.g., bifacial Janus particles).[55] Hence, the ability to predict, and ideally control, the formation of segregated systems is crucial for surface-specific applications.[28]

We report the synthesis, characterization, and theoretical considerations of a new family of stable, monodisperse, and solution-processed Cu-Ag bimetallic nanoparticles (NPs) with controlled atomic arrangement. These include the formation of Cu/Ag nanocrescents that, to the best of our knowledge, have not been observed before. High-resolution electron microscopy combined with elemental (EDS) mapping was applied to resolve the location of Cu and Ag within each of the structures. The bulk Cu-Ag system has been the subject of numerous phase-stability calculations, and is representative of segregated alloys with positive enthalpy of mixing.[56] Additionally, Cu-Ag bimetallic nanoparticles find applications in such fields as catalysis[57,58] and printed electronics.[59] As such, we decided to investigate whether the formation of bimetallic NCs of Cu and Ag can be predicted with a simple thermodynamic model focused on surface and interface effects. We have revisited models studying wetting in multiphase systems[60–62] to probe how the geometry of Cu and Ag domains in a nanoparticle is primarily determined by the ratio of surface and interface energies. Here, surface energy refers to the energy needed to create a boundary between a solid and a vapor,[63] while interface energy is the cost to create an interface between two different solids.[64] By combining experimental results with a simple theoretical treatment, we hope to develop design principles for achieving desired geometries of binary NCs.

Cu-Ag bimetallic nanoparticles have been previously synthesized using pulsed laser deposition,[65] microwave irradiation,[66] and wet chemistry, both in aqueous[67] and organic[68,69] solvents. However, in most of these cases, the reports describe only one geometry of nanoparticles, either core-shell[59,68] or bifacial,[69,70] under the implicit assumption that there should exist one equilibrium product for the Cu-Ag bimetallic NC. Here, we present synthetic conditions that can

produce multiple surface configurations: Ag only (core-shell), both Cu and Ag (crescent), and Cu only (as Cu_2O in an inverted core-shell). We also demonstrate that these various geometries are expected to occur at equilibrium, given specific and reasonable ratios of surface and interface energy values. An Organic-based synthesis was chosen, as it results in small (~7nm) nanoparticles, which emphasizes surface effects. Furthermore, the growth process was split into two steps to achieve better control over the system and to develop a more universal synthetic scheme. First, Cu particles were synthesized, and afterward, Ag salt was added to induce galvanic exchange at low (<100 °C) temperatures. Galvanic exchange is driven by the reduction potential between Cu and Ag, since Cu atoms are readily oxidized and replaced in the nanoparticles by reduced Ag.[71]

Galvanic exchange has been used for the synthesis of Cu-Ag nanoparticles before, yielding either core-shell[68] or clustered[69] geometries. What drives the choice between the two morphologies has not been explored previously. High-resolution STEM-EDS mapping under conditions that carefully exclude oxygen and avoid any air exposure is important, if not essential, for unambiguous identification of the location and Cu and Ag within the bimetallic nanomaterials. Cu readily oxidizes to Cu_2O, and this transformation is accompanied by significant restructuring of the particles. While it is possible to measure d-spacing from high-resolution TEM images, the d-spacing of Cu(111) and Ag(200) differ from each other by less than 0.05 Å, introducing substantial uncertainty into resolving HRTEM images. Using air-free STEM-EDS, we were able to unambiguously resolve the formed structures and separate the influence of oxidation on the morphology. Based on the temperature, two oxidized products were obtained, differing in particle geometry and the amount of Cu_2O.

2.2 Cu-Ag crescent and core−shell particle formation via galvanic exchange

Cu-Ag bimetallic particles were formed via a two-step process: 1. organic-based synthesis of Cu particles, 2. galvanic exchange of Cu with an Ag-containing salt. Dividing the synthetic process into two steps gave us significantly higher control over the morphology, as compared to simultaneous reduction of Cu and Ag precursors. Since Cu and Ag do not alloy in the bulk and the interface energy between these two metals is positive, it is important to avoid homogeneous nucleation that would lead to the formation of separate Cu and Ag nanoparticles. This was achieved by conducting galvanic exchange in ether, a non-reducing solvent.

The first reaction step was the synthesis of 7 nm tetradecylphosphonate-capped Cu nanoparticles following a previously published protocol.[72] (see Section 2.7.3 for more details) For the second reaction step, galvanic exchange, both Cu particles and Ag precursor needed to be soluble in the same solvent. Isoamyl ether was selected, because it does not reduce copper or silver ions, and it dissolves both TDPA-capped Cu nanoparticles and silver trifluoroacetate. In the absence of any other reducing agent, Ag^+ ions can only react with Cu^0 in the prepared solution. All reaction steps were performed under the protective argon atmosphere, either on a Schlenk line or in a glovebox, in order to prevent any Cu oxidation. Ag TFA is known to thermally decompose at approximately 120 °C.[73] Since we wanted to avoid the possibility of Ag homogeneous nucleation, this set a temperature limit for the galvanic exchange.

The incorporation of Ag into Cu particles was probed with two techniques: inductively coupled plasma optical emission spectrometry (ICP-OES) and electron microscopy. ICP-OES can determine the bulk ratio of Cu and Ag in the tested samples but does not provide information on the spatial arrangement of the two materials. To unambiguously analyze the morphology and elemental composition of products, high-resolution TEM and STEM-EDS elemental mapping were employed with care to ensure no exposure to oxygen or air (Figure 2.1). For all presented STEM-EDS maps, the average Cu:Ag ratio was consistent with the one obtained from ICP-OES (less than 5% discrepancy, Table 2.1), corroborating that the results presented here are representative of the entire sample.
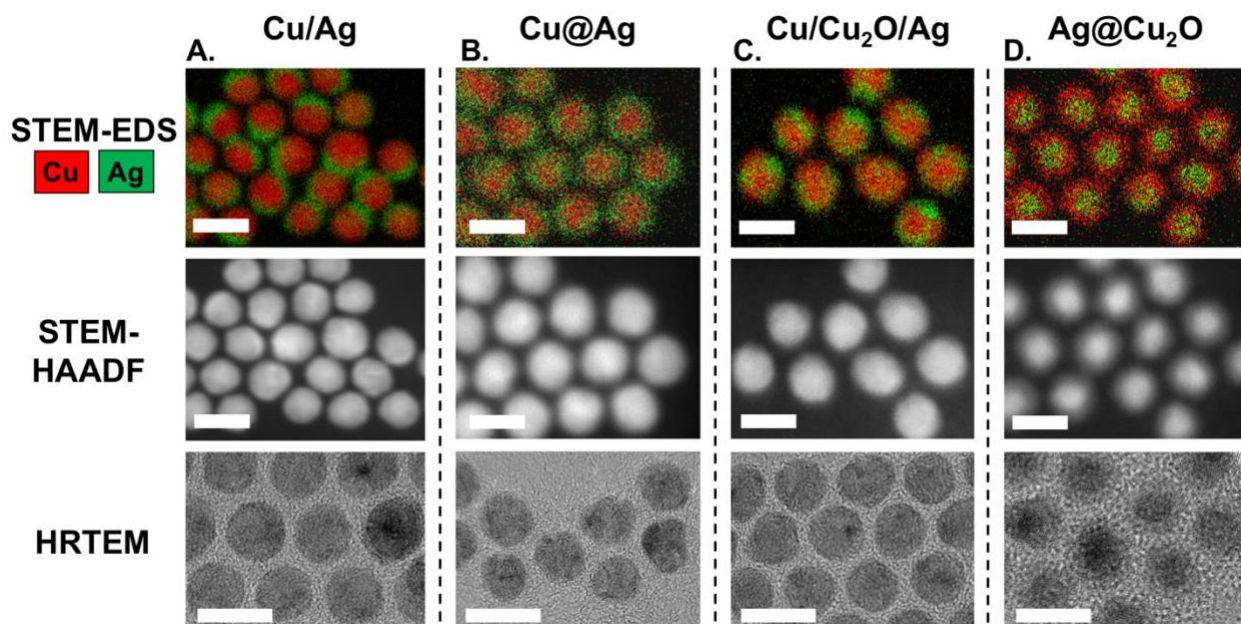
Figure 2.1. Electron microscopy images of Cu-Ag bimetallic nanoparticles
Each row represents an electron imaging technique: STEM-EDS, STEM-HAADF, and HRTEM. All scale bars correspond to 10nm. Each column represents a different synthesized morphology. A: Cu/Ag nanocrescents (imaged in air-free conditions). B: Cu@Ag core-shell nanocrystals (imaged in air-free conditions). C: Cu/Cu$_2$O/Ag – Cu/Ag nanocrescents oxidized at room temperature. D: Ag@Cu$_2$O core-shell NCs synthesized by oxidizing nanocrescents at 90 °C.

Different conditions were probed for galvanic exchange by varying temperature and the relative concentration of Ag/Cu (Figure 2.2 A-D). Qualitatively, higher temperatures speed up the reaction, and higher concentrations of Ag salt result in a higher atomic fraction of Ag (at%Ag) in the bimetallic particles. The spatial distribution of Cu and Ag displays a more complex dependence on these two factors. While smaller amounts of Ag salt always favor the formation of an incomplete crescent-shaped shell (Cu/Ag) over the complete-shell (Cu@Ag), this relationship is also affected by the reaction temperature. At room temperature, slower diffusion rates result in more uniform coverage of particles. In contrast, at elevated temperatures (e.g., 90 °C), a heterogeneous population is more likely, with some particles having more Ag than the others (Figure 2.8). At higher temperatures, Ag exchanges with Cu faster, leading to more heterogeneity. This is possibly due to the faster nucleation and dissolution rates at elevated temperatures, which lead to bigger Ag clusters and broader size distribution of the islands.[74]
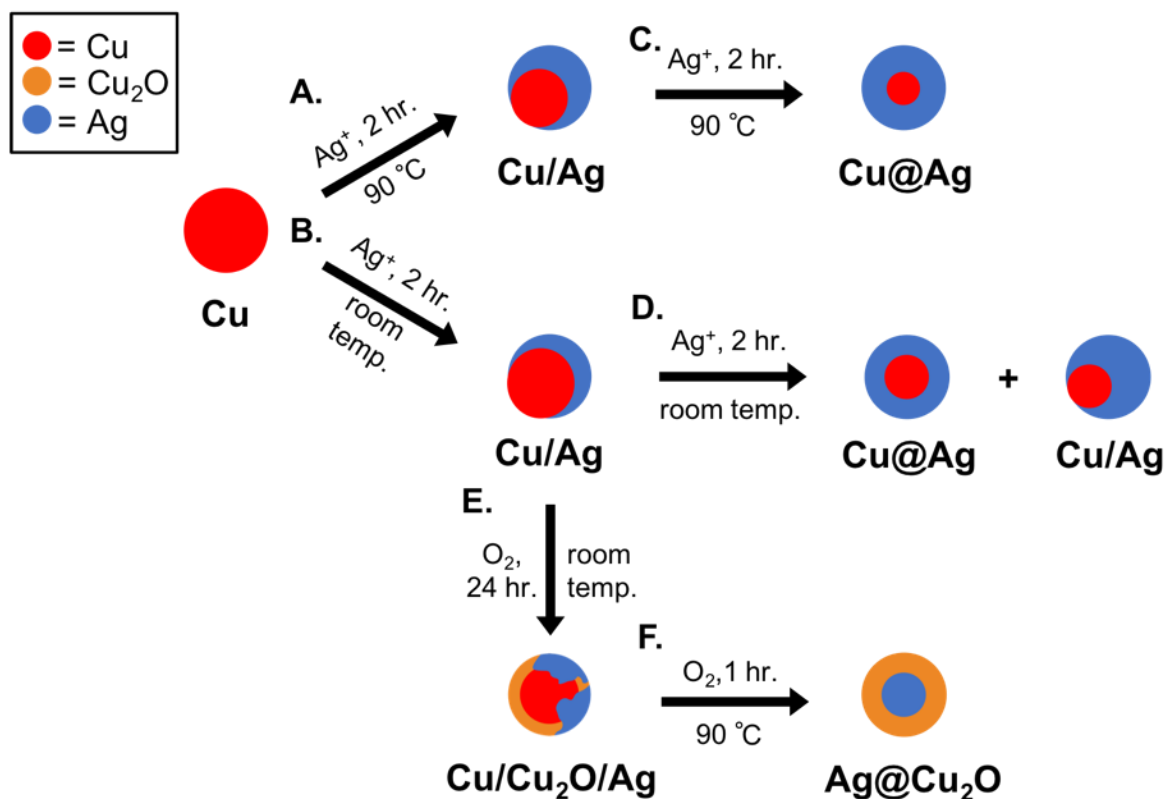
Figure 2.2. Reaction sequence for the synthesis of Cu-Ag bimetallic nanoparticles
A-B: Galvanic exchange of Cu nanoparticle with Ag^+ (at 25 °C and 90 °C) resulting in Cu/Ag crescents. C-D: Further addition of Ag^+ results in a formation of Cu@Ag particles or a mixture of Cu@Ag and Cu/Ag. In both cases, no more Ag can be incorporated. E: Exposure to oxygen at 25 °C oxidizes Cu to Cu_2O on the surface of the nanoparticles. F: Heating in air oxidizes Cu completely and inverts the morphology to $Ag@Cu_2O$.

When more Ag^+ is added to the nanoparticle solution or when the galvanic exchange initially starts with a larger Ag^+ amount, the shell coverage on the particles increases. Temperature dictates whether all particles can achieve complete-shell geometry. At 25 °C, at%Ag saturates at about 35% on average. At this ratio, some particles are fully core-shell, while others are locked in a crescent shape with an incomplete shell (Figure 2.9). As long as the galvanic exchange is kept at room temperature, further addition of Ag^+ does not change the Cu:Ag ratio. At 90 °C, we were able to synthesize Cu@Ag particles with 60 at%Ag on average, but only when the galvanic exchange with Ag^+ was performed twice. For particles fully covered in Ag, further galvanic exchange does not occur (as tested at both 25 °C and 90 °C), preventing further changes in Cu:Ag ratio. It is less apparent why the Cu/Ag crescents cannot incorporate more Ag. Possibly, due to strain arising from Cu-Ag lattice mismatch and energetics, no more Ag atoms can enter the particles, making the crescent structure the lowest energy configuration. The crescent geometry remains stable over long periods of time (at least one year), giving further evidence of its stability. A thin layer of cuprous oxide on the surface would also block galvanic exchange, but the particles have never been exposed to oxygen, so we doubt that this is the case.

2.3 Particle oxidation in air

While it was crucial to synthesize and characterize the Cu-Ag nanoparticles without any exposure to oxygen for the comparison of theoretical and experimental results, we were also interested in the morphological changes induced by oxidation. In air, Cu nanoparticles invariably oxidize to copper oxide, but it is usually Cu(I), not Cu(II).[72,75] This oxidation dramatically changes the electronic and mechanical properties of copper.[59] However, researchers have demonstrated that adding Ag slows down oxidation rates.[69,76] For Cu@Ag, the mechanism of oxidation prevention is a simple one: Cu is covered with layers of Ag atoms, preventing contact with O_2 molecules. For particles with Cu atoms on the surface, the mechanism of oxidation prevention is more complex. DFT calculations suggest that as a result of a partial electron transfer from Cu to Ag, the affinity of Cu to O_2 decreases.[69] Recently, the reduction of oxygen binding energy of Cu has been experimentally observed for Cu-Ag bulk foils.[45]

During the galvanic exchange at 25 °C, as all Cu sites on the surface get oxidized, oxygen access is blocked and Cu(0) gets trapped underneath, resulting in $Cu/Cu_2O/Ag$ geometries (Figure 2.2 E). This phenomenon is analogous to the formation of $Cu@Cu_2O$ from Cu, already observed for the monometallic nanoparticles used in galvanic exchange.[72] A more pronounced transformation occurs for Cu/Ag particles oxidized in air at 90 °C. At this temperature, the atomic mobility increases enough to fully oxidize Cu to Cu_2O and induce an inversion, from Ag being on the surface to Ag being exclusively enclosed in the core of $Ag@Cu_2O$ particles (Figure 2.2 F). This reaction does not occur for Cu@Ag heated in air, nor Cu/Ag heated in the glovebox, indicating that temperature alone cannot change the morphology of Cu/Ag particles. Oxygen is necessary to bring Cu atoms on the surface of Ag, since Cu_2O is characterized by lower surface energy and larger lattice constant as compared to Ag[77,78]. As only Cu/Ag transform into $Ag@Cu_2O$ upon heating, the observed inversion is useful in separating Cu/Ag from Cu@Ag.

To investigate oxidation states of Cu and Ag experimentally, X-ray photoelectron spectroscopy (XPS) and electron diffraction were used. XPS has the capacity of resolving oxidation states on the surface of the material, while electron diffraction, operating on the same principle as X-ray diffraction, identifies bulk crystal structure. Proper identification of surface Cu oxidation state is particularly difficult, as Cu(0) and Cu(I) cannot be reliably resolved using the principal line of the Cu 2p edge. Instead, Auger lines need to be used as they display a sufficient energy separation from each other.[79] Using XPS measurements, we were able to unambiguously confirm that Cu oxidizes primarily to Cu(I) (Figure 2.3); however, some Cu(II) is present on the surface (Figure 2.10a). Furthermore, the oxidation of dried Cu/Ag particles occurs on the timescale of hours at room temperature: particles left in air for only 2 hours still have mostly Cu(0) on the surface, and even after three days there is still some metallic Cu left. As expected, $Ag@Cu_2O$ formed after oxidation at elevated temperatures shows only Cu(I) and Cu(II), while Cu@Ag primarily contains metallic Cu. Although technically XPS can probe the sample up to 10nm deep,[80] which is more than the diameter of studied bimetallic particles, signal is strongest from the top-most layer, which explains why the Ag signal is stronger for Cu@Ag and weaker for $Ag@Cu_2O$, while the opposite is true for the Cu edges.
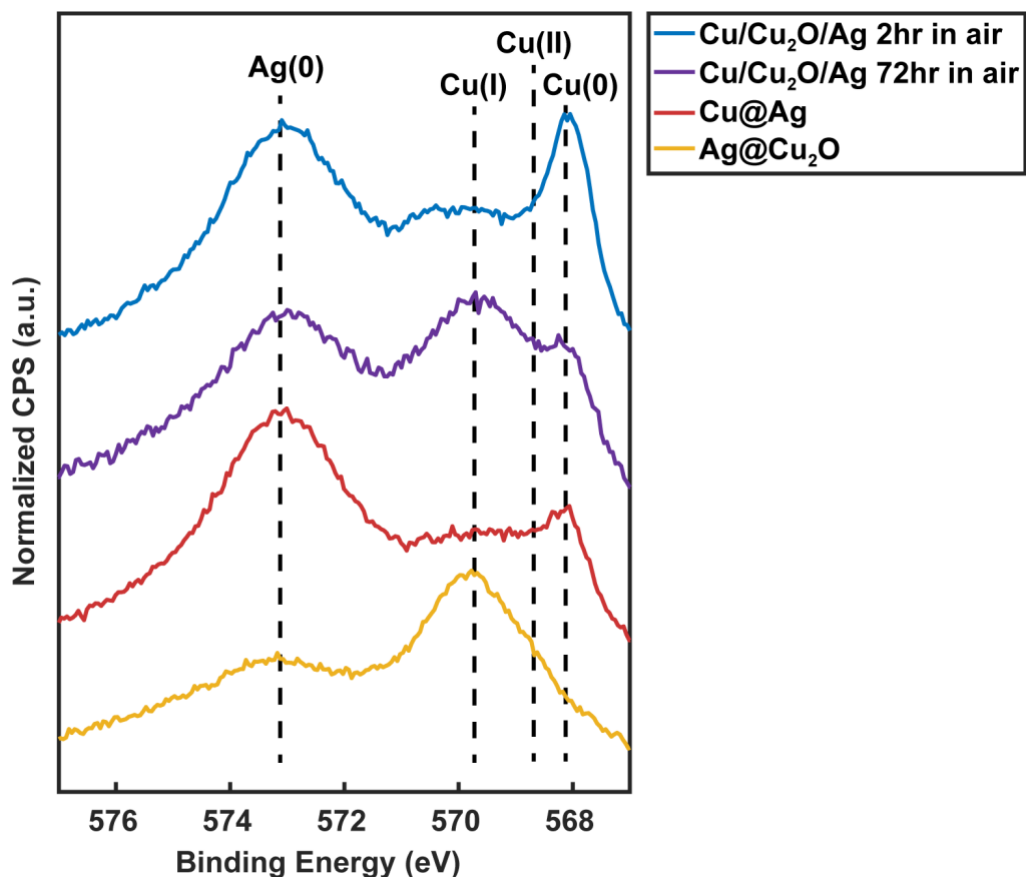
Figure 2.3. X-ray photoelectron spectroscopy spectra of Ag 3p and Cu LMM regions
Cu/Cu2O/Ag (2 hr and 72 hr in air, respectively), Cu@Ag and Ag@Cu2O

Further information concerning Cu and its oxidation state came from the Cu 2p edge. At the Cu 2p edge, the resolution of Cu(0) vs. Cu(I) is uncertain, but Cu(II) displays a sufficient shift to be recognized (Figure 2.10a). Unsurprisingly, Cu(II) is most abundant for Ag@Cu2O, but this phase seems to be present to some extent in all samples. The Cu 2p edge also provided additional evidence for Cu(0) oxidation to Cu(I) based on the exact position of the main peak. According to literature, Cu(I) exists at slightly lower binding energy than Cu(0),[79] and indeed, Ag@Cu2O is shifted by 0.3eV in relation to Cu@Ag (Figure 2.10a).

Regarding the oxidation state of Ag, there have been reports of Ag particles oxidizing in air, at least on the surface.[81] In this work, however, no substantial oxidation changes for Ag were observed, even during the transformation into Ag@Cu2O. The Ag 3d edge of Cu@Ag had signal strong enough to show the loss features that are only present for Ag(0) (Figure 2.10b).[82] While other spectra did not have the signal strength required to observe the loss features, all Ag 3p edges displayed the same asymmetric shape which again indicated the presence of Ag metal.[82] The observed lack of Ag oxidation for Cu-Ag bimetallic particles may be caused by a large difference in the formation energies of Ag2O and Cu2O, which significantly favors the formation of the latter.[65] Furthermore, any molecular oxygen coming in contact with Ag atoms is likely to move towards Cu domains, due to the binding energy differences.[83]

Finally, it is worth mentioning that the transformation into Ag@Cu$_2$O seems irreversible. Reversing the oxidation of Cu to Cu$_2$O was attempted by exposing Ag@Cu$_2$O to three reducing agents: Tris(trimethylsilyl)silane (TTMSS), carbon monoxide and lithium triethylborohydride (LiEt$_3$BH, Super-Hydride®). While TTMSS and CO were used at temperatures above 100 °C, according with previous literature reports,[84,85] LiEt$_3$BH is potent enough to reduce Cu salts at room temperature. Nevertheless, none of these agents succeeded in obtaining Ag@Cu particles. Instead, we observed Cu etching and dewetting of the metals, resulting in pure Ag particles (former cores) remaining. Such results demonstrate the importance of surface energies and lattice strains in dictating particle morphologies. Metallic Cu has a significantly smaller lattice than metallic Ag does, while the surface energy of the latter is much larger than that of the former. Therefore, Cu(0) cannot accommodate a Ag(0) core underneath it, and the existence of Ag@Cu morphology for particles smaller than 10 nm is very unlikely.[55,86]

2.4 Optical properties of Cu-Ag nanocrystals

While both Cu and Ag feature plasmonic responses, the two metals possess significantly different onset energy for interband transitions resulting in an interesting optical behavior when the two metals are in close contact.[70] The Cu-Ag optical properties are attractive for theoretical considerations as well as potential applications, such as light-driven catalysis.[70,87] The optical extinction spectra obtained for our Cu-Ag bimetallic nanoparticles are in good agreement with previous reports.[65,70] As Ag is introduced into the particles, a strong resonance feature appears and redshifts towards the standard Ag absorption (for <10 nm particles) of around 410 nm. At the same time, the Cu feature (~570 nm) fades away and eventually completely disappears (Figure 2.4a). Absorption peaks for Cu-Ag are broadened and dampened as compared to monometallic particles.
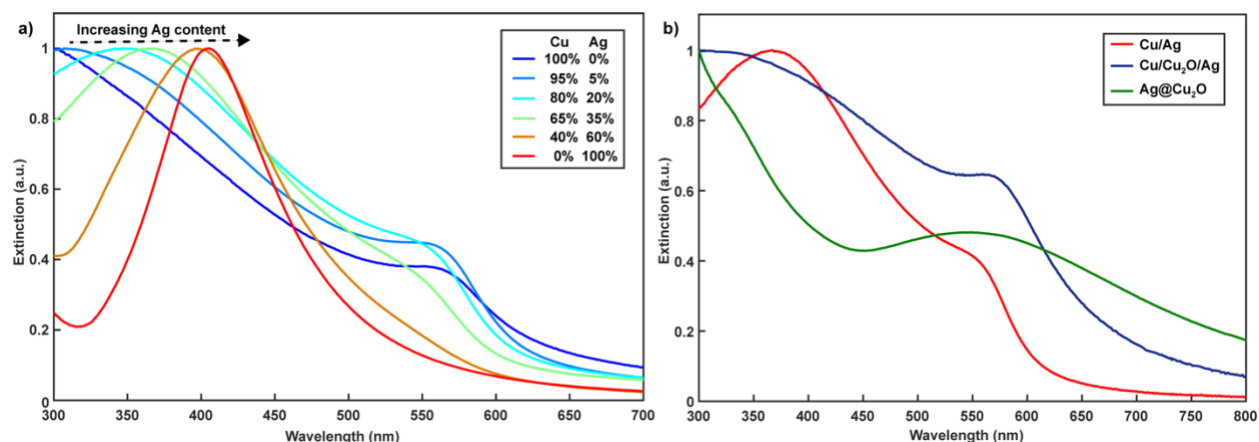
Figure 2.4. Optical extinction spectra
a) Unoxidized Cu-Ag bimetallic particles together with monometallic Cu particles (used for the galvanic exchange) and Ag particles of the same size (~7 nm)[88] for comparison. b) Cu-Ag crescents (20 at%Ag) before and after oxidation in air. Spectra are normalized to the maximum peak.

As metallic Cu turns into semiconducting Cu$_2$O, the optical extinction undergoes significant changes (Figure 2.4b). These changes can only be observed for Cu/Ag crescents, where Cu is on the surface and prone to oxidation, as Cu@Ag does not oxidize. It is well-reported that the metal cluster oxidation is responsible for a redshift, which moves the Cu plasmon peak from

approximately 570 nm to 590 nm.[72,89] The damping of both resonances can be explained and modeled by the formation of an outer oxide shell of large refractive index with the correlated size reduction of the remaining metallic core.[65] Indeed, the dampening is stronger for Ag@Cu$_2$O than for the Cu/Cu$_2$O/Ag sample. The presence of the oxide is also characterized by an increasing absorption in the infrared. This increasing infrared absorption (>700 nm), caused by the direct forbidden bandgap of Cu$_2$O,[90] is perhaps the most easily identifiable sign of the degree of particle oxidation.

The plasmon shift tied to the Cu:Ag ratio provides useful information during the synthesis process. Measuring the optical extinction is a much faster and accessible way to observe the galvanic exchange in Cu-Ag formation than imaging with an electron microscope. Although the latter provides more direct structural information and STEM-EDS is a technique that allows unambiguous material characterization, UV-Vis (especially combined with ICP-OES) can serve as a quick identification tool for more routine syntheses. In the future, the plasmon shift could be useful for a catalytic application that requires the absorption center to be at 350-370 nm instead of 400 nm and above, as it is the case with pure Ag. As the resonance feature disappears as a result of Cu$_2$O formation, reducing and air-free environments, e.g., CO$_2$ reduction, may be best suited for light-driven Cu-Ag catalysis.

2.5 Thermodynamic consideration of crescent vs. core-shell formation

Since Cu and Ag can hypothetically arrange in a variety of different morphologies, this system is a good model case for determining the equilibrium geometry based on the thermodynamics of surface and interface energies. However, thermodynamic equilibrium models are not applicable for kinetically-trapped products that change over time.[91] To the best of our knowledge, the existence of well-controlled Cu-Ag crescents has not been reported yet, so we wanted to confirm that the synthesized particles are equilibrium products and their shape can be elucidated with a model based on thermodynamics.

In the past, researchers observed dewetting of Ag from Cu@Ag particles over the course of one year.[68] Nevertheless, Cu/Ag crescents synthesized with our method do not seem to be undergoing any such changes. A 1-year-old sample, heated overnight at 100 °C in a glovebox (dissolved in isoamyl ether), shows no morphological change under STEM-EDS (Figure 2.12). While it is only suggestive, and not a complete proof that Cu/Ag crescents are indeed in a quasi-equilibrium instead of being kinetically-trapped, it certainly shows that inducing Ag dewetting is significantly harder than in the previous cases. The discrepancy may come from synthesizing the particles in the presence of different solvent and ligands or because of incidental partial oxidation. As it will be demonstrated, crescents can be equilibrium structures of the nanoparticle synthesis.

Inspired by a simple thermodynamic model,[62] we aimed at calculating the specific shape of a Cu-Ag crescent and the energy difference between various geometries. While the model described in reference 14 is general, we apply this model to our specific Cu-Ag system. Differences in interface/surface energies for different facets are ignored, and it is assumed that there is no stress at the interface. As the surface energy of Cu is significantly larger than that of Ag (for example $\gamma_{Cu(111)} = 1.83$ J/m^2 and $\gamma_{Ag(111)} = 1.25$ J/m^2),[78] it is reasonable to exclude Ag@Cu as a possible equilibrium product. Therefore, θ, the angle of the Ag coverage on Cu, is a good descriptor of the

different idealized Cu-Ag shapes: separated monometallic Cu and Ag, crescent (Cu/Ag) and core-shell (Cu@Ag) (Figure 2.5). During galvanic exchange, Ag atoms can either homonucleate forming separate Ag particles ($\theta = 0°$) or grow on top of the Cu core ($\theta > 0°$). There's an energetic drive to cover Cu with Ag, which lowers the surface energy of the entire particle, but it also introduces increasing amount of the unfavorable Cu-Ag interface caused by a large lattice mismatch between the two elements without a sufficient electronegativity difference.[56] These interactions create an interesting interplay allowing for the possible existence of either Cu/Ag ($\theta < 180°$) or Cu@Ag ($\theta = 180°$).

Figure 2.5. The model depicting three possible Cu-Ag geometries
Separated, crescent and core-shell, described with a single order parameter (θ).
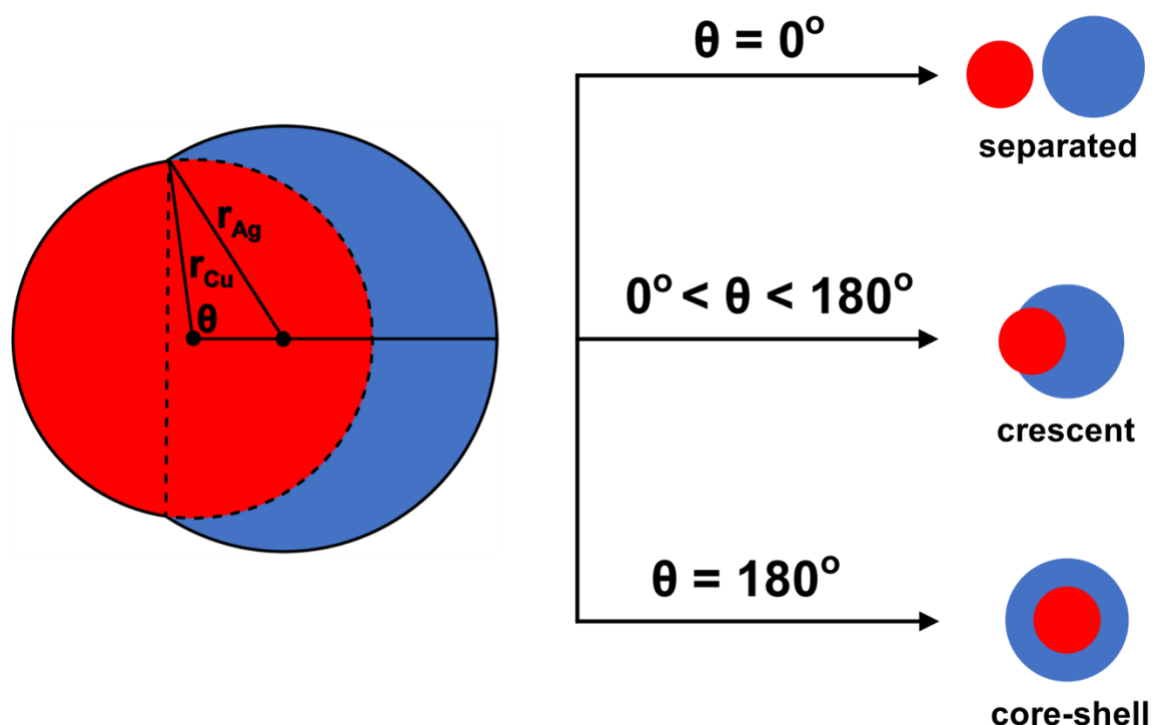
For small particles, especially smaller than 10nm in diameter, surface and interface energies, i.e., quantities scaling with area, not volume, begin to dominate the energetic landscape.[92] The presented model considers only structures and energies of spheres and spherical caps. The Cu core is always represented by a sphere, while the geometry of the incomplete shell of Ag is represented by spherical caps that depend on the interplay between different surface energy terms (see Section 2.7.5 for more details). For any given Cu:Ag ratio, the radius of the Cu core (r_{Cu}), and the angle θ, there is only one possible configuration in the model.

As long as there is a constant amount of Cu and Ag in the system, the cohesive energy, which scales with volume, cancels out. Under this condition, the simplest yet informative model needs to incorporate only three values: γ_{Cu} and γ_{Ag}, the surface energies of Cu and Ag, and γ_{Int}, the Cu-Ag interface energy. All these energies depend on a given facet,[78] but as long as perfect spheres are considered, there is no faceting involved, and average surface energy values suffice. The

experimentally obtained particles do not display apparent faceting either (Figure 2.1), so this assumption seems appropriate. It should be noted that the surface and interface energies display size dependence for small nanoparticles, especially <5 nm in diameter.[93,94] When considering that size regime, it is prudent to apply a correction for the bulk energy values. However, the surface free energy of 7-8 nm size nanocrystals (Figure 2.1) differs from the bulk value by less than 5%.[93]

Surface and interface energies are positive, hence equilibrated structures will tend towards diminishing their overall contribution. Therefore, the most stable arrangement can be found by calculating total energies, i.e., summing up each γ multiplied by a corresponding surface area and finding the geometry with the minimum energy value (see Section 2.7.5 for more details). As we intend for the model to elucidate the relationship between the surface and interface energies, instead of focusing on any specific values, the variables can be further simplified to γ_{Cu} / γ_{Int} and γ_{Ag} / γ_{Int}. The calculated energy was then normalized by setting γ_{Int} to 1. This way, the model can be numerically solved for a range of values of γ_{Cu} and γ_{Ag} (Figure 2.13).

It has already been demonstrated that the crescent structure ($0° < \theta < 180°$) is energetically favorable for intermediate values of γ_{Cu}, γ_{Ag}, and γ_{Int}, namely $\gamma_{Cu} < \gamma_{Ag} + \gamma_{Int}$ and $\gamma_{Int} < \gamma_{Cu} + \gamma_{Ag}$.[62] However, the exact shape of the crescent, as well as the degree by which crescent geometry is more favorable than that of core-shell, depend on the specific Cu:Ag ratio (Figure 2.6). When the at%Ag is small, the optimal θ is also small and the crescent is the equilibrium shape. On the other hand, for particles mainly composed of Ag, the thermodynamic preference between a crescent and a core-shell structure is greatly diminished. This theoretical relationship corresponds with the experimental results. Experimentally, at approximately 20 at%Ag, all synthesized particles are clearly in the crescent shape, but at 35 at%Ag, both crescents and core-shell can be observed (Figure 2.2).
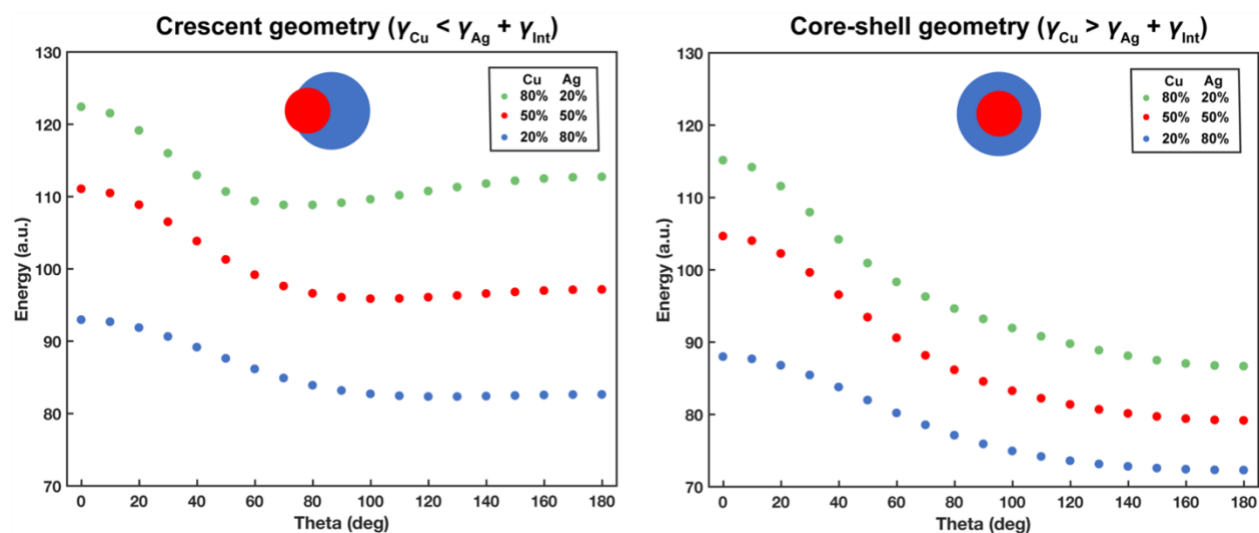
Figure 2.6. Calculated energies for two sets of γ_{Cu}, γ_{Ag}, and γ_{Int}
The calculations are done for three different atomic ratios of Cu:Ag that lead to either crescent geometry, with the minimum energy value corresponding to an intermediate value of θ (left) or core-shell geometry, where θ =180° has the lowest energy (right).

Regarding valid parameter ranges in the model, the consideration of γ_{Cu} being either smaller or greater than the sum of γ_{Ag} and γ_{Int} is not a hypothetical one. While γ_{Cu} is always larger than γ_{Ag}, molecular dynamics (MD) calculations show that based on the facets, the interplay of surface and interface energies can result either in crescent or core-shell being the equilibrium structure, i.e., either $\gamma_{Cu} < \gamma_{Ag} + \gamma_{Int}$ or $\gamma_{Cu} > \gamma_{Ag} + \gamma_{Int}$, respectively.[95] For example, Cu(111) interfacing with Ag(111) should form a core-shell structure (since $\gamma_{Cu} > \gamma_{Ag} + \gamma_{Int}$ according to the MD calculations),[95] but if the interface is positioned on (100) facets (i.e., $\gamma_{Cu} < \gamma_{Ag} + \gamma_{Int}$), then one would expect a formation of crescents. It is generally assumed that the Cu-Ag interface occurs along lowest-energy facets, i.e., (111),[55] but often these energies are calculated based on bulk surfaces. They do not include curvature and surface effects, which are very important for small nanoparticles. It should also be remembered that theoretical calculations often do not consider ligands, which can change the surface energies.[96] The γ_{Cu} and γ_{Ag} relevant for the thermodynamic model correspond to surfaces capped with TDPA, not for bulk surfaces in vacuum. Nevertheless, the model suggests that the average interface between the two metals in Cu/Ag crescents more closely resembles that of (100) facets than (111).

The same type of thermodynamic analysis can be performed for Ag@Cu$_2$O, which also consists of only two materials. Although we could not find a calculated value for the interface energy between Ag and Cu$_2$O for any facets in the literature, the fact that only core-shell structures were observed at elevated temperatures leads to the conclusion that $\gamma_{Ag} > \gamma_{Cu2O} + \gamma_{Int}$. In other words, the surface energy of Cu$_2$O must be significantly lower than that of Ag (calculated $\gamma_{Cu2O(111)}$ = 0.71 J/m^2 vs. $\gamma_{Ag(111)}$ = 1.25 J/m^2)[77] or the interface energy between these two materials, γ_{Int}, is relatively low. Since Cu$_2$O and Ag have less of a lattice mismatch than Cu and Ag do, and there have been reports of epitaxially-grown Cu$_2$O on Ag,[97] γ_{Int} between the two materials should indeed be small, corroborating the simple thermodynamic model.

The two trends, smaller θ and stronger preference for crescent over core-shell for lower at%Ag, are true for all values from the intermediate regime of $\gamma_{Cu} < \gamma_{Ag} + \gamma_{Int}$ and $\gamma_{Int} < \gamma_{Cu} + \gamma_{Ag}$ (Figure 2.13). We consider the Cu:Ag ratio to be particularly relevant since it can be directly controlled in experimental settings. Surface energies can be modified by changing the size of particles (especially for <5 nm in diameter)[93] or the binding ligand,[96] but the exact dependence of γ_{Cu}, γ_{Ag}, and γ_{Int} on these alterations is complex and experimentally challenging. On the contrary, adjusting the Cu:Ag ratio is relatively easy, simply by bringing more Ag$^+$ into the reaction solution (although only as long as there is Cu remaining on the nanocrystal surface for galvanic exchange).

With this ability to control the Cu:Ag ratio, one can consider how it affects the likely geometry of the particles and create a simple phase diagram. For the most dynamic region of surface and interface energies, i.e., where the crescent shape is theoretically an equilibrium structure, the energy difference between various geometries can be investigated as a function of the atomic fraction of Ag. Under these assumptions, we distinguish three synthetic regimes based on the atomic fraction of Ag: crescents only, both crescents and core-shell, and core-shell only (Figure 2.7). Such division matches the experimentally obtained results (Figure 2.2). It is important to remember that our model does not include the cohesive energies of Cu and Ag, as we only intend to compare the energetic stability of different structures for a specific composition of the metals. Therefore, Figure 2.7 is meant to illustrate the relative stability of possible geometric

arrangements with the same at%Ag and emphasize the dependence of thermodynamic preference for crescent over core-shell on the atomic fraction of Ag. Since we control the concentration of Ag$^+$ added in our experiments, this model seems appropriate to elucidate the structural features observed.
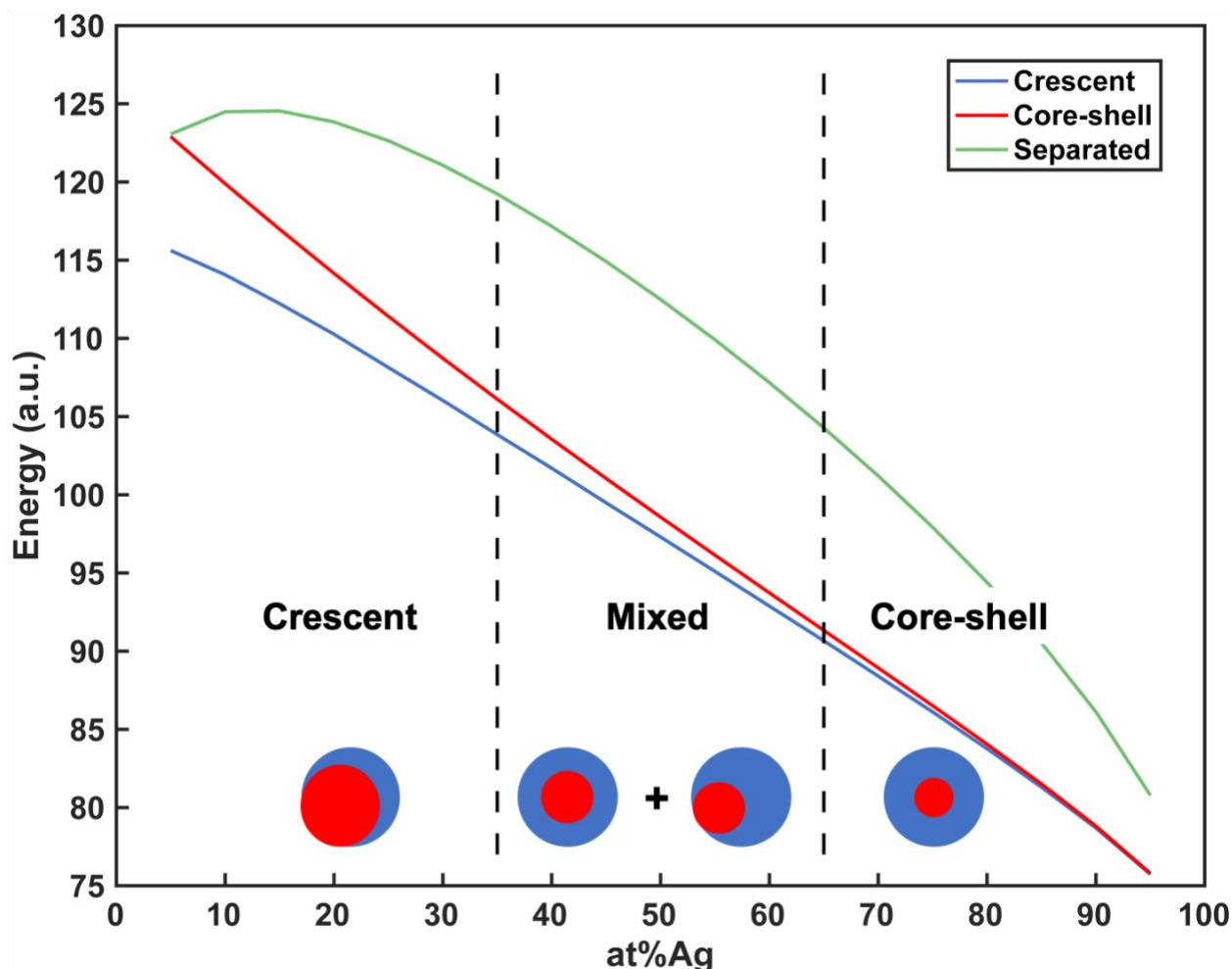
Figure 2.7. Calculated energies of three possible Cu-Ag shapes
Calculations are done for different atomic fractions of Ag under the condition where the crescent is the equilibrium structure (i.e., $\gamma_{Cu} < \gamma_{Ag} + \gamma_{Int}$ and $\gamma_{Int} < \gamma_{Cu} + \gamma_{Ag}$). The three presented regimes correspond to experimentally observed structures, since the energy difference between crescent and core-shell varies with at%Ag.

The correspondence between the simple thermodynamic model and the experimental results is not perfect, as the model predicts that for a given set of γ_{Cu}, γ_{Ag}, and γ_{Int} there can be only one equilibrium geometry and it does not take into account entropic considerations. However, the consideration of the energetic difference between crescents and core-shell enables the creation of a framework for understanding how surface and interfacial energies affect the geometry of a bimetallic particle composed of two non-alloying metals at a given elemental ratio. Considering the ease of the thermodynamic model and its limited assumptions (perfectly spherical shapes, does

not include any faceting and cohesive information), we find the insights offered to be highly instructive.

2.6 Conclusion

While precise predictions of geometries for nanoparticle syntheses are still challenging, the overall trends in binary Cu-Ag nanocrystal formation and the resulting phases were elucidated with a simple thermodynamic model that takes into account the counteracting forces of surface and interface energies. A part of this calculated phase diagram of Cu-Ag nanoalloys was experimentally explored to demonstrate that the same synthetic scheme can lead to both bifacial and core-shell geometries. Low atomic fractions of Ag favor the formation of nanocrescents, which have not been observed for this system before. High atomic fractions of Ag lead to more complete surface coverage, such that eventually only core-shell structures are formed. This dependence leads us to believe that surface and interface energies of the system are in an intermediate range, i.e., $\gamma_{Cu} < \gamma_{Ag} + \gamma_{Int}$, according to the model predictions.

Using high-resolution elemental mapping, taking care to avoid oxygen and air exposure, the effect of oxidation on morphology was isolated and showed that temperature has a key influence on the degree to which Cu is oxidized to Cu_2O. At room temperature, some Cu(0) gets trapped in the core to form $Cu/Cu_2O/Ag$ structures but 90 °C is sufficient to increase material mobility and results in an oxidative inversion to $Ag@Cu_2O$. The atomic fraction of Ag and the degree of oxidation significantly affect the optical behavior, resulting in changes in both absorption position and strength. The strong plasmonic response of Ag is dampened by contact with Cu, especially in its oxide form due to the semiconducting nature. The four synthesized and characterized structures (Cu/Ag, Cu@Ag, $Cu/Cu_2O/Ag$, $Ag@Cu_2O$) may find applications in fields such as catalysis, optics, and electronics, especially when a high degree of control over the surface elemental composition is needed.

2.7 Supplementary information

2.7.1 Supplementary figures and tables

Table 2.1. Atomic fractions of Cu and Ag based on STEM-EDS and ICP-OES

Sample	STEM-EDS		ICP-OES	
	at%Cu	at%Ag	at%Cu	at%Ag
Cu/Ag	78.1	21.9	81.2	18.8
Cu@Ag	37.3	62.7	38.5	61.5
$Cu/Cu_2O/Ag$	81.8	18.2	81.3	18.7
$Ag@Cu_2O$	81.5	18.5	79.9	20.1
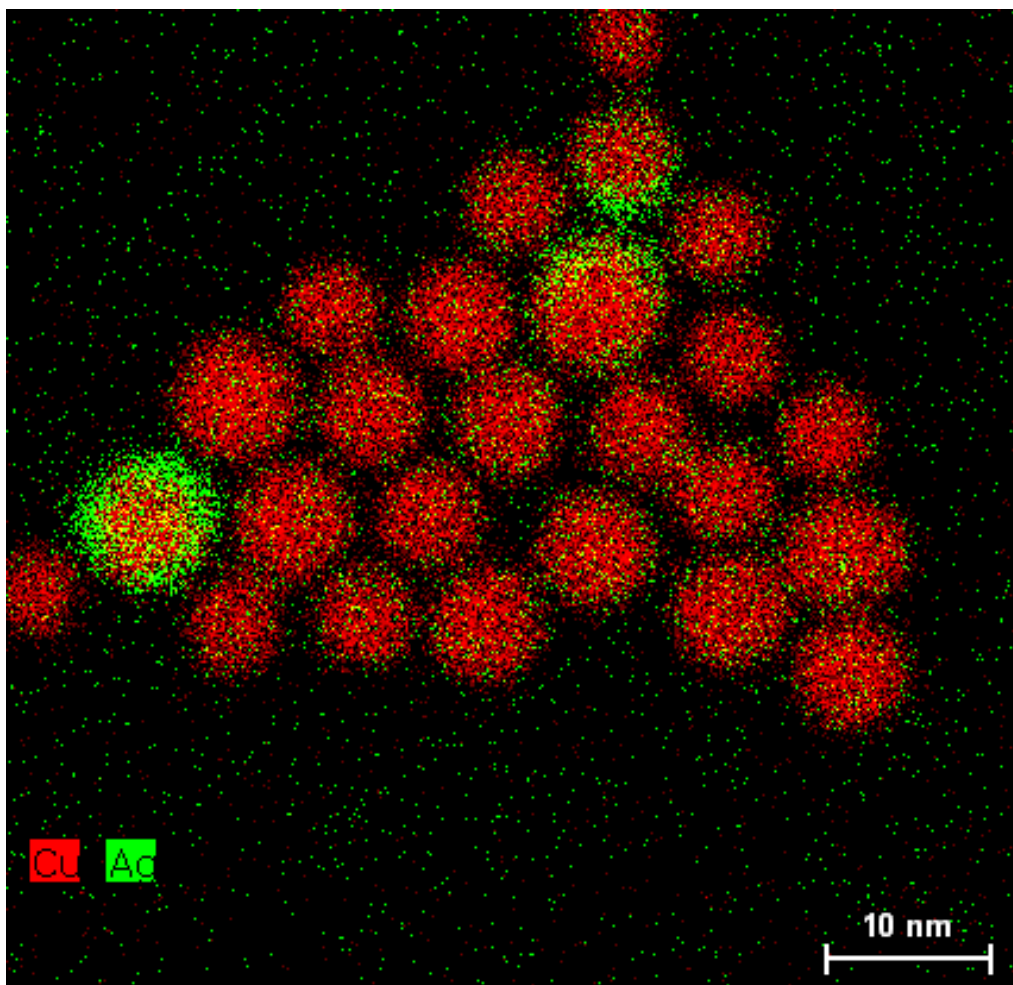
Figure 2.8. STEM-EDS of Cu/Ag crescents synthesized at 90 °C
The figure depicts particles that display a particularly heterogeneous Cu:Ag atomic fractions.
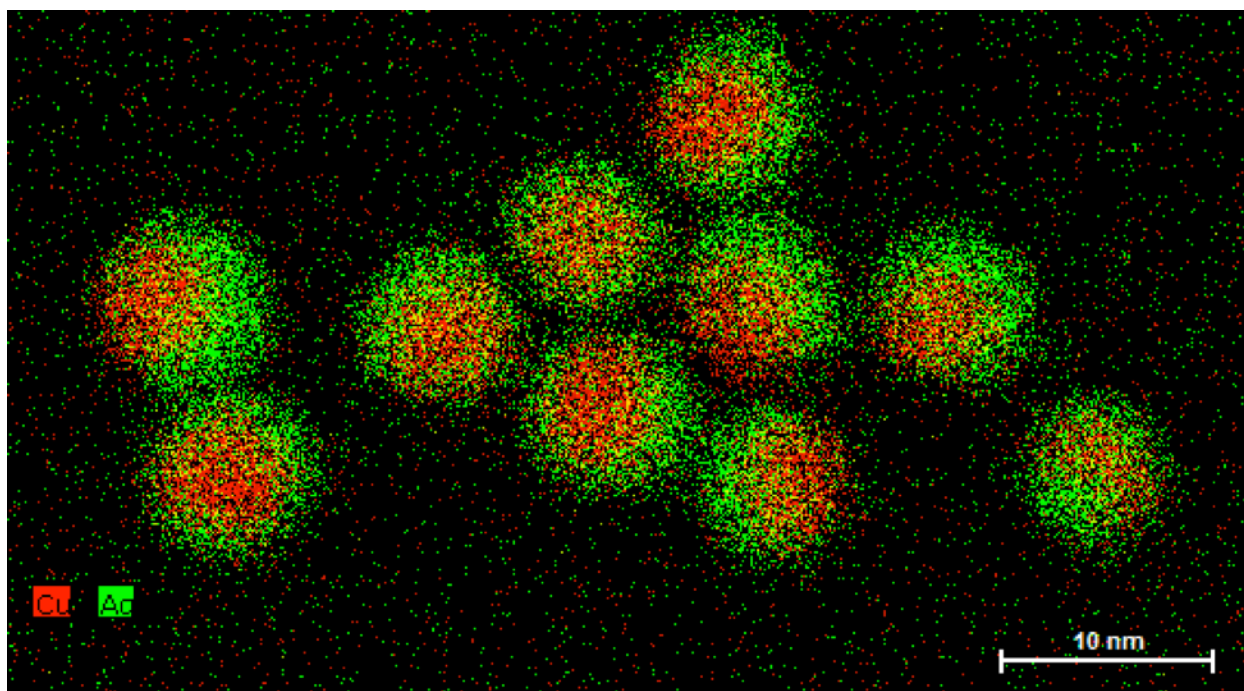
Figure 2.9. STEM-EDS of Cu/Ag crescents and Cu@Ag synthesized at room temperature. *Despite adding an excess of Ag⁺, some particles remain in the crescent shape.*
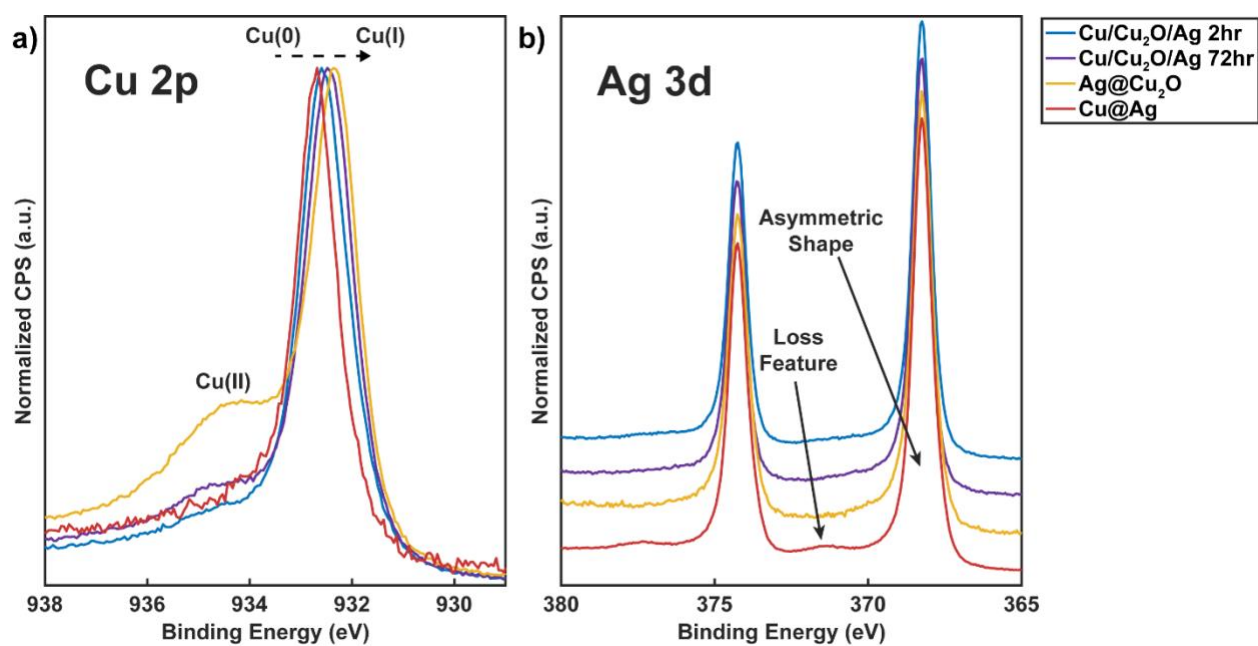
Figure 2.10. Further X-ray photoelectron spectroscopy spectra *(a) Cu 2p and (b) Ag 3d regions for Cu/Cu₂O/Ag (2hr and 72hr in air, respectively), Cu@Ag and Ag@Cu₂O.*
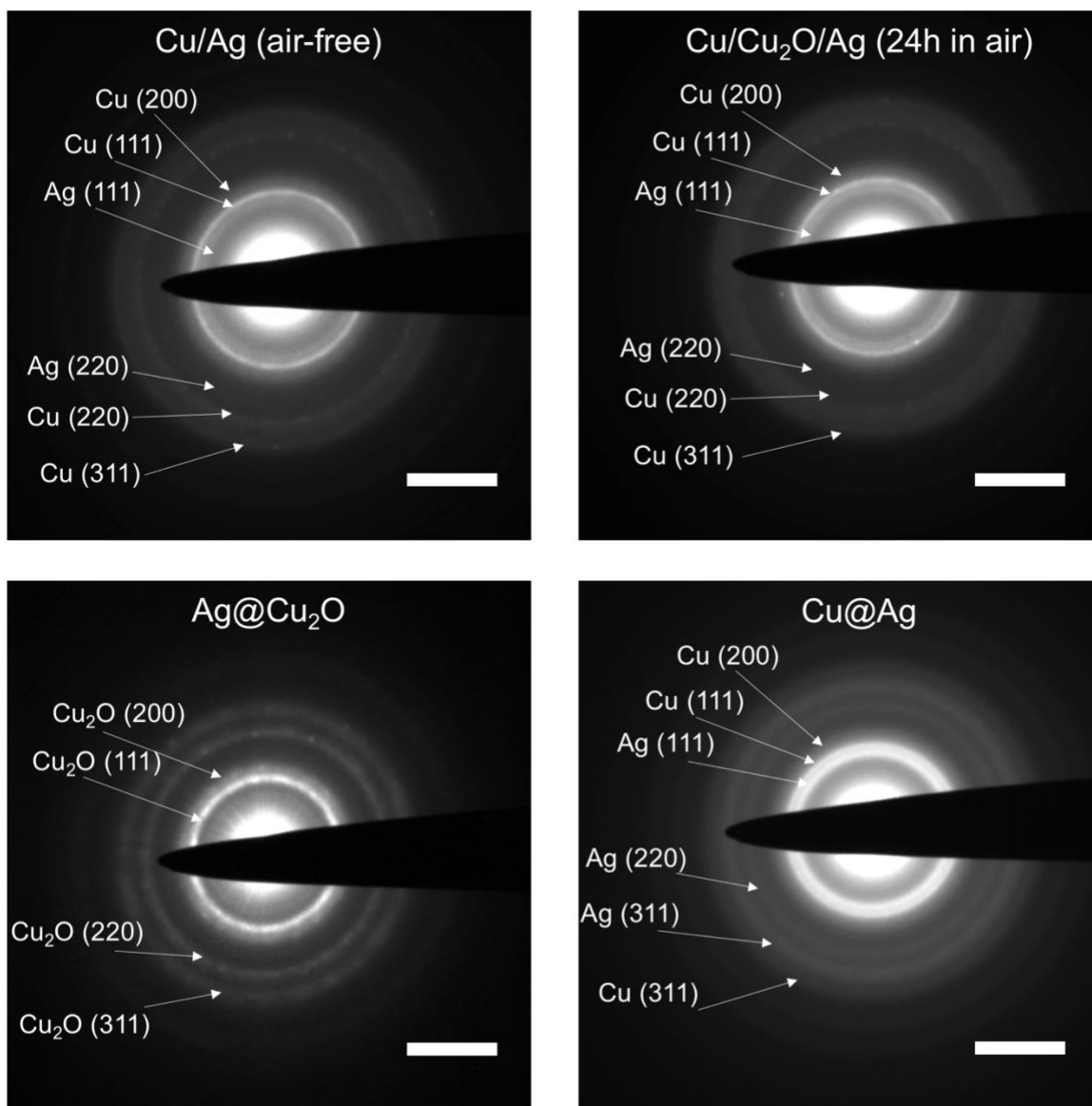
Figure 2.11. Electron diffraction patterns
The diffraction rings are created from many randomly oriented nanoparticles of Cu/Ag crescent (air-free and 24h in air), Ag@Cu$_2$O and Cu@Ag. All scale bars correspond to 5 nm^{-1}.

The layer of Cu$_2$O in Cu/Cu$_2$O/Ag kept in air for 24hr is thin enough to be seen on XPS but not on a bulk measurement of electron diffraction. Thus, the pattern for Cu/Cu2O/Ag is the same as for the Cu/Ag sample that has been exposed to air for less than one minute. Bulk differences are only observed for Ag@Cu$_2$O. Again, there is some Cu(II) present on the surface, but the bulk material is unambiguously Cu$_2$O. Although Cu/Ag and Cu@Ag consist of the same materials, Cu(0) and Ag(0), the intensity of diffraction rings corresponds to relative amounts of Cu and Ag. Since Cu@Ag has three times more Ag than Cu/Ag, signal coming from Ag is much more visible in the obtained diffraction pattern. The diffraction powder patterns also confirm lack

of bulk Ag oxidation, as no diffraction rings smaller than Ag(111) are observed. As Ag oxides have larger lattice constants than Ag metal, the presence of smaller diffraction rings would indicate Ag oxidation.
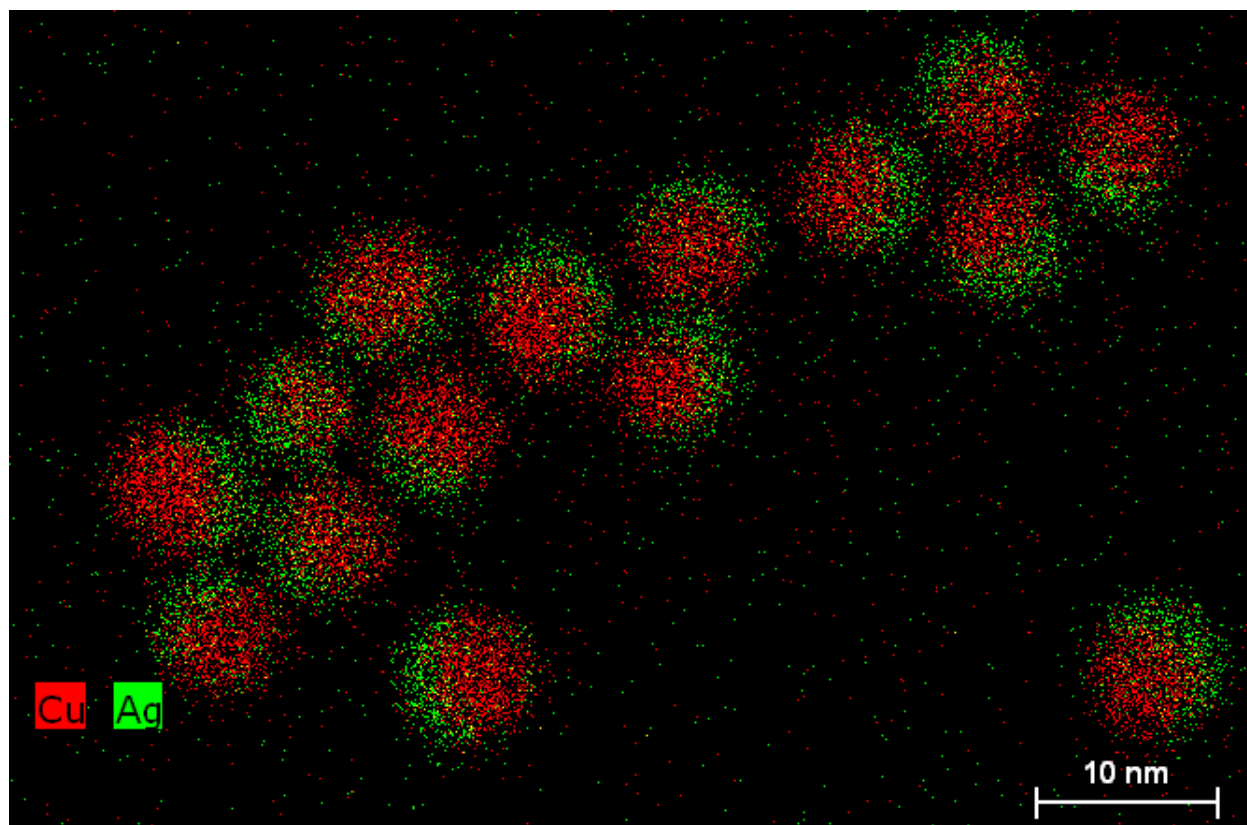
Figure 2.12. STEM-EDS of 1-year-old Cu/Ag crescents after overnight heating
At 100 °C in isoamyl ether under argon
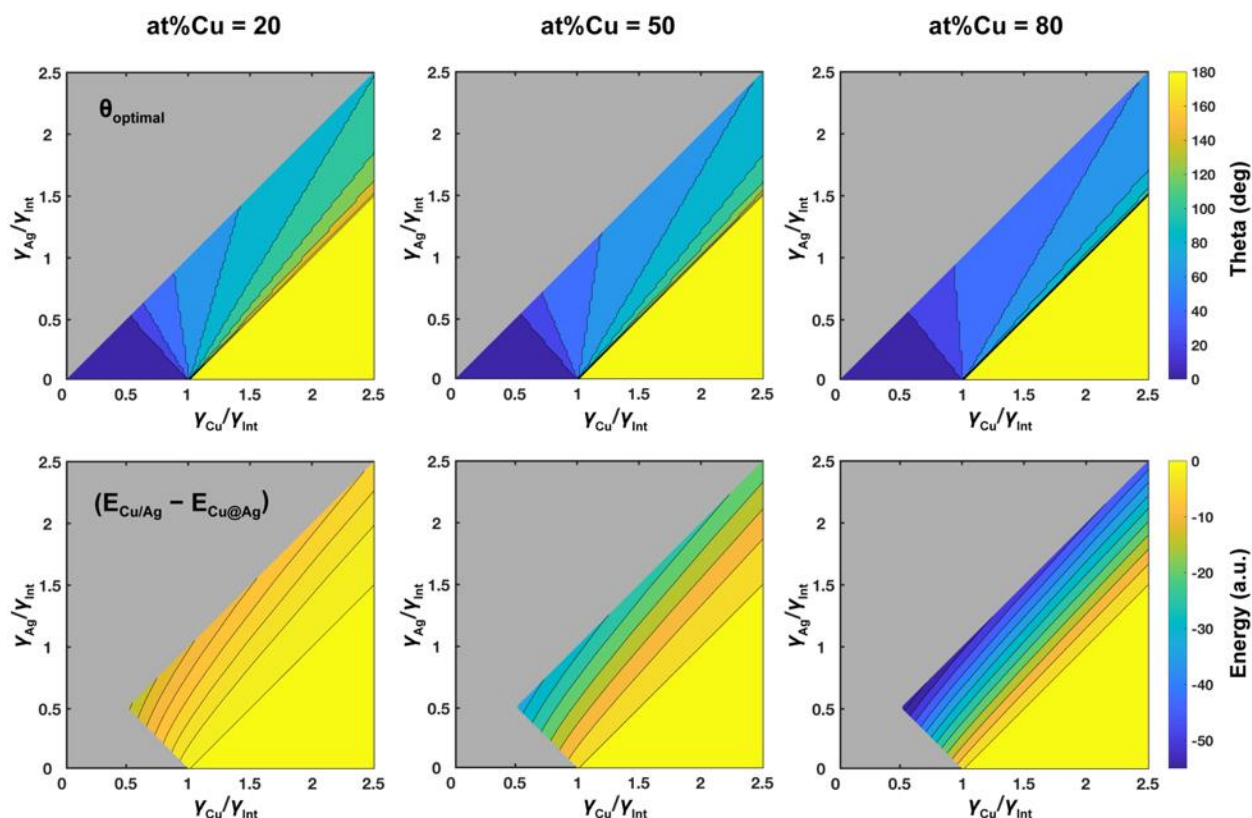
Figure 2.13. Energy and shape considerations for a range of γ_{Cu} and γ_{Ag} values
Top row: optimal value of θ as a function of ratios of γ_{Cu}/γ_{Int} and γ_{Ag}/γ_{Int} for three different atomic fractions of Cu. Bottom row: energy difference between Cu/Ag optimal crescent structure (5° ≤ θ ≤ 175°) and Cu@Ag geometry as a function of ratios of γ_{Cu}/γ_{Int} and γ_{Ag}/γ_{Int} for three atomic fractions of Cu.

2.7.2 Used materials

Copper(I) acetate (Sigma-Aldrich, 97%), n-tetradecylphosphonic acid (abbrev. as TDPA, Sigma-Aldrich, 97%), Trioctylamine (Sigma-Aldrich, 98%), Isoamyl ether (Sigma-Aldrich, 99%), Silver Trifluoroacetate (abbrev. as Ag TFA, Sigma-Aldrich, ≥99.99% trace metals basis), Nitric acid (Sigma Aldrich, ≥99.999% trace metals basis), Water (Milli-Q, 18.2 MΩ), Hexane (Sigma-Aldrich, mixture of isomers, anhydrous, ≥99%), Ethanol (Sigma-Aldrich, pure, anhydrous, ≥99.5%), Isopropanol (Sigma-Aldrich, anhydrous, 99.5%), Tris(trimethylsilyl)silane (Sigma-Aldrich, 97%), Super-Hydride® solution (Sigma-Aldrich, 1.0 M lithium triethylborohydride in THF). All materials were used without further purification unless specified otherwise in the experimental methods.

2.7.3 Synthesis

Cu nanoparticle synthesis
Cu nanoparticles capped with TDPA (~7 nm diameter) were synthesized according to a literature procedure, with strict air-free handling procedures to avoid any risk of particle oxidation that could

impact subsequent synthetic steps.[72] Briefly, trioctylamine was degassed in a Schlenk flask by heating at 90 °C under vacuum for an hour and then transferred and stored in a glovebox. In the same glovebox, 123 mg of copper(I) acetate, 139 mg of n-tetradecylphosphonic acid, and 10 mL of degassed trioctylamine were added to a 25 mL three-neck flask equipped with a transfer valve. The solution was stirred in an argon environment on a Schlenk line and heated to 105 °C to ensure that all solids were dissolved. Then it was rapidly heated (approx. 2 °C/s rate) to 180 °C and kept at this temperature for 30 min. The reaction mixture was subsequently heated to 270 °C (approx. 2 °C/s rate) and kept at this temperature for another 30 min. The purplish red colloidal solution was cooled down to room temperature and the whole flask was transferred immediately into a glovebox for particle purification. Cu particles were precipitated by addition of 1:1 ethanol:isopropanol mixture (1.25 × the volume of particles solution) and centrifuged at 5,000 rpm for 5 minutes without air exposure. Particles were re-dispersed in hexane and the centrifugation step was repeated. For TEM imaging and general storage, particles were again re-dispersed in hexane, and for the galvanic exchange, they were re-dispersed in isoamyl ether. Throughout all this process, care was taken to avoid any exposure to air.
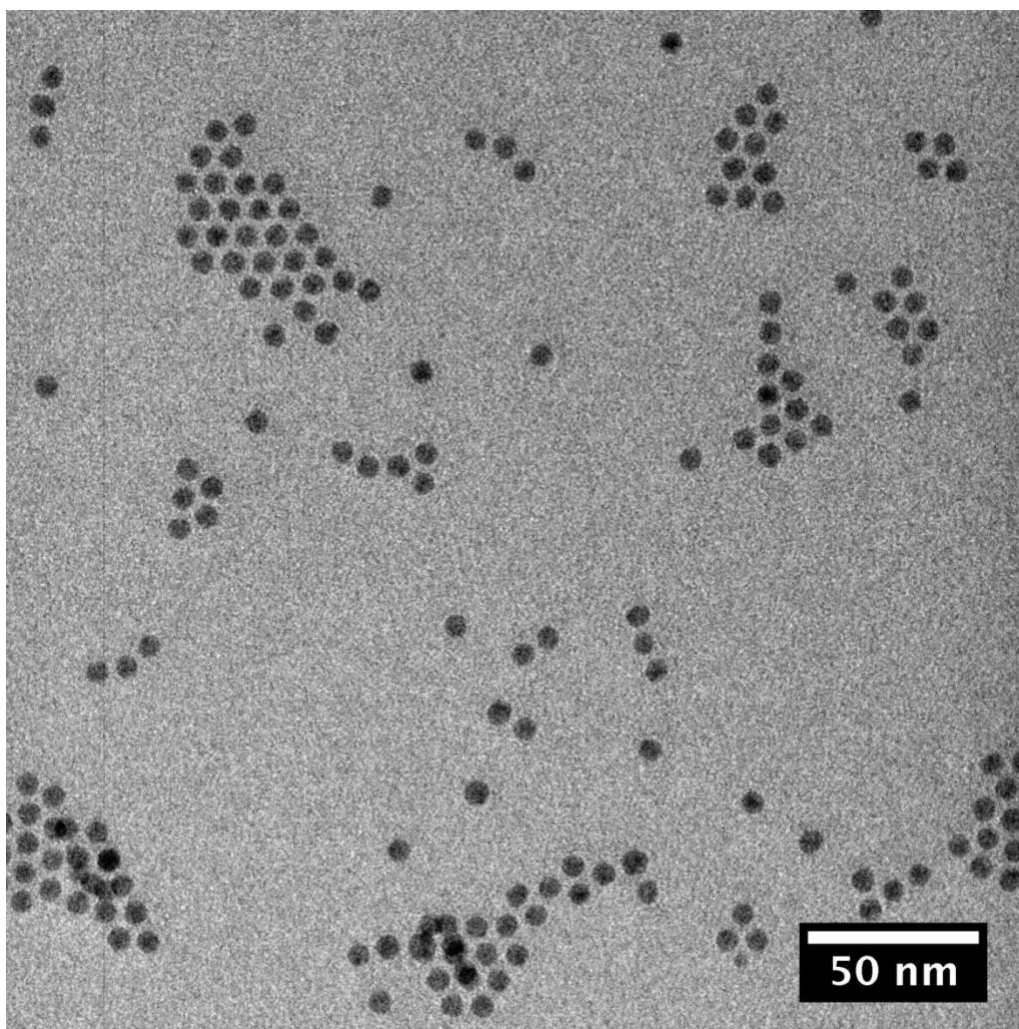
Figure 2.14. TDPA-capped Cu nanoparticles used for galvanic exchange imaged with bright-field TEM

Cu/Ag bimetallic formation via galvanic exchange

Using the centrifugation/re-dispersion method described in the previous section, Cu particles were dissolved in isoamyl ether (previously dried and degassed by heating at 130 °C for an hour under argon) in the glovebox. Based on inductively coupled plasma optical emission spectrometry (ICP-OES), Cu concentration was about 3 mg/mL. Separately, silver trifluoroacetate solution in isoamyl ether was prepared (5 mg added per 1g of ether). To initiate galvanic exchange, the solution of Cu particles (500 mg) was mixed with the Ag ether solution (100-700 mg). The maximum amount of Ag TFA was dictated by the trifluoroacetate anion that precipitated the particles in a concentration higher than approximately 12mM. The reaction time was 2 hr, and heating, if needed, was provided by a hot plate inside the glovebox. For example, Cu/Ag crescents (20 at%Ag) were synthesized by adding 250 mg Ag solution for 2 hr at 25 °C; a mixture of Cu/Ag and Cu@Ag (35 at%Ag) was obtained by adding 600 mg Ag solution for 2 hr at 25 °C; Cu@Ag core-shell NCs (60 at%Ag) were synthesized by adding two batches of 700 mg Ag solution, each time for 2 hr at 90 °C. At the end of the reaction time, particles were precipitated and re-dispersed in hexane, following the same procedure as in the previous section, or in isoamyl ether to add another batch of Ag TFA.

Particle oxidation and inversion to Ag@Cu₂O

Particles were oxidized at room temperature either by taking the hexane solution out of the glovebox and exposing it to air or by letting hexanes dry completely and having particles in direct contact with air. To accomplish a full conversion to Ag@Cu₂O, the solvent was evaporated outside of the glovebox and dry particles were heated for an hour at 90 °C. Afterward, particles were re-dispersed in hexane again.

2.7.4 Characterization methods

Electron Microscopy

Routine transmission electron microscopy (TEM) was done by drop-casting particles on a TEM grid (Electron Microscopy Sciences, CF-400-Cu) and acquiring images on a 200 kV Tecnai G2 T20 S-TWIN with a Gatan SC200 CCD camera. High-resolution (HRTEM) was acquired either on JEOL 2100-F or FEI TitanX, both operating at 200 kV. Selected area electron diffraction (SAED) patterns, as well as STEM-HAADF and STEM-EDS imaging were performed on FEI TitanX using a Fischione high-angle annular dark-field (HAADF) detector with an inner semi-angle, β, of 63 mrad. The EDS detector was the FEI Super-X windowless detector with a solid angle of 0.7 steradians. Bruker Esprit software was used for quantitative elemental analysis. To minimize carbon contamination, ultrathin carbon on gold TEM grids (Ted Pella, 01824G) were cleaned with oxygen-plasma right before drop-casting the particles. For oxygen-free imaging, the TEM grid was prepared and inserted into a TEM holder in a glovebox. The holder was then transported to the microscope inside a protective vacuum sheath in order to maintain the argon atmosphere until just before inserting into the microscope (<1 min exposure to air).

X-ray photoelectron spectroscopy

The core level, Auger, and valence band spectra of the CuAg bimetallic nanoparticles were measured using a Kratos Axis Ultra DLD x-ray photoelectron spectrometer (XPS). All spectra

were acquired using monochromatized Al Kα radiation (15 kV, 15 mA). Ar sputtering of the sample surface was avoided in order to prevent surface composition changes resulting from the nonequivalent sputtering rates of Cu and Ag. The ligands used to stabilize the nanoparticles prevented facile charge transfer to the glassy carbon substrate, which resulted in charge accumulation within the nanoparticles during the course of analysis. Charge neutralization was conducted by flooding the chamber with electrons at a current of 1.6 A, which was experimentally determined to be optimal for suppressing measurement artifacts arising from the accumulation of charge within the nanoparticles. Since it was not possible to use the C 1s edge for calibration, the kinetic energy scale of the measured photoemission spectra was instead calibrated by setting the Ag $3d_{5/2}$ binding energy to 368.25 eV. The actual oxidation state of Ag was determined by the presence of loss features and an asymmetric shape of the peaks, which is indicative of the metallic Ag(0) state.[82]

Other techniques

UV-VIS spectroscopy of nanoparticle colloidal suspension in hexane in air-free quartz cuvettes was performed using Shimadzu UV-3600 UV-VIS-NIR spectrophotometer. Absolute concentration of Cu and Ag in the solution was determined by inductively coupled plasma optical emission spectrometry (ICP-OES) using Perkin Elmer ICP Optima 7000DV. ICP sample preparation was done after at least two rounds of centrifugation to ensure the absence of any salt precursors. The nanoparticles were digested in high-purity nitric acid and diluted with ultrapure water to reach the optimal concentration for the measurement (0.5-10 ppm).

2.7.5 Mathematical details of the thermodynamic model

The thermodynamic model of surface and interface energies in Cu-Ag nanoparticles is based on previous research of wetting in multiphase systems, especially the work of Yuan *et al.*[62] The math described below was done according to the Yuan model. All interface energies are assumed to be isotropic and all interfaces are assumed to be stress-free. We compute and compare the energies of the competing structures in order to determine the most stable morphology, i.e., the equilibrium geometry. This basic model takes into account only three parameters: γ_{Cu} and γ_{Ag}, the surface energies of Cu and Ag, and γ_{Int}, the Cu-Ag interface energy. Three morphologies are considered: core-shell, crescent and separated monometallic clusters (Figure 2.1). Volume of Cu and Ag as well as the radius of the Cu core remain constant in all the different morphologies.

To ensure similarity with the experimental results, we set r_{Cu} = 7nm. Volume of Ag, V_{Ag}, is calculated by assuming a certain Cu:Ag ratio:

$$V_{Ag} = \left(\frac{4.09\text{Å}}{3.61\text{Å}}\right)^3 \times \frac{at\%Ag}{at\%Cu} \times V_{Cu} \tag{2.1}$$

where 4.09Å and 3.61Å are lattice constants of Ag and Cu, respectively, at%Ag and at%Cu are atomic fractions of Ag and Cu in the system, and V_{Cu} is the volume of Cu.

The energy of each morphology, in terms of input variables r_{Cu}, V_{Ag} and θ, is calculated in the following way:

  1. Core-shell

31

$$E = \gamma_{Ag} \times A_{Ag} + \gamma_{Int} \times A_{Cu} = \gamma_{Ag} \times 4\pi \left(\frac{3}{4\pi}(V_{Ag} + V_{Cu})\right)^{2/3} + \gamma_{Int} \times 4\pi r_{Cu}^2 \qquad (2.2)$$

where A_{Ag} is the surface area of the Ag shell, and A_{Cu} is the surface area of the Cu core.

2. Separated monometallic particles

$$E = \gamma_{Ag} \times A_{Ag} + \gamma_{Cu} \times A_{Cu} = \gamma_{Ag} \times 4\pi \left(\frac{3}{4\pi}V_{Ag}\right)^{2/3} + \gamma_{Cu} \times 4\pi r_{Cu}^2 \qquad (2.3)$$

where A_{Ag} and A_{Cu} are the surface areas of Ag and Cu spheres respectively.

3. Crescent

$$E = \gamma_{Ag} \times A_{Ag} + \gamma_{Int} \times A_{Cu,covered} + \gamma_{Cu} \times A_{Cu,exposed} =$$

$$= \gamma_{Ag} \times 2\pi r_{Ag}^2 \left(1 + \sqrt{1 - \left(\frac{r_{Cu}}{r_{Ag}}\sin\theta\right)^2}\right) + \gamma_{Int} \times 2\pi r_{Cu}^2(1 - \cos\theta) \qquad (2.4)$$

$$+ \gamma_{Cu} \times 2\pi r_{Cu}^2(1 + \cos\theta)$$

where A_{Ag} is the surface area of the Ag incomplete shell; $A_{Cu,covered}$ and $A_{Cu,exposed}$ are the surface areas of two parts of the Cu sphere, covered and uncovered by the Ag shell, respectively. The Cu-Ag nanocrescent is modeled by a sphere and two spherical caps (Figure 2.15).
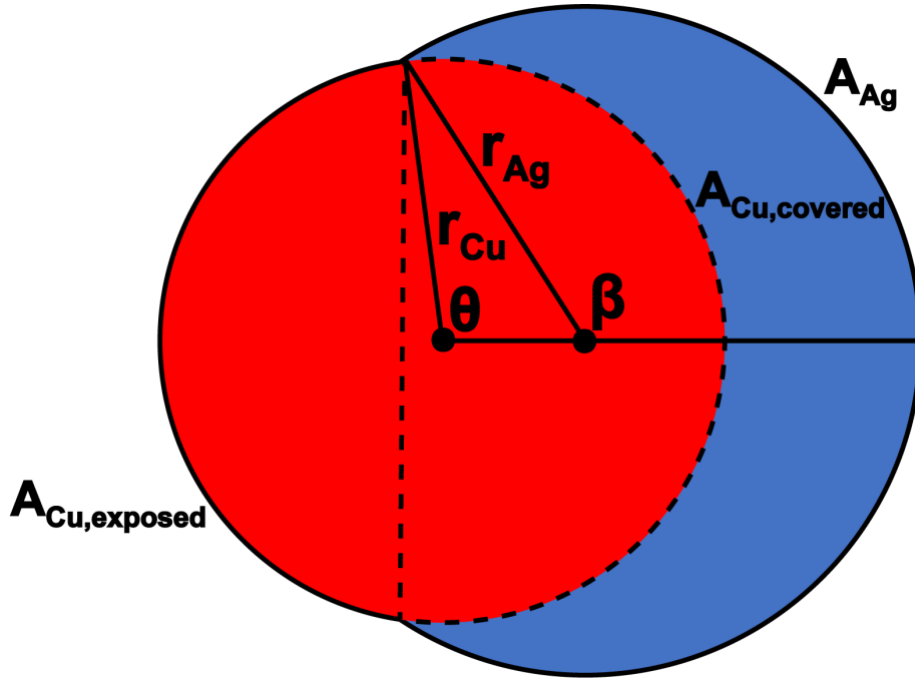
Figure 2.15. Geometric model of the Cu-Ag nanocrescent
It is uniquely described by r_{Cu}, V_{Ag}, and θ. β and r_{Ag} are calculated from these three variables. Cu sphere (red) is divided into two parts: covered and uncovered (exposed) by the Ag shell. There are two spherical caps: smaller, representing only the covered Cu, determined by r_{Cu} and θ, and bigger, representing the entirety of Ag shell and the covered Cu, determined by r_{Ag} and β.

The relationship between variables in Figure 2.15 comes from the Sine Law:

$$\frac{r_{Cu}}{\sin(\pi - \beta)} = \frac{r_{Cu}}{\sin \beta} = \frac{r_{Ag}}{\sin \theta} \qquad (2.5)$$

The surface area and volume of a spherical cap are defined as:

$$A_{cap}(r, \varphi) = 2\pi r^2 (1 - \cos \varphi) \frac{r_{Cu}}{\sin(\pi - \beta)} = \frac{r_{Cu}}{\sin \beta} = \frac{r_{Ag}}{\sin \theta} \qquad (2.6)$$

and

$$V_{cap}(r, \varphi) = \frac{2\pi}{3} r^3 (1 - \cos \varphi) - \frac{\pi}{3} r^3 \cos \varphi \sin^2 \varphi \qquad (2.7)$$

Therefore,

$$A_{Cu,covered} = 2\pi r_{Cu}^2 (1 - \cos \theta) \qquad (2.8)$$
$$A_{Ag} = 2\pi r_{Ag}^2 (1 - \cos \beta) \qquad (2.9)$$
$$V_{Cu,covered} = r_{Cu}^3 \left[\frac{2\pi}{3} (1 - \cos \theta) - \frac{\pi}{3} \cos \theta \sin^2 \theta \right] \qquad (2.10)$$
$$V_{LargeCap} = r_{Ag}^3 \left[\frac{2\pi}{3} (1 - \cos \beta) - \frac{\pi}{3} \cos \beta \sin^2 \beta \right] \qquad (2.11)$$

Note that the large spherical cap contains both the volume of Ag and the volume of Cu covered by it, hence:

$$V_{LargeCap} = V_{Ag} + V_{Cu,covered} \qquad (2.12)$$

β and r_{Ag} used in the equations above must be defined in terms of input variables of the model: r_{Cu}, V_{Ag}, and θ. Therefore,

$$\sin \beta = \frac{r_{Cu}}{r_{Ag}} \sin \theta \qquad (2.13)$$

$$\cos \beta = \pm \sqrt{1 - \sin^2 \beta} = \pm \sqrt{1 - \left(\frac{r_{Cu}}{r_{Ag}} \sin \theta \right)^2} \qquad (2.14)$$

In all geometries that we tested, solutions for β were found to be above 90°, so

$$\cos \beta = - \sqrt{1 - \left(\frac{r_{Cu}}{r_{Ag}} \sin \theta \right)^2} \qquad (2.15)$$

The value of r_{Ag} can be found numerically from the equation:

$$V_{LargeCap} = r_{Ag}^3 \left[\frac{2\pi}{3} \left(1 + \sqrt{1 - \left(\frac{r_{Cu}}{r_{Ag}} \sin \theta \right)^2} \right) + \frac{\pi}{3} \sqrt{1 - \left(\frac{r_{Cu}}{r_{Ag}} \sin \theta \right)^2} \left(\frac{r_{Cu}}{r_{Ag}} \sin \theta \right)^2 \right] \qquad (2.16)$$

When r_{Ag} is known, the surface area of the large spherical cap (Ag shell) can be determined:

$$A_{Ag} = 2\pi r_{Ag}^2 \left(1 + \sqrt{1 - \left(\frac{r_{Cu}}{r_{Ag}} \sin \theta \right)^2} \right) \qquad (2.17)$$

33

The last term needed to calculate the free energy of a crescent from eq. 2.4 is $A_{Cu,exposed}$, i.e. the surface area of the part of the Cu core that is not covered by Ag:

$$A_{Cu,exposed} = A_{Cu,core} - A_{Cu,covered} = 2\pi r_{Cu}^2(1 + \cos\theta) \qquad (2.18)$$

Chapter 3. Morphological change and catalytic performance of Cu-Ag bimetallic nanocrystals

3.1 Morphological change and separation of Cu-Ag nanomaterials during the catalysis

Since the amount of Cu-Ag interface has been postulated to be a significant factor in the catalytic performance, we set to probe it by depositing the controlled amount of Cu and Ag in two different configurations: 1) physical mixtures of monometallic Cu and Ag nanoparticles and 2) bimetallic Cu-Ag nanoparticles (described in Chapter 2) of various Cu:Ag content (Figure 3.1).
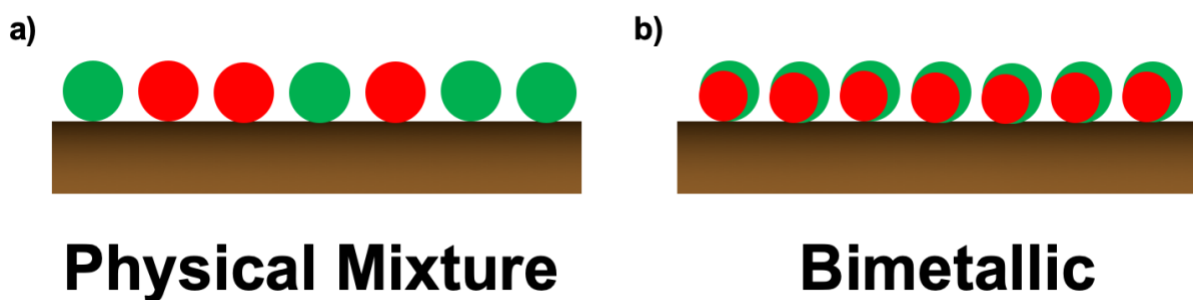
Figure 3.1. Schematic illustration of two types of Cu-Ag catalysts
a) Physical mixture of monometallic Cu and Ag nanoparticles drop-casted onto the glassy carbon substrate b) Bimetallic Cu-Ag nanocrescents drop-casted on the glassy carbon substrate. Red denotes Cu and green denotes Ag.

The drop-casting solutions deposited on glassy carbon electrodes were standardized by adjusting their concentrations using the ICP-OES measurements such that in all of the catalytic runs, the total number of atoms of Cu and Ag remained roughly equal. All nanocrystals were in the size between 5 and 8nm (Figure 3.2). Cu and Cu-Ag particles were bound by the same ligand, tetradecylphosphonate (TDPA), but for synthetic reasons, Ag nanoparticles were bound by oleylamine.
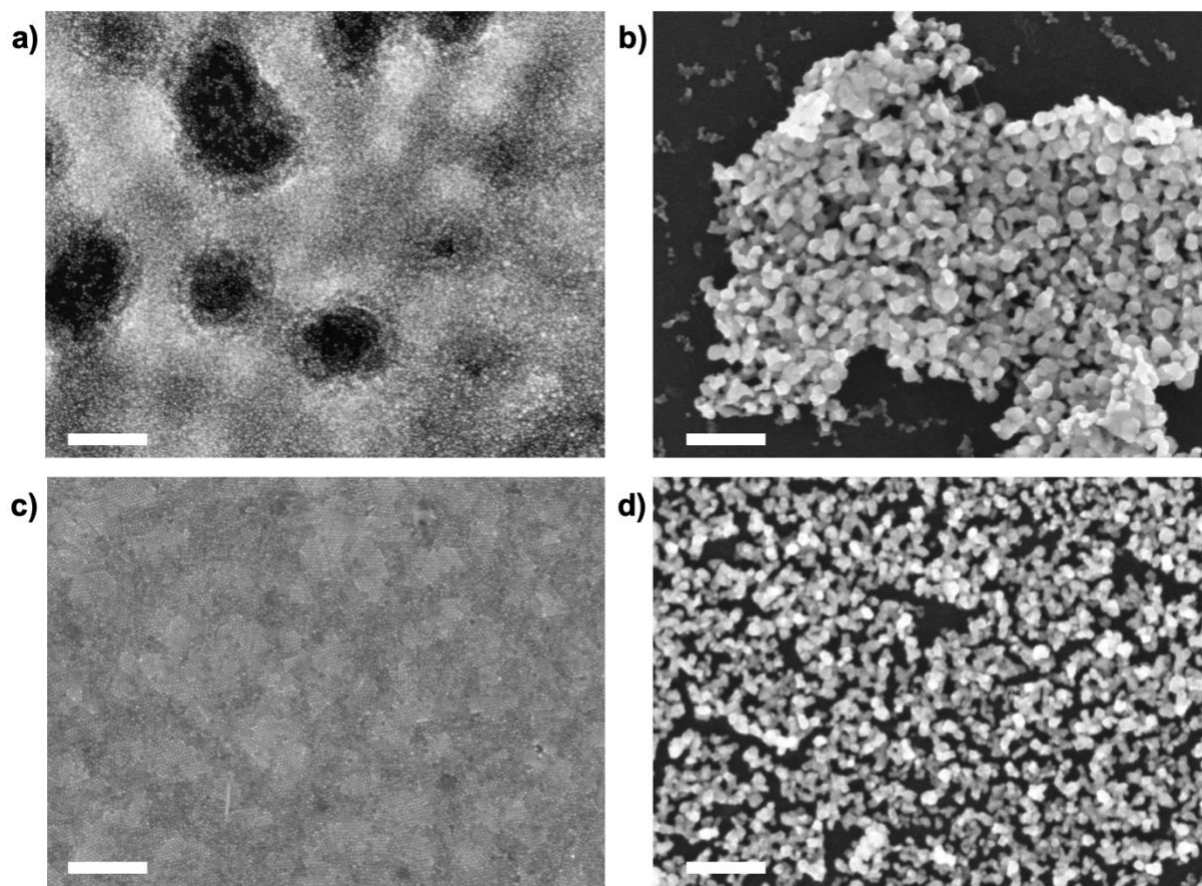
Figure 3.2. SEM images of Cu-Ag nanomaterials used for catalysis
Physical mixture of monometallic Cu and Ag nanoparticles (50 Cu%at) (a) before and (b) after the catalysis at -1.1V vs. RHE for 60 min. Cu/Ag bimetallic (75 Cu%at) (c) before and (d) after the catalysis at -1.1V vs. RHE for 60 min. All scale bars correspond to 200 nm.

The original intention of probing the relevance of Cu-Ag interfaces by using physical mixtures versus bimetallic samples turned out to be hindered by significant morphological restructuring (Figure 3.2). As the particles sintered and joined to form a continuous film, we lost the ability to differentiate between the two distinct original catalyst architectures. To understand the resulting morphology better and see whether there are still differences between the physical mixtures versus bimetallic, we transferred the materials onto TEM grids and imaged them with STEM-EDS (Figure 3.3).
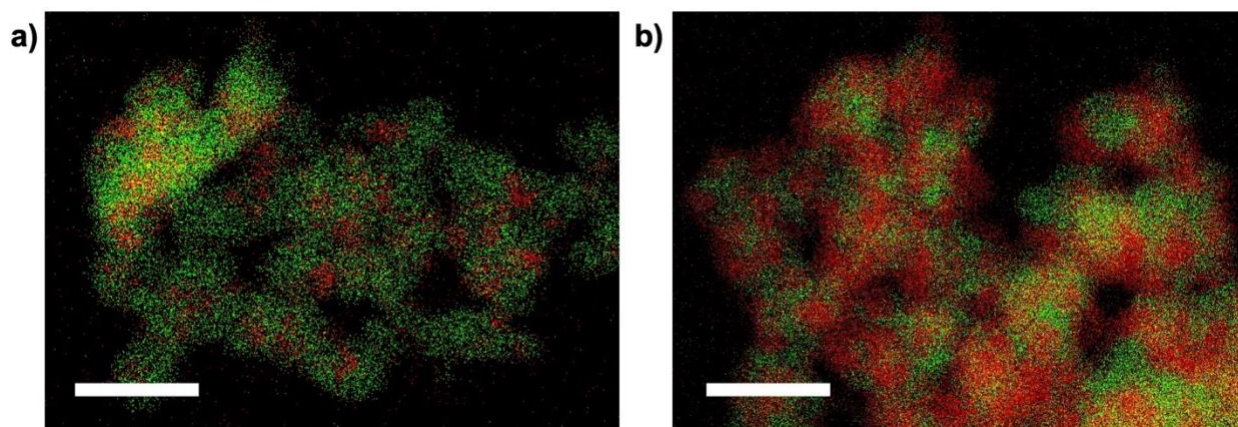
Figure 3.3. STEM-EDS of Cu-Ag material after catalysis
a) Physical mixture of monometallic Cu and Ag nanoparticles (50 Cu%at) b) Cu/Ag bimetallic (75 Cu%at). Scale bar corresponds to 40nm.

In both cases, during the catalysis, not only do the nanocrystals merge into a continuous structure, but also undergo a phase separation that results in a formation of larger monometallic domains, not very different from the size reported for bulk Cu-Ag foil (10-15 nm in length). Clearly, the catalytic conditions provide sufficient energy to restructure the Cu-Ag material into a more thermodynamically stable state which has a lower surface area as well as less unfavorable Cu-Ag interface. In the future, appropriate measures of nanoparticle isolation to avoid restructuring can be explored, such as conductive polymers[98] or physical barriers.[99]

3.2 Catalytic performance of Cu-Ag bimetallic nanocrystals vs. Cu and Ag nanoparticle physical mixtures

While the ability to precisely control the amount of Cu-Ag interface as well as probe potential electronic effects due to a different amount of coupling between the metals was not accomplished, the catalytic results are still worth elaborating. When comparing the Cu-Ag results with the sample of pure Cu NPs, the two most visible trends are: 1) significant decrease in H_2 production and 2) an increase in oxygenates, i.e., species containing at least one O atom except CO and formate (Figure 3.4). Such trends correlate well with the results observed on bulk Cu-Ag foils.[17,45] Another clear change is an increase in CO production following the amount of Ag, which can be explained by the fact that Ag atoms have very weak binding to this molecule and will not reduce CO further. As H_2 production is a competitive reaction to CO_2RR and considered undesired, the decrease in its selectivity for Cu-Ag materials is very beneficial. That being said, its mechanism is less understood than the increase in CO production. Likely, it is caused by the weak O and H binding of Ag that decreases the likelihood of H_2O interactions and H adsorption needed to produce H_2 (Figure 1.6b).[100]
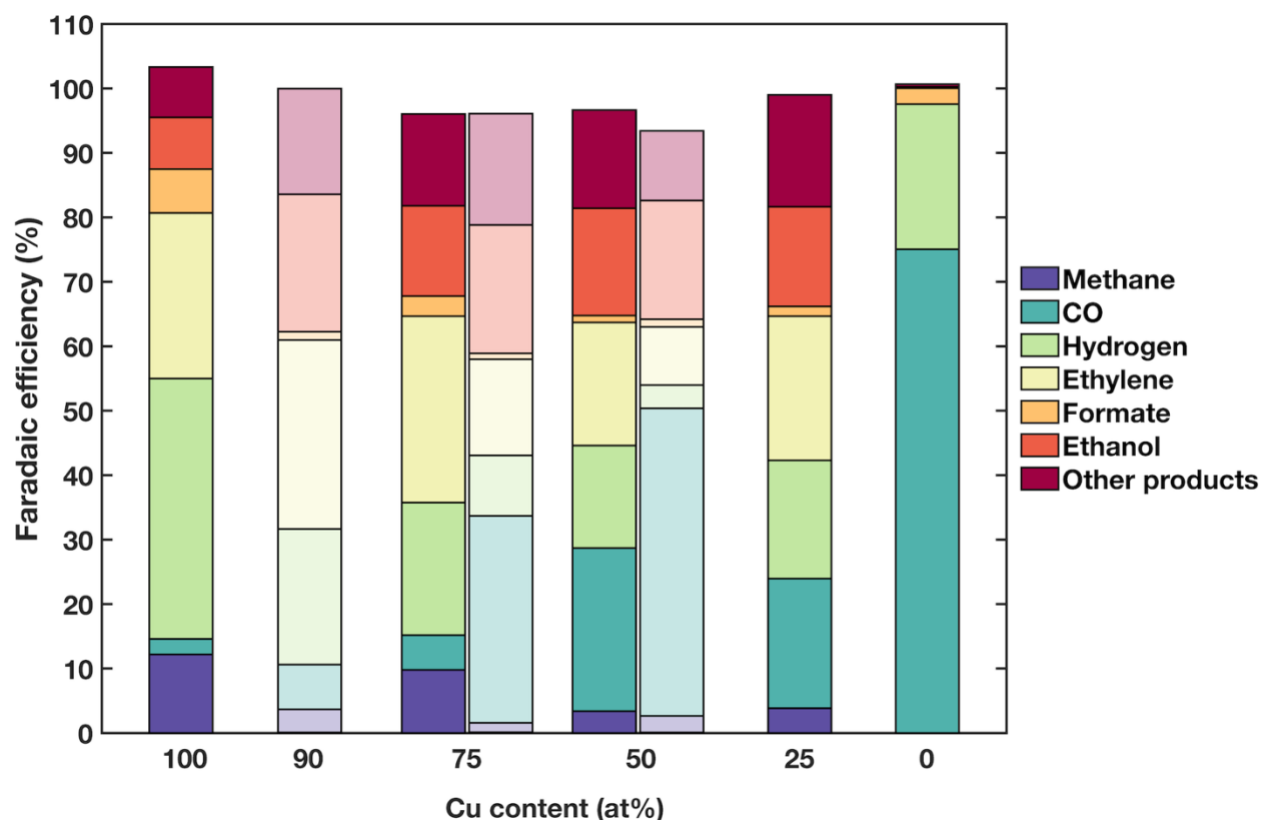
Figure 3.4. Faradaic efficiencies for Cu-Ag physical mixtures and bimetallic samples
Physical mixtures and monometallic samples are denoted by the bars with darker colors, while bimetallic samples are denoted by fainter colors. The measurements were performed at -1.1V vs. RHE.

The high oxygenate production (Figure 3.5), a second feature that distinguishes Cu-Ag materials, is not only very interesting from the perspective of elucidating the formation mechanisms of various CO_2 reduction products, but could also be industrially relevant if the selectivity was further pushed towards high yields of ethanol production. Ethanol is widely used as fuel and as a precursor to a variety of chemicals. At present, it is impossible to fully decouple ethanol production from other minor liquid products and its generation is roughly equal to that of the rest of oxygenates. The definition of oxygenates exclude CO and formate because these two species can be formed by other metals than Cu and take only two electrons for the reduction from CO_2.[101]

Regarding the mechanism of the increase of oxygenates production on Cu-Ag materials, there are no definitive conclusions yet but it is likely that the phenomenon is connected with the change in H and O bonding. As the H_2 evolution is less likely, there should be more CO interactions which in turn should increase the likelihood of C-C coupling. However, as O binding is also weakened, products are more likely to detach from the catalyst surface when oxygen atoms are still present in the molecules, rather than continuing towards the more reduced form of ethylene. As O binding is up to five times more sensitive to strain effect than CO binding,[102] it is likely that

the presence of both Cu and Ag atoms with their lattice mismatch is indeed causing an overall decrease in oxophilicity.
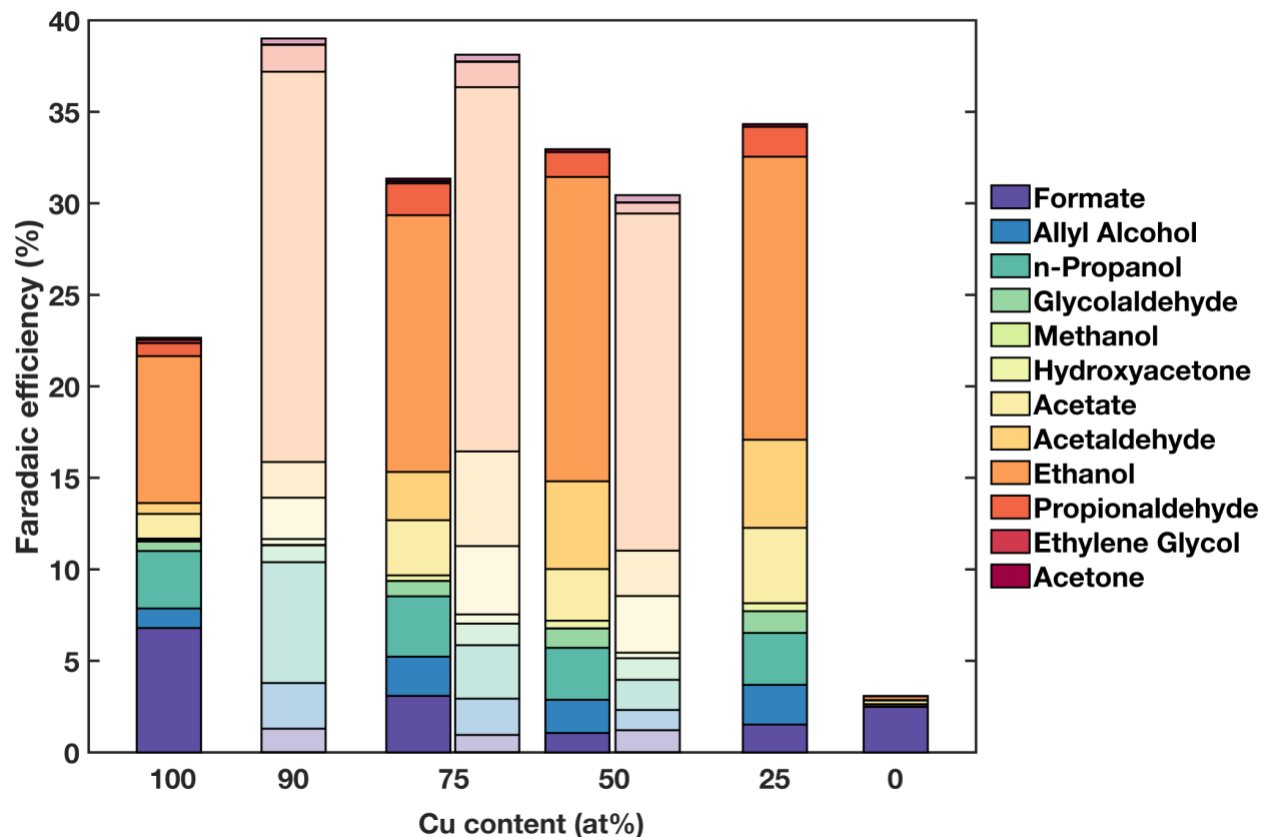
Figure 3.5. Faradaic efficiencies of liquids for Cu-Ag physical mixtures and bimetallic samples

Data were obtained for the same samples as in Figure 3.4. Darker colors correspond to physical mixtures, and lighter colors correspond to bimetallic samples.

The catalytic activity has also been assessed based on the measured current densities (Figure 3.6). We report the geometric current, based on the surface area of the substrate, and the normalized current, calculated by determining the electrochemically active surface area (ECSA).[103] Current has been averaged throughout the run, excluding the first five minutes due to double-layer charging, Cu_2O reduction, and stabilization. The ECSA was determined by measuring the double-layer capacitance of the material. While helpful, the final result must be approached with a degree of caution because the calculation assumes that the value of capacitance does not change for all probed substrates, and since nanoparticles are known for having different electrochemical properties than bulk,[104] this assumption may not be correct. Nevertheless, we found this method to give more reliable results than the Randles-Sevcik equation[41] and it is certainly more insightful than measuring the geometric surface area from SEM images.[40]
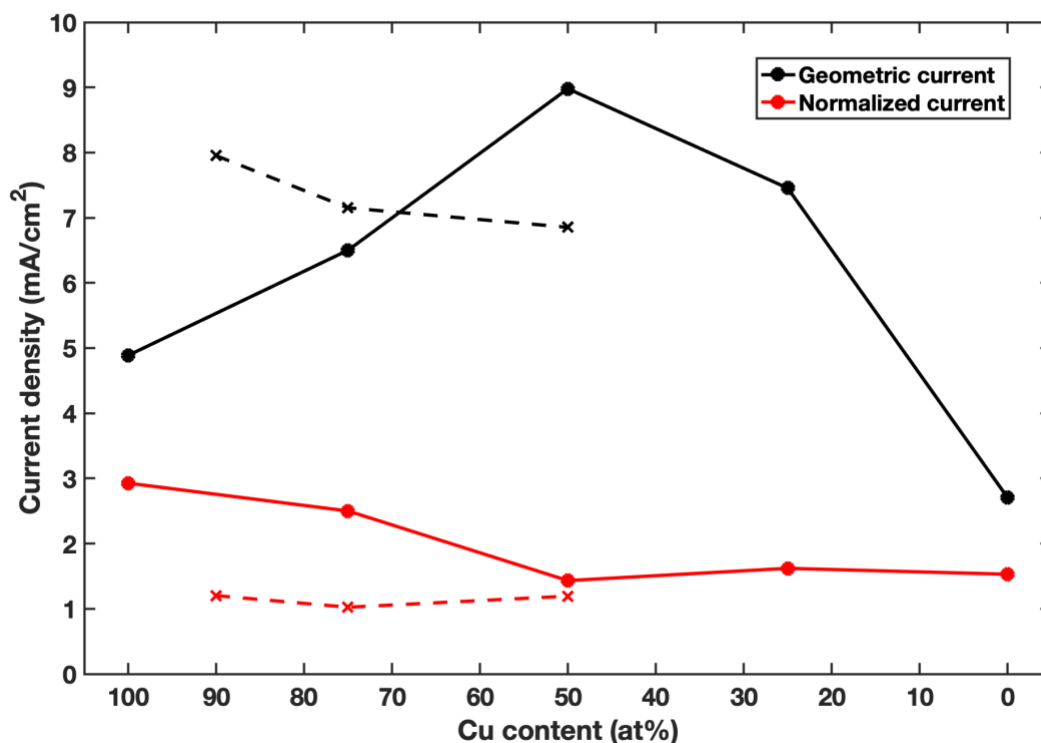
Figure 3.6. Geometric and normalized current densities for Cu-Ag runs
The solid line denotes physical mixtures, and the dashed line denotes bimetallic samples.

The geometric current for physical mixtures goes through the maximum for the 50:50 sample (Figure 3.6). Since all tested samples were equalized to the total number of atoms, this suggests that there is some beneficial effect of combining Cu and Ag nanoparticles. Possibly, it is a result of Cu and Ag NPs being slightly different sizes (Cu: 7-8nm; Ag: 5-7nm) which created a rougher surface, effectively increasing the electrochemical surface area. This hypothesis seems to agree with the ECSA measurements, as the trend for normalized current is different and shows a decrease in activity from pure Cu to pure Ag. The bimetallic samples displayed a more uniform performance and after normalization, the activity seems worse than for physical mixtures. We did not aim at optimizing the current densities, however, so it is likely that we have not found the optimal conditions for the particles regarding loading as well as ligand coverage.

Regarding the catalytic differences between physical mixtures and bimetallic samples, the latter resemble pure Ag at higher Cu content than physical mixtures do. This can be rationalized knowing the morphology of individual Cu-Ag bimetallic particles used in the experiment and synthesized by the method of galvanic exchange described in Chapter 2. At 50 at%, the particles almost exclusively have Ag on the surface as they are core-shell, Cu@Ag (Figure 2.1). A small fraction of imperfect core-shell particles would not explain a substantial production of oxygenates, which pure Ag surface is not capable of catalyzing. Instead, the particles underwent significant restructuring which must have drawn enough Cu to the surface of the catalyst to make further CO reduction possible. This fact is indicative of how important intermediate absorption can be in the morphological restructuring of tested catalysts. Nevertheless, the total amount of surface Ag must still have remained higher than in the case of physical mixtures. The high selectivity towards CO

is somewhat regrettable as 50:50 Cu@Ag bimetallic sample displayed a remarkably low selectivity towards H_2 production, less than 5%. If it was possible to maintain the low H_2 production but increase the fraction of continued CO reduction, the surface created from 50 at% bimetallic particles would be quite promising for catalytic applications.

It is also worth noticing that the 90 at% bimetallic sample bears the closest resemblance to the 75 at% physical mixture suggesting that for bimetallic structures, a small amount of Ag becomes more catalytically relevant. This is in agreement with the bulk foil studies that showed that while Cu and Ag do not mix at all at room temperatures, a monolayer surface alloy, at least on Cu(100) is possible.[105] We ruled out a possibility of a phase-pure monolayer of Ag on the bimetallic particles formed during synthesis,[106] but it is not impossible that under catalytic conditions, some surface alloying occurs.[45] More studies, especially ultra-surface-sensitive ion scattering spectroscopy (ISS), are needed to explore this possibility. Focusing on adding an even smaller amount of Ag could also be enlightening, but such studies may turn out to only reproduce the already-existing results on bulk foil if one does not have better control over the morphological change at the nanoscale.

3.3 Effect of Cu-Ag loading on the catalytic performance

Another difference between bulk and nanomaterial catalysts is the ability to adjust the loading of the latter on the substrate. We set to probe how the loading of the catalyst, in this case, the physical mixture of Cu and Ag particles (50:50), affects the selectivity, and we observed a significant change (Figure 3.7). As shown, loading optimization is a key step in obtaining desired catalytic performance. It turned out that the most favorable selectivity, i.e., the highest production of C_2 and C_3 products as well as the lowest H_2 production, occurred for the intermediate regime when the drop-casting solution was diluted by a factor of 5. When the sample was diluted 20 times more, such that the particles no longer covered the whole substrate (Figure 3.8), the activity towards CO production was much higher.
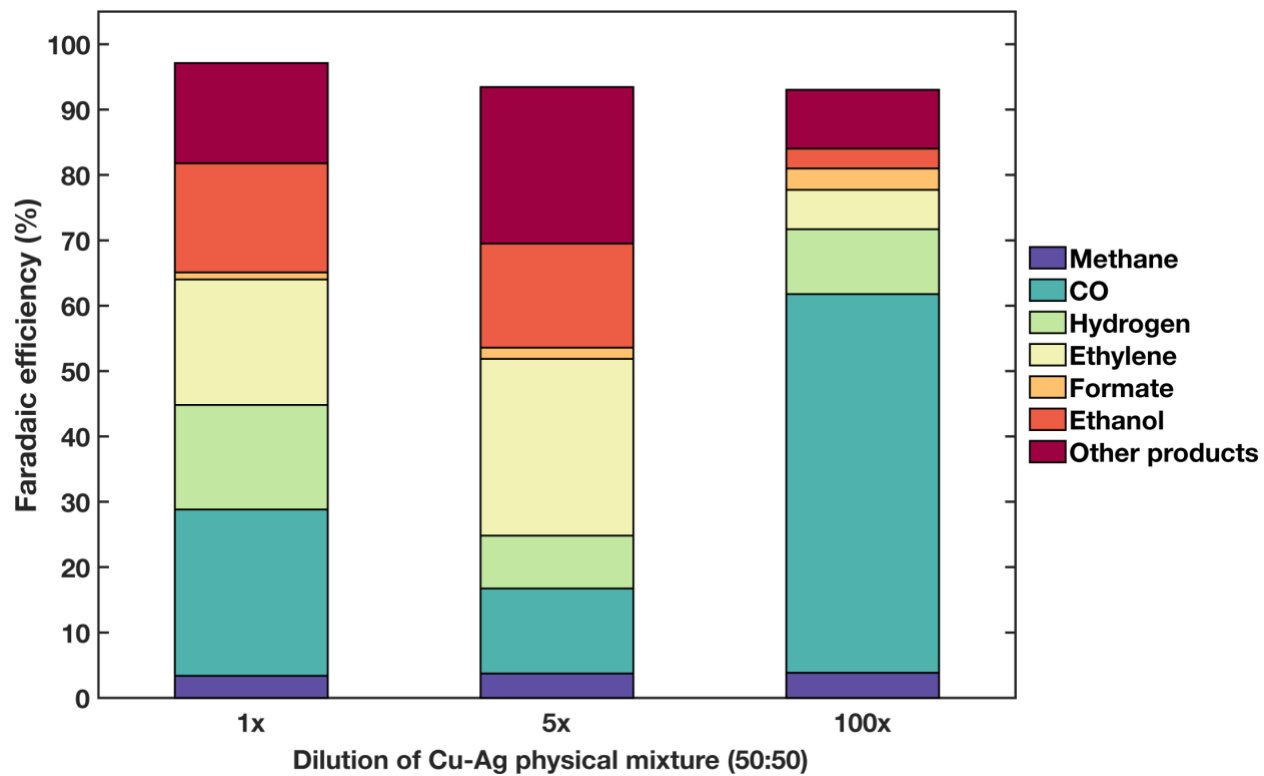
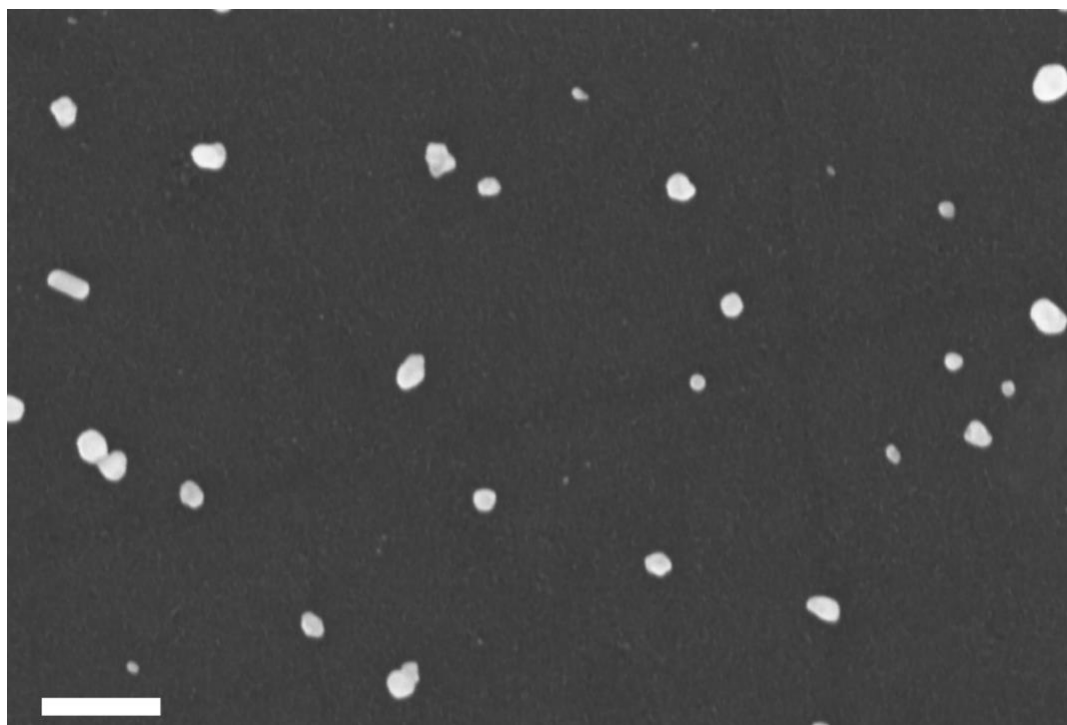**Figure 3.7. Dilution effect on the faradaic efficiencies**

Figure 3.8. SEM image of 100x dilutes sample after catalysis.
-1.1V vs. RHE for 60 min. Physical mixture of Cu and Ag NPs (50:50). Scale bar corresponds to 200nm.

The loading effects of nanoparticles and their effect for catalytic activity of CO_2 reduction have not been explored in the literature as much as the selectivity and efficiency changes based on other characteristics, such as particle shape or elemental composition. Kim *et al.* studied the effect of loading for plain Cu nanoparticles, synthesized by the same method and with the same ligand as described in this dissertation.[42] They have also observed strong loading dependence, with their highest reported loading being the most selective towards C_2 and C_3 products. As the particles undergo significant morphological restructuring under the relevant catalytic conditions, it was proposed that based on the loading and relative particle proximity, the final morphology will be different and may display different catalytic properties. While the researchers were not able to conclusively explain what determines the high selectivity towards given products, they suggested that the active site motifs must be unique enough that cannot be simply reproduced by starting with larger Cu cubes that will not undergo an equivalent morphological restructuring.

Regardless of what exactly causes CO_2 reduction selectivity to be quite sensitive to the particle loading, this effect also exists for Cu-Ag samples and deserves further attention. It is certainly possible that the morphological change occurring during the reaction results in structures different enough that their active sites display different chemical selectivity. It is also possible that the modeling perspective of intermediates binding to specific atoms is not sufficient to predict the catalytic outcome, as the diffusion layer in the process is large enough that molecules can migrate from spot to spot and interact with several different sites before the final product appears.[9] Furthermore, the substrate should also be considered as it can either modify the properties of the deposited catalyst[107] or it can perform its own catalysis. Indeed, different CO_2RR performance has been seen on flat glassy carbon versus three-dimensional carbon paper, although it is unclear whether the change comes from the difference in geometry or chemical properties of the support.[42] Finally, the existence of organic ligands, not present for bulk materials, shall be considered too. Overall, the nanoparticle catalytic system is very complex, and it certainly calls for a better fundamental understanding which could elucidate the effects of selectivity dependence on loading.

To complete the analysis of the dilution effect, we compared the geometric and normalized current densities using the same techniques as described in the previous section. The geometric current decreases by almost an order of magnitude as the result of dilution (Figure 3.9). It is curious to see a substantial drop between 1x and 5x dilution even though in both cases the films covered the whole substrate. Likely, at higher concentrations, the particles assemble into rougher forms with more surface area. This seems to be confirmed by the ECSA measurement showing that the normalized current density has the opposite trend to the geometric one. Per site, particles are the most active when they are most diluted. It may be possible to simultaneously benefit from high selectivity towards oxygenates and high current densities by switching the substrate to a three-dimensional support such as carbon paper.
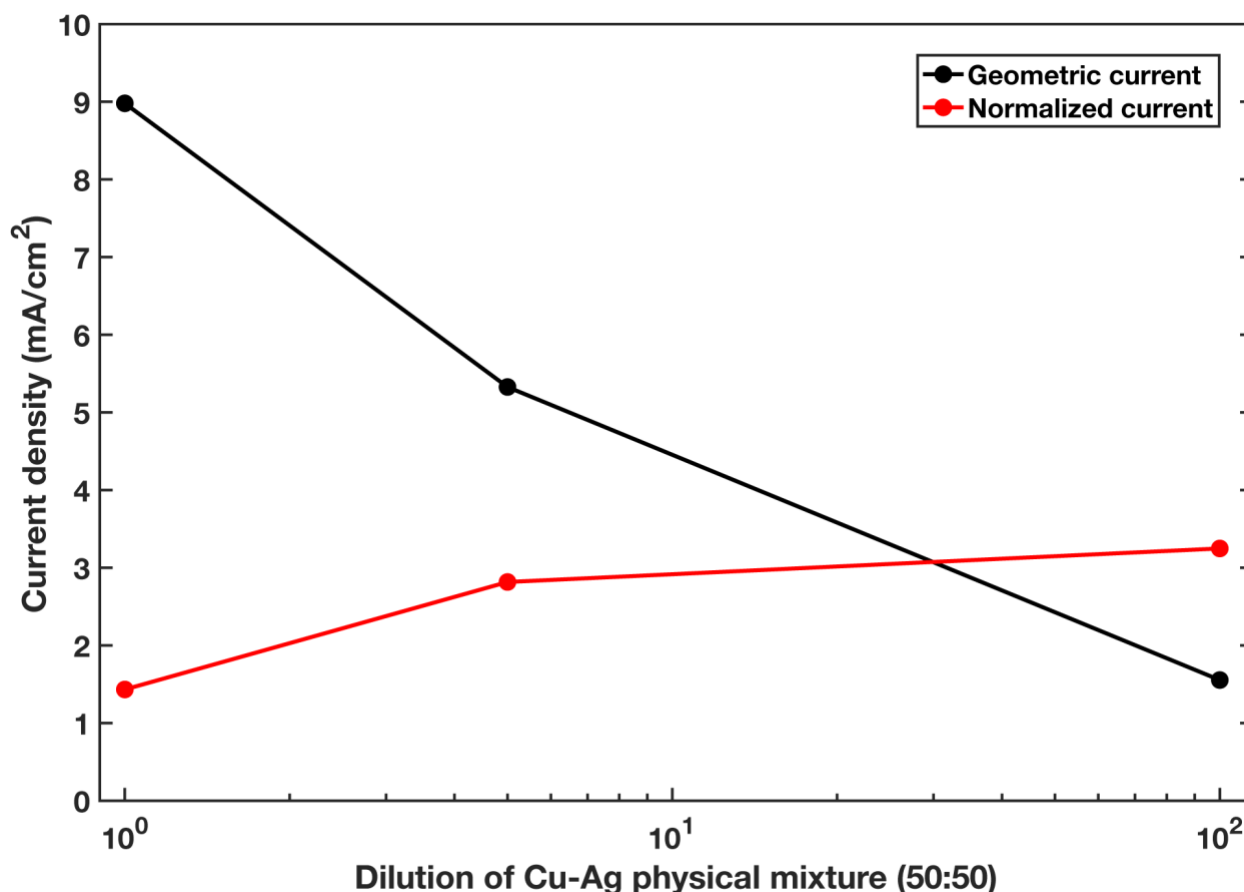
Figure 3.9. Geometric and normalized current densities for the diluted samples

3.4 Conclusion and future directions

Despite a focused effort of turning electrochemical CO_2 reduction into an industrially viable technology that could be deployed on a massive scale required for energy storage of renewable electricity, we still do not have catalysts efficient and selective enough to yield most enticing products, such as ethylene and ethane. As discussed in Section 1.3, breaking the scaling relationships between the binding of various reaction intermediates will probably be necessary to ever achieve much higher catalytic selectivity. For this purpose, mixing several metals seems to be one of the most promising strategies and Cu-Ag surfaces have shown progress in obtaining more C_2 and C_3 products.

Nevertheless, the quest for catalysts making just one product beyond CO reduction is far from over. Further fundamental understanding is needed, as it can not only propel the field of CO_2RR but also elucidate other electrocatalytic process and deepen our knowledge of chemical surface interactions under relevant conditions. In this pursuit, one should not only consider the catalytic benchmarks, such as current density and faradaic efficiency, but also study the dynamics of the reaction and the associated morphological changes, since the surface of the catalyst is one of the most important factors shaping the chemical process.

44

Even simplest Cu-based bimetallic catalysts, i.e., foils, undergo morphological changes under the catalytic conditions. There have been reports of Cu-Ag surface alloy formation[45] and catalytic sites formed as the result of Cu_2O reduction.[46] When one aims to engineer a specific surface geometry or use nanomaterials that need to be dispersed onto a substrate, the catalytic system becomes even more complex and the range of possible catalytic outcomes widens. Special attention needs to be paid to thermodynamics as the electrochemical conditions provide enough energy to relax systems into more stable conditions: lower surface area, fewer undercoordinated sites, and less unfavorable bimetallic interface. This has undoubtedly occurred for the physical mixtures of monometallic Cu and Ag NPs as well as bimetallic Cu-Ag crystals which sintered into a continuous, poorly-controlled structure (Figure 3.3).

Despite the inability to probe the effect of Cu-Ag interface on the catalysis carefully, we were still able to observe more general trends driving this reaction. For both physical mixtures and bimetallic samples, we identified an optimal elemental ratio which had significantly higher faradaic efficiencies towards oxygenates and lower H_2 production rates than systems of pure Cu (Figure 3.4). The optimal ratio was found at lower Ag content for bimetallic samples than for physical mixtures. While both configurations sintered into a continuous film, it is possible that the morphological restructuring occurred somewhat differently for both and was responsible for the observed catalytic differences.

We have also observed a significant shift in catalytic selectivity based on the catalyst loading. Similar to pure Cu catalysts, low loadings favored C_1 products, while higher loadings showed more selectivity towards C_2 and C_3 products. This is important information both from practical and fundamental standpoints. Catalyst loading optimization will be a crucial step in building any device meant for industrial applications. Also, the amount of nanocrystals on the surface seems to lead to a formation of different surface sites; potentially, there is a synergistic effect between local atomic environments which would explain why small Cu-Ag clusters produce more CO and less oxygenates than the large ones do.

A careful study of Cu-Ag interface could be attempted again if the morphological restructuring was to be prevented. Recently, researchers used Nafion suspension to stabilize larger (>20 nm) Cu-Ag structures.[98] This method is not perfect as it leads to significantly higher H_2 selectivity proving that Nafion is not an innocent bystander, but instead it either blocks some catalytic sites or changes their binding affinities. Furthermore, it is much harder to perform high-resolution electron microscopy on materials covered with organic matter, so it is unclear whether Nafion prevents surface restructuring or just stabilizes the particle size. Nevertheless, attempting strategies that will prevent sintering is certainly a good avenue of research, although inorganic approaches such as nano-pores may be more appropriate.[99]

Perhaps, it is even more crucial to maintain the focus on deepening the fundamental understanding of the relationship between the morphology of active sites and the catalytic activity. Cu-Ag surfaces should be probed with high-resolution surface-sensitive tools, ideally obtaining the information *in operando*. While undoubtedly challenging, such approach will probably bring more results than testing a variety of possible nano-structured catalysts in different cell configurations, since as of right now, our ability of engineering complex morphologies does not

seem to be matched by a deep enough understanding of the reaction dynamics and the relevant structure-function relationships.

3.5 Supplementary information
3.5.1 Used materials and synthesis

Materials
Copper(I) acetate (Sigma-Aldrich, 97%), n-Tetradecylphosphonic Acid (abbrev. as TDPA, Sigma-Aldrich, 97%), Trioctylamine (Sigma-Aldrich, 98%), Isoamyl ether (Sigma-Aldrich, 99%), Silver Trifluoroacetate (Sigma-Aldrich, ≥99.99% trace metals basis), Silver Nitrate (Sigma-Aldrich, 99%), o-Dichlorobenzene (abbrev. as DCB, Sigma-Aldrich, 99%), Oleylamine (Sigma-Aldrich, 70% technical grade), 1,2-Dodecanediol (Sigma-Aldrich, 90%), Cesium Carbonate (Sigma-Aldrich, 99.995% trace metals basis), Carbon Dioxide (Praxair, 99.99% purity) Water (Milli-Q, 18.2 MΩ), Hexane (Sigma-Aldrich, mixture of isomers, anhydrous, ≥99%), Ethanol (Sigma-Aldrich, pure, anhydrous, ≥99.5%), Isopropanol (Sigma-Aldrich, anhydrous, 99.5%). All materials were used without further purification unless specified otherwise in the experimental methods.

Synthesis
Cu and Cu-Ag bimetallic nanocrystals were synthesized by the same methods as described in Section 2.7.3.

Ag nanocrystals were prepared according with the literature method.[108] Briefly, 0.1 g of $AgNO_3$ was dissolved in 5 mL of DCB and 1 mL of oleylamine. The solution was injected into 10 mL of DCB solution containing 100 mg of dodecanediol at 180 °C under argon atmosphere. After about 5 min, the temperature was cooled down to room temperature and subjected to two ethanol-hexane washing cycles using air-free techniques (more details on washing in Section 2.7.3). The nanocrystals were stored in a glovebox and kept away from light to avoid any potential precipitation.

3.5.2 Catalytic experimental methods

Fabrication of electrodes
Glassy carbon disks (Type 2, Alfa Aesar) with diameter of approximately 25 mm of were polished using 1 μm alpha alumina (CH Instruments) and 50 nm gamma alumina (CH Instruments). The disks were rinsed with Milli-Q water, sonicated for 2-3 min, and blown dry with nitrogen. Before the first use and when needed, electrodes were additionally kept in 1.5M ultra-purity HNO_3 for 30 min. The nanocrystal solutions were prepared such that the total number of atoms of Cu and Ag remained approximately constant. The concentration of all solutions was quantified with ICP-OES (more details in Section 2.7.4) and diluted with hexanes to 15 mM. Then, 100 μL of a nanocrystal solution was drop-casted onto the electrode and allowed to dried. Finally, 150 μL of ethanol was drop-casted and kept for 30 sec and afterward gently blown away with nitrogen.

Electrocatalysis
All electrochemical measurements were performed in a custom gastight cell machined from PEEK.[109] We followed protocols previously published in literature with minor modifications.[45,110] The cell was washed in 20 wt% nitric acid and sonicated in Milli-Q water before

experimentation. The working and counter (Pt foil, 99.99% trace metal, Sigma-Alidrich) electrodes were parallel and separated by an anion-conducting membrane (Selemion AMV AGC Inc.). The electrolyte volume of each electrode chamber was 1.8 mL and the exposed geometric surface area of each electrode was 1 cm^2. The Ag/AgCl reference electrode (LF-2, Innovative Instruments Inc.) was referenced against the ET070 Hydroflex™ Hydrogen Reference Electrode (eDAQ, Inc.). 0.1 M $CsHCO_3$ in Milli-Q water was used as the electrolyte, which was prepared by bubbling CO_2 through a solution of half the molarity of Cs_2CO_3, producing a solution of pH 6.8 after approx. 2 h. Cesium cation was chosen, as it has been shown that it enhances C_2 and C_3 selectivity.[111] Both electrode chambers were sparged with CO_2 at a rate of 5 sccm for 10 min prior to and throughout the duration of all experiments.

Electrocatalysis was performed using a Biologic SP-200 potentiostat. All electrochemical measurements were recorded versus the reference electrode and converted to the RHE scale. Potentiostatic electrochemical impedance spectroscopy (PEIS) was used to calculate the uncompensated resistance (R_u) of the electrochemical cell by applying voltage waveforms about the open-circuit potential with an amplitude of 20 mV and frequencies ranging from 100 Hz to 300 kHz.[45] The chronoamperometry experiments were performed by applying the potential equivalent to -1.1V vs RHE and holding it for 1 h.

Quantification of the products
Gaseous products were quantified using a gas chromatograph (MG-5, SRI Instruments) with 12-foot Hayesep-D column and thermal conduction (TCD) and flame ionization (FID) with a methanizer detectors. The effluent was sampled before the electrocatalysis started and then every 16 min. The initial temperature of the run was 50 °C for 3 min, then increased to 180 °C for the rest of the run.

Liquid products were quantified using nuclear magnetic resonance (NMR). 1D ^{1}H NMR was performed on Bruker Avance 700MHz spectrometer with an inverse cryoprobe using a water suppression technique.[112] Peak areas were converted into concentration using calibration curves.[7] Briefly, standard curves were made using purchased chemicals over the concentration range of interest, with the internal standard DMSO (10mM) in 0.1 M $CsHCO_3$. Liquid samples were stored in the fridge to limit evaporation of volatile products. The coulombs needed to produce that concentration of each chemical were calculated and divided by the total coulombs passed during the chronoamperometry to determine the faradaic efficiency.

3.5.3 Other characterization methods

Scanning electron microscopy images of electrodes were acquired using a Zeiss Gemini Ultra-55 field emission SEM with an InLens detector, 5 kV accelerating voltage, and 3 mm working distance. For STEM-EDS, sintered material was transferred onto a TEM grid (Electron Microscopy Sciences, CF300-Au-UL) by wetting the grid with methanol, placing it on top of the electrode and applying pressure with a microscope slide for a few seconds. Imaging was performed on FEI TitanX with an EDS detector (more details in Section 2.7.4).

Chapter 4. Sintering of Cu nanocrystals during electrochemical CO_2 reduction

4.1 Electrochemical sintering proposed mechanisms

As discussed in Chapter 1, significant improvements in the efficiency and selectivity of CO_2RR require carefully nano-engineered surfaces that break the scaling relationships of binding strength by such motifs as high-energy facets and low coordination numbers. Unfortunately, the same motifs are most likely to undergo morphological restructuring when given enough energy. Since catalyst stability is a crucial aspect of its usefulness, it is worth investigating the changes of Cu nanocrystals that occur during the electrochemical CO_2 reduction. In the future, the Cu-based alloys should also be studied, but for the sake of simplicity and applicability, we chose to start with the most common CO_2RR catalyst that generates C_2 and C_3 products.

The morphological changes of Cu NCs that were observed by our group[40] as well as others,[41,42] can be described as sintering, i.e., loss of overall surface area by increasing in average size of particles. Recently, two groups studied the dynamics of larger (>15 nm) Cu nanocubes under the CO_2RR conditions, which also undergo some sintering, albeit much slower due to the size difference.[113,114] These publications focused on changes occurring to individual particles, not on the collective behavior. Regardless of whether sintering is caused by thermal or electrochemical processes, it can be broadly classified into two categories: particle migration and coalescence (PMC) and atomic ripening (AR) (Figure 4.1).[32] PMC involves a coordinated motion of entire nanoparticles or metal clusters that are mobile enough, due to temperature or other reasons, to diffuse and coalesce into each other.[115] In AR, more commonly known as Ostwald ripening, metallic atoms move from smaller particles to larger ones, either on the surface or through the reaction medium (vapor, gas, electrolyte).[116] The newer name AR proposed by Goodman *et al*.[32] emphasizes that the atoms taking part in ripening sometimes travel as bound and stabilized species rather than bare atoms. Both PMC and AR are motivated by the energetics of lowering available surface area, which is thermodynamically favorable.
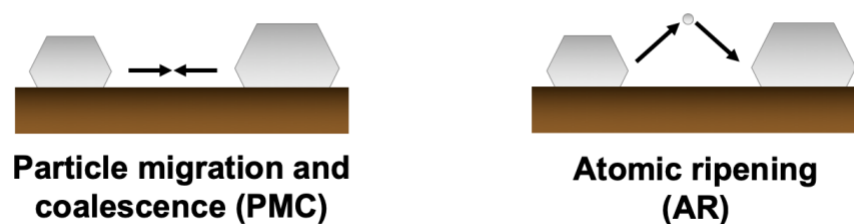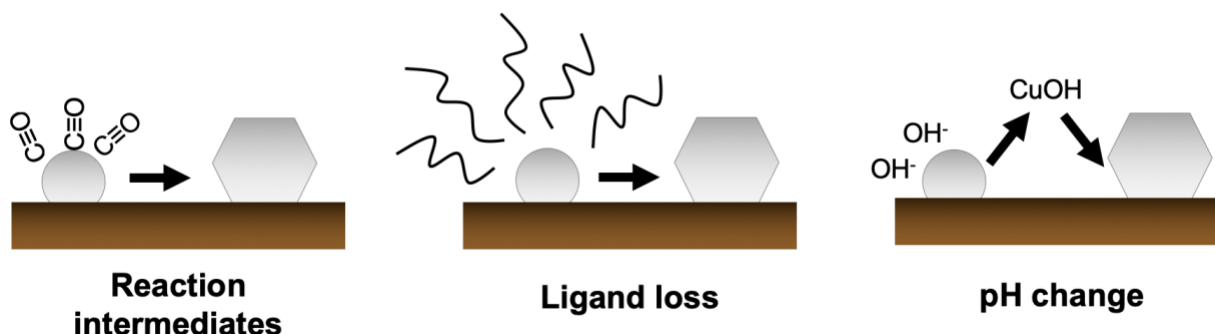
Figure 4.1. Schematic illustration of sintering mechanisms and potential driving forces in the case of CO$_2$RR

While the existence of sintering can always be motivated by the loss of surface area, is it also worth to consider the potential driving forces that could enable this morphological process in the case of the electrochemical CO$_2$ reduction. The chemical environment of this reaction is quite complex as it involves a distinct nano-object, coated with organics and deposited on a given support, that is exposed simultaneously to electrochemical reducing bias, electrolyte, gaseous CO$_2$ as well as all the intermediates that are the result of the undergoing catalysis. Potential mechanisms hypothesized for the observed morphological changes involve: 1) reaction intermediates, such as CO, that restructure the particle surface and drive sintering, 2) ligand loss due to Coulombic repulsion under negative bias that significantly increase particles' mobility, and 3) OH$^-$ production that changes pH locally enough to etch and reshape the Cu surface (Figure 4.1). It is worth emphasizing that these driving forces may exist simultaneously, just like it is possible that both AR and PMC processes occur for the studied reaction. That being said, some factors are likely more important than others and therefore deserve a direct investigation to understand the sintering phenomenon under relevant catalytic conditions better.

We studied the system by running a series of electrochemical runs under default conditions of CO$_2$ reduction and analyzed the obtained morphologies by electron microscopy, both SEM and TEM. We decided to contrast the results with a variety of control experiments that exclude or modify one of the factors involved in the default operation (CO$_2$ gas, pH, electrical bias) in the hope of understanding which ones are most responsible for the investigated phenomenon. This is an ongoing research project in our group, and we hope to keep elucidating it further in the future.

4.2 Observed morphological change during CO$_2$RR

In order to benefit from high surface area, researchers often probe small nanocrystals for their catalytic activity. In the field of CO$_2$RR, there are several groups that performed the reaction with small, <10 nm in diameter, organically-synthesized, monodisperse and colloidally stable Cu nanocrystals bound with tetradecylphosphonate (TDPA) ligand.[40,42] Under catalytic conditions, the particles lose their monodispersity and sinter into larger ill-described structures. While this morphological change has been postulated as beneficial since it led to a higher selectivity towards C$_2$ and C$_3$ products,[42] it deserves an understanding as, without it, it will not be possible to stabilize more complex catalysts such as Cu-Ag bimetallic NCs.

To observe the sintering more easily, Cu NCs were spin-coated onto a flat, two-dimensional surface of glassy carbon that allows for easier and more precise imaging. The nanocrystals formed a sub-monolayer (Figure 4.2 a-b), which is far from the most optimal loading when it comes to selectivity towards C$_2$ and C$_3$ products, but it improves the quality of post-catalytic characterization.
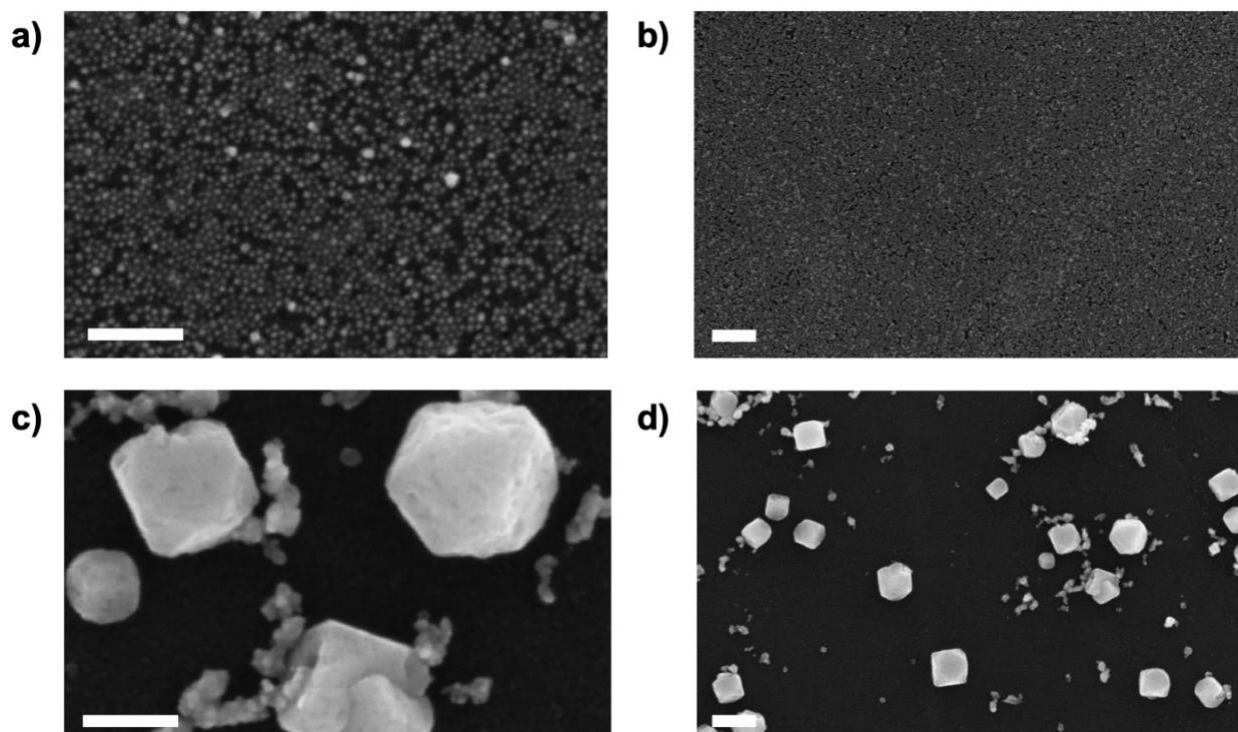
Figure 4.2. SEM images of Cu catalyst before and after 20 min of catalysis
a-b) Cu nanocrystals spin-coated onto the glassy carbon substrate before catalysis. c-d) The same electrode after 20 min at -1.05V vs. RHE. Scale bars correspond to 100nm for a) and c), and to 200nm for b) and d).

After 20 min of catalysis, the morphology of Cu nanocrystals has changed completely (Figure 4.2 c-d). Particles grew significantly, and their size distribution is no longer monodisperse. Interestingly, many large objects appear to be faceted, forming relatively regular geometric structures with flat surfaces. While based on several runs we performed we do not observe just one

dominating geometric shape, the faceting is very common. Nevertheless, there are also smaller structures, still larger than the original diameter of 7 nm, and they have more irregular shapes, visibly forming aggregates resulting from a PMC process, where particles migrate and coalesce together but do not form new facets. PMC seems to dominate under reducing conditions, so this observation is consistent with the literature.[31,117]

While initially the catalytic runs have been performed for 20 min, mainly as the reference to previous experiments performed in Chapter 3, the morphological change actually occurs on a significantly faster timescale. 1 min of catalysis proved to be sufficient to drive the particles towards complete restructuring (Figure 4.3a).
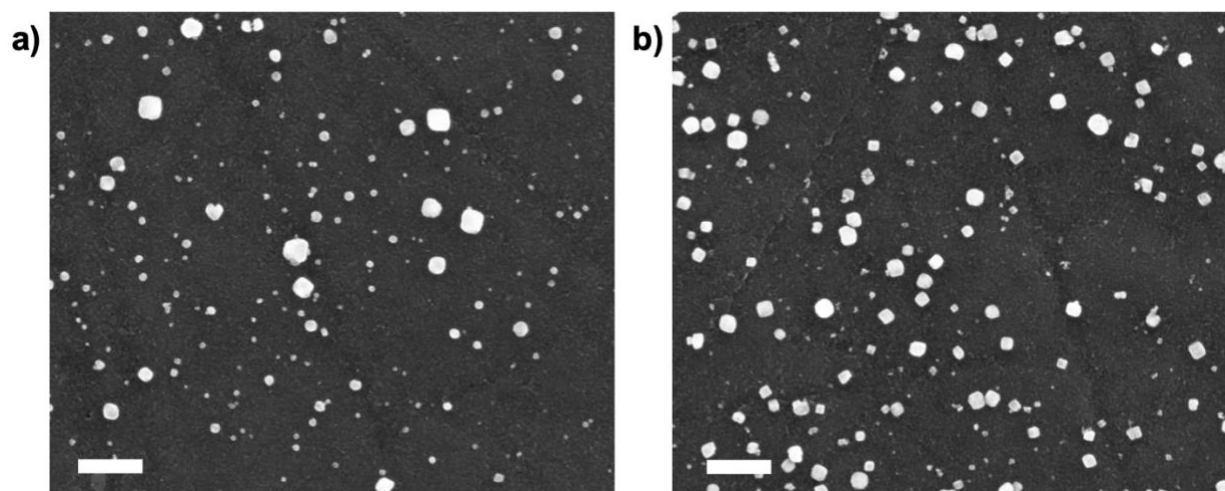
Figure 4.3. SEM images of Cu catalyst after different durations of catalysis
Left: 1 min. Right: 60 min. Both electrodes were exposed to -1.05V vs. RHE. Scale bars correspond to 200 nm.

The particles are somewhat smaller than the structures formed after 20 min (Figure 4.2d) or 60 min (Figure 4.3b) of catalysis, but this is not a dramatic difference considered the duration of tested runs. Sintering, at least in its initial stages, must be occurring relatively quickly compared to other known examples, especially thermal processes.[30,31] Nevertheless, the sintering proceeds in time, albeit much slower, and after 60 min the vast majority of the material is in structures that are on average more than 5 times larger in diameter than the original starting point. The size of 30 nm and more agrees with previous literature reports that did not observe sintering when using Cu particles larger than that size.[41] Presumably, the surface energy contribution for particles that large is small enough that it does not drive restructuring. This is less surprising than the mobility of 7nm Cu nanocrystals that undergo sintering even though surface atoms represent less than 0.1% of all atoms in the crystal.

4.3 Control experiments for probing the sintering mechanism

The simplest way to learn more about the sintering mechanism is perhaps performing a series of control experiments. If the morphology of particles under the changed conditions differs from the original, then the modified factor is crucial for the investigated process. To probe the

potential driving forces illustrated in Figure 4.1, we conducted experiments that changed pH, replaced CO_2 with argon, and probed the presence of ligands.

Although the global pH in the electrochemical cell is controlled by the carbonate buffer and stays around 6.8, which we confirmed by measuring it after the reaction, the local pH right by the electrode can be significantly higher due to the production of OH^- ion in the CO_2 reduction (Figure 1.3). The Pourbaix diagram predicts that Cu is most thermodynamically stable as solid at virtually any pH at the reducing potential of interest,[118] but such calculations are done for bulk and not small nanocrystals that are inherently less stable. Researchers have shown that cycling a Cu foil in the presence of halides forms Cu nanocubes.[119] While it is less likely than OH^- would have the same effect, we wanted to probe the hypothesis of OH^- etching Cu to CuOH which then almost immediately gets re-deposited as larger structures, which could account for the Wulff-like shape and faceting (Figure 4.2 c-d).

To test this hypothesis, we performed the electrolysis of Cu NCs in 0.1M KOH bubbling argon. We chose that gas because it is inert, and if pH is the main driver responsible for sintering, then the presence of CO_2 would not be necessary. Furthermore, CO_2 is effectively insoluble at pH of 13.[9] The same bias of -1.05V vs. RHE was applied for 20 min, but the obtained morphology was significantly different from structures resulting from CO_2RR (Figure 4.4). Cu NCs in 0.1M KOH formed dendritic structures, in what appears to be a standard PMC mechanism. Therefore, we do not believe that the buildup of hydroxide ions is a likely cause of sintering during CO_2RR, especially that the local pH is significantly lower than 13.
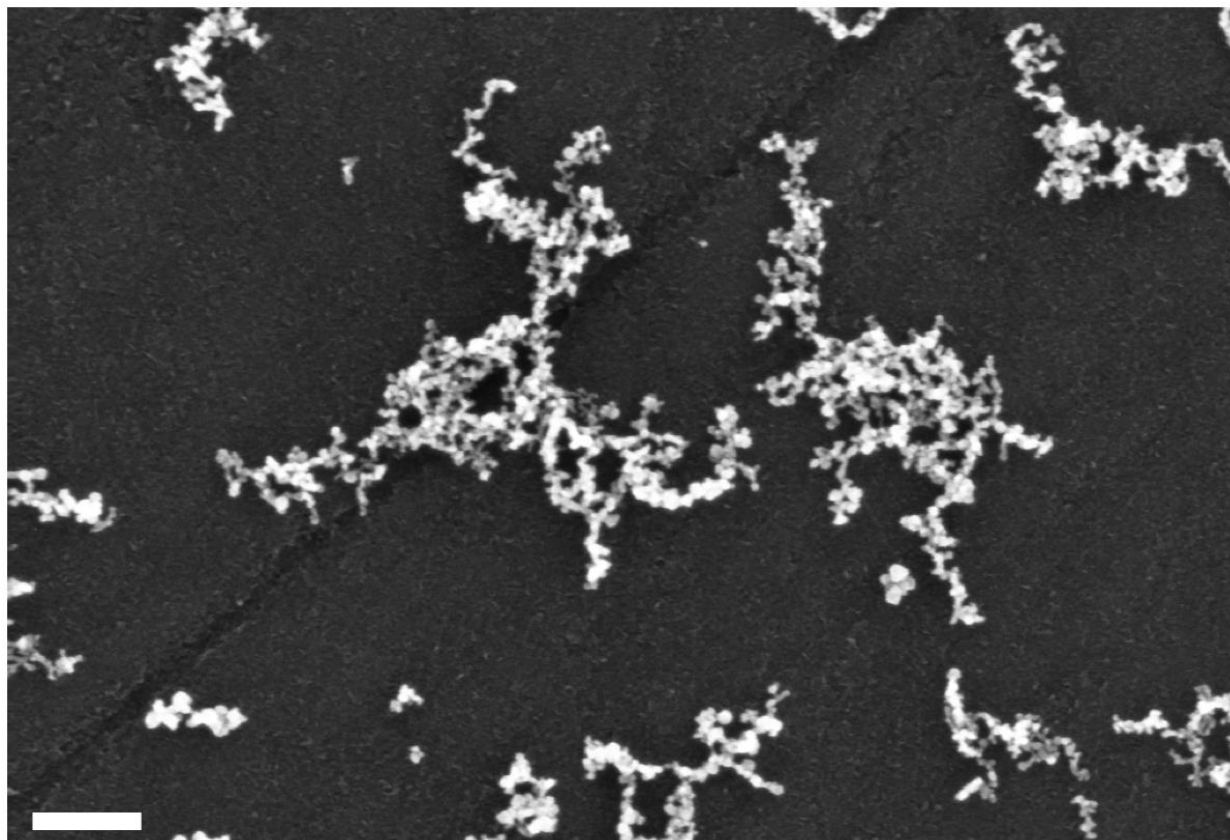
Figure 4.4. SEM image of Cu material after 20 min of electrolysis in 0.1M KOH
-1.05V at RHE, bubbling argon. Scale bar corresponds to 200nm.

The second probed hypothesis involves the binding of CO_2RR intermediates restructuring the surface. As shown by the test in 0.1M KOH, electrochemical sintering still occurs without the presence of CO_2, but it is exclusively dendritic growth driven by PMC. To further focus on the role of CO_2 and the reaction intermediates, we performed electrochemical runs in the standard carbonate buffer but bubbling argon instead (Figure 4.5). Again, the sintering was observed as particle changed shape and grew in size, but without the presence of CO_2, there was no formation of large and visibly faceted objects. The vast majority of structures looked dendritic as shown in Figure 4.5b. We identified a few more round objects, but these had clear domains made up of original Cu NCs.

When comparing Figure 4.5a and Figure 4.5b, especially the bottom, zoomed-in SEM images, it is easy to notice similarities between some of the sintered material from both runs. Presumably, all structures result from particle migration and coalescence, which is responsible for the uneven shape and the visible difference between domains that originated from the 7 nm Cu NCs. However, since we found no evidence of larger and faceted structure after electrolytic runs performed without CO_2, it is clear that this molecule and resulting intermediates such as CO play a role in the final obtained morphology. This role will be explored in more detail in the next Section (4.4).
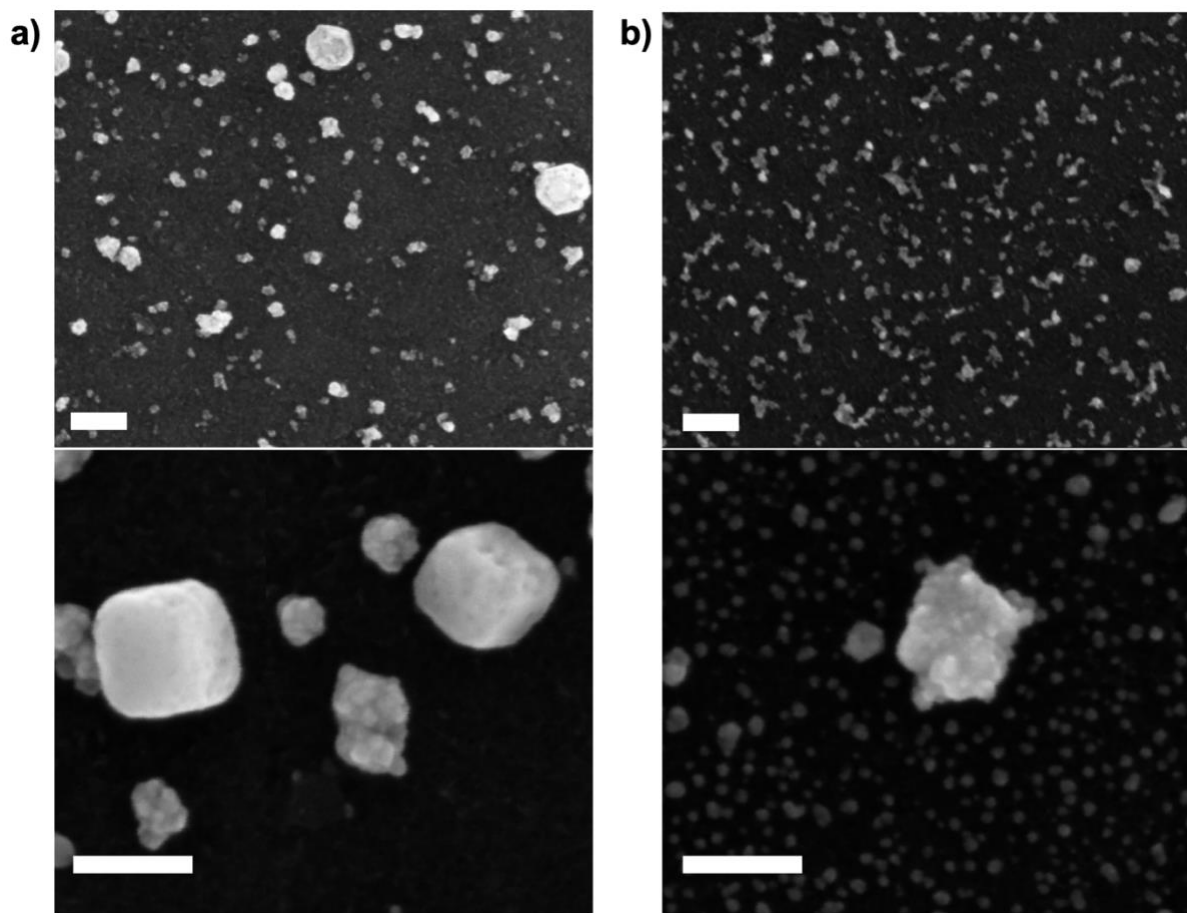
Figure 4.5. Comparison of sintering of Cu catalyst with and without CO₂

a) SEM images after electrocatalysis at -1.05V vs. RHE for 20 min with CO₂ bubbling b) SEM images after electrocatalysis in the same conditions except for bubbling argon. While some sintered material appears similar for both runs, the smoother faceted objects form only in the presence of CO₂. All scale bars correspond to 100 nm.

We have established that the presence of CO_2 is necessary to form the faceted structures, but since sintering also occurs without this molecule, we decided to probe the presence of ligands after the reaction. As hypothesized, ligand detachment could render the Cu nanocrystals mobile enough to diffuse on the substrate and coalesce together. Since Nafion, an organic conductive polymer, has been shown to stabilize the particles and prevent their sintering (while negatively affecting the selectivity, unfortunately),[98] the lack of any organic protective layer may be responsible for the observed PMC processes. The ligand in question, TDPA, binds to Cu through a negatively-charged phosphonate group. This bond is stable in the absence of electrical potential but strongly reducing bias charges Cu negatively which can lead to a Coulombic repulsion between the nanocrystal and the ligand head group.

The presence of ligands was probed with two techniques: infrared reflection-absorption spectroscopy (IRRAS) and X-ray photoelectron spectroscopy (XPS) (Figure 4.6). Both techniques

54

are highly surface-sensitive and capable of detecting a signal from a sub-monolayer of nanocrystals and their organic ligands. Both techniques also permitted probing the structures of interest directly on the glassy carbon substrate, without a need for any transfer which could perturb the results. IRRAS can detect C-H stretches from the TDPA's alkyl chain, while XPS can probe the P 2p and Cu 2p edges (Figure 4.6).
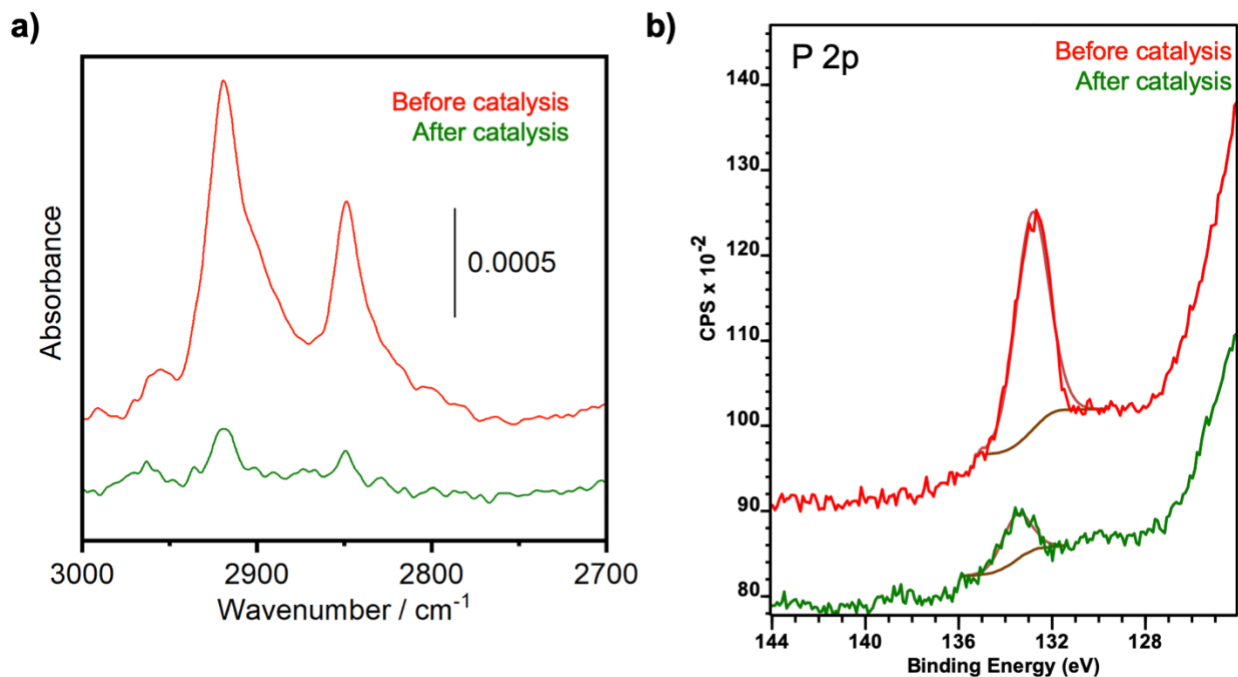
Figure 4.6. IRRAS and XPS spectra of the surface before and after catalysis
a) IRRAS spectra of the C-H stretch region of the electrode surface before (red) and after (green) electrolysis at -1.05V vs. RHE for 20 min with CO_2 b) XPS spectra of P 2p edge of the electrode surface (red) and after (green) electrolysis in the same conditions.

It can be postulated that the sintering associated with the PMC mechanism is indeed caused by the ligand loss and increased the mobility of the bare Cu surface. Cu NCs not exposed to CO_2 still sinter and form dendritic uneven shapes. As ligand loss has been observed by XPS in the argon experiment, such hypothesis seems plausible. Ligand loss seems to be enhanced by the presence of CO_2, which can be rationalized by the molecules binding through the surface and replacing TDPA.

4.4 Role of CO in the observed sintering

Ligand loss may be playing an important part in the sintering process, but the final observed morphology cannot be explained without the role of CO_2, whose absence clearly affects the formed structures. CO_2 reduction cannot occur without molecules binding to the catalyst, and such binding may restructure nanoparticle surfaces based on the surface energy change.[120] The intermediate that is most likely responsible for the formation of smooth structures is CO, which backbonds to metals and is present in higher concentration on the surface than other intermediates.[12] To understand this phenomenon better, we conducted electrolysis bubbling pure CO instead of CO_2 (Figure 4.7), as

well as also transferred the sintered material onto TEM grids for higher-resolution imaging and electron diffraction.
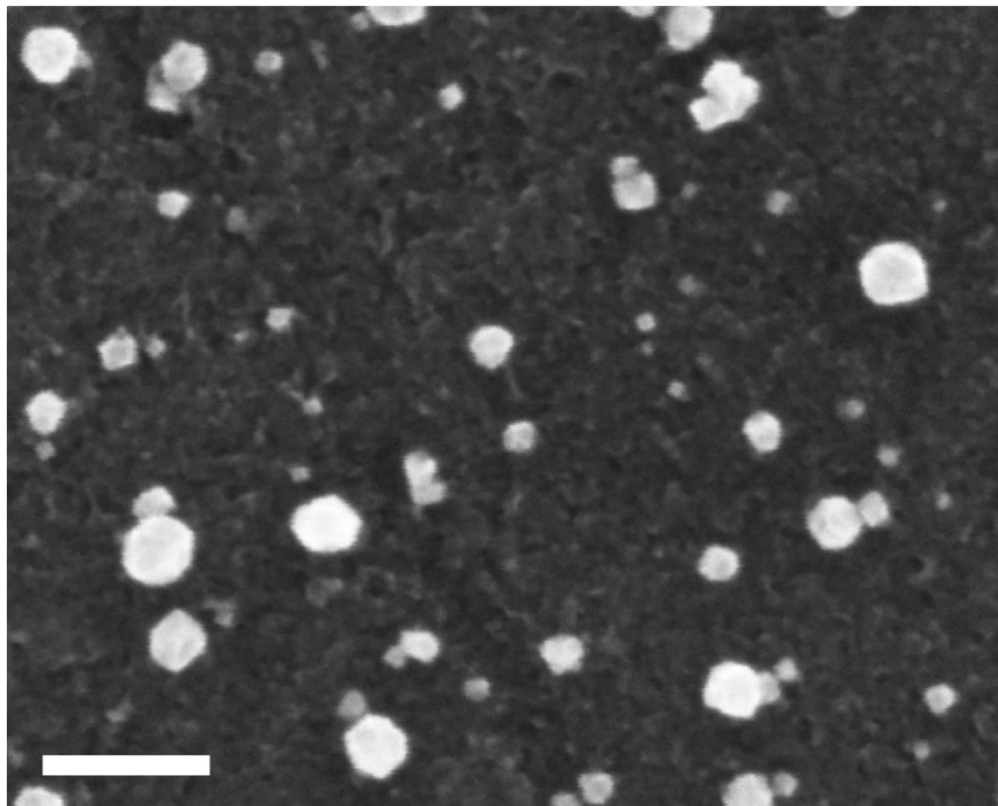
Figure 4.7. SEM image of Cu material after electrolysis with CO
-1.05V vs. RHE for 20 min. Scale bar corresponds to 100nm.

SEM reveals that CO has a similar effect on sintering as CO_2 does. Larger, round and perhaps faceted objects are observed again. This supports the hypothesis of CO being the relevant intermediate for modification of the sintering process. Naturally, if CO_2 itself was responsible for this role, then the CO run would reveal a significantly different morphology, perhaps similar to this observed under argon. A further backing of the claim comes from the sintering studies on Au or Ag surfaces that showed dendrite formation under CO_2RR.[117] These metals do not interact with CO after it is being produced and undergo only a PMC sintering, perhaps due to ligand loss under the reducing environment.

In the hope of better understanding the role of CO in the sintering process, sintered objects under "CO_2" and "no CO_2" conditions were investigated using high-resolution TEM (Figure 4.8). In both cases, the material is highly-crystalline, but the faceted structures described previously form large domains of single-crystal orientation, while the structures ascribed to PMC processes consist of several small domains oriented at random. These domains are smaller than the original Cu NCs diameter of 7nm which makes sense because these crystals are themselves made up of several crystalline domains.[72] These observations are further confirmed with selected-area electron diffraction (Figure 4.9). Large single-crystal domains correspond to a strong pattern, while smaller domains present much fainter spots that are not ordered in one line. Both the observed lattice

spacings and diffraction patterns are indicative of Cu_2O. The catalyst must have oxidized in the air after being removed from the catalytic conditions.
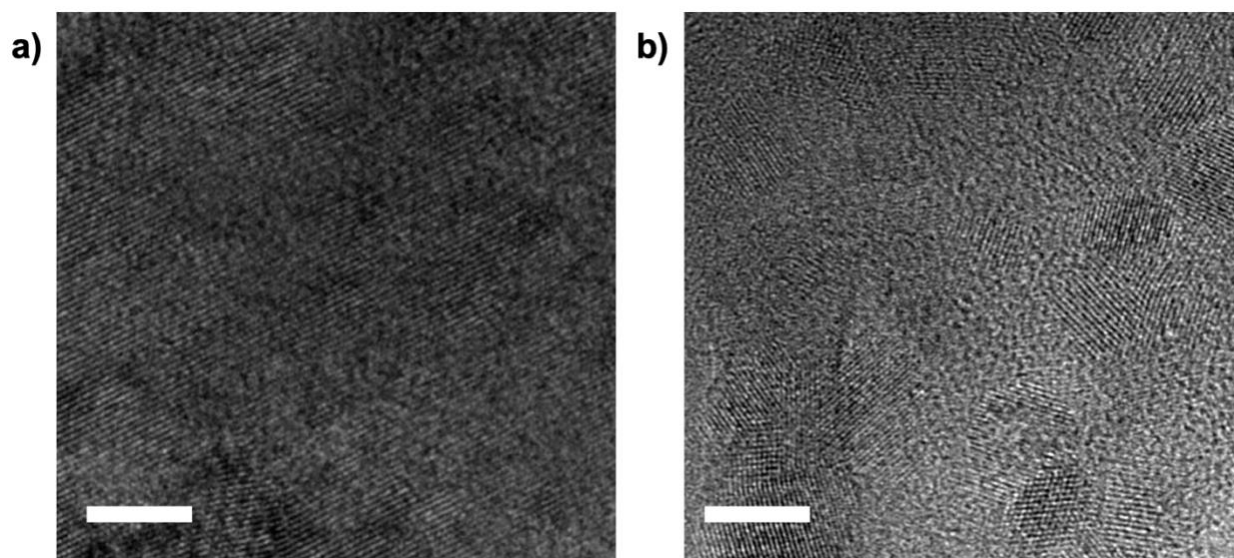
Figure 4.8. High-resolution TEM images of sintered objects
a) A center part of one of the large structures only seen under "CO_2" conditions b) A center part of a structure from "no CO_2" conditions. Scale bars correspond to 5nm.
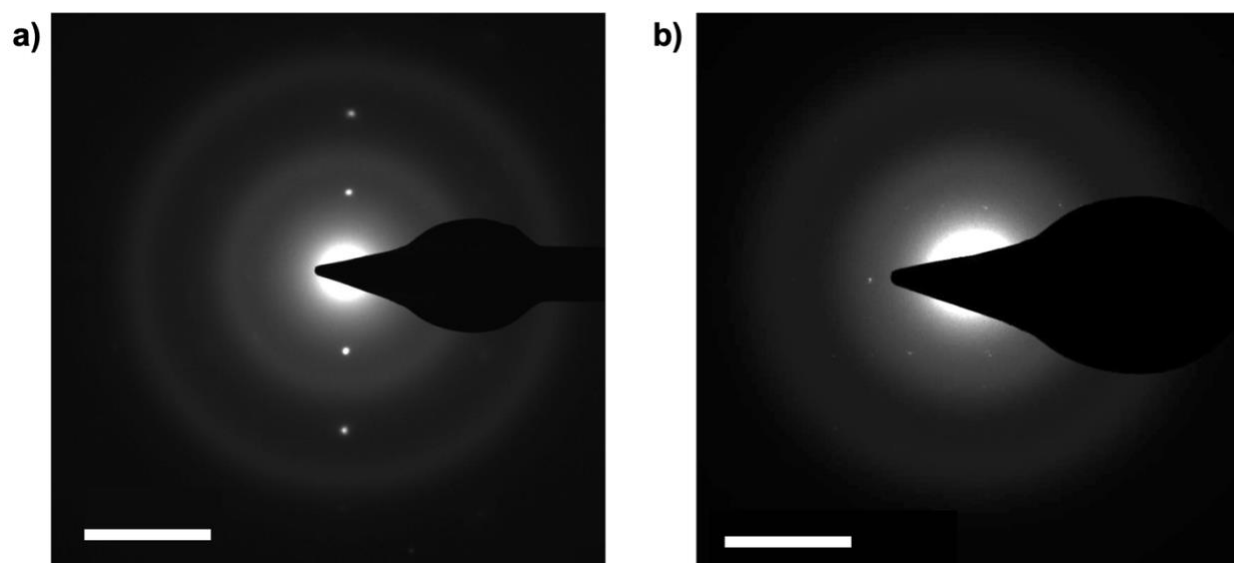
Figure 4.9. Selected area electron diffraction patterns.
a) "CO_2" conditions: strong diffraction pattern revealing a single crystal. b) "No CO_2 conditions": diffraction spots are much fainter and do not belong to a single crystal. Scale bars correspond to 5 nm^{-1}.

The electron diffraction data suggest the CO binding is responsible for a morphological restructuring of the Cu catalyst that cannot be only ascribed to a PMC process. The latter would leave the crystalline domains being ordered at random and would not create a single larger facet,

57

as it is the case with "no CO_2" experiments. When CO is present, some structures turn into single crystals, which is presumably caused by a change in surface energy or perhaps an increase in atom mobility that effectively "anneals" the surfaces. The question remains what determine the fraction of structures that undergo this process, as there are many other objects formed that remain in less ordered. Possibly, it is the matter of kinetics and given sufficiently long enough time, more energy, or a higher concentration of CO on the surface, all crystals would eventually undergo restructuring towards single crystals.

4.5 Electron beam effect on sintering

A promising technique of studying the sintering process is identical-location (IL) imaging, where the same surface region is imaged before and after catalysis.[121] Even with a uniform and monodisperse catalyst such as spherical nanocrystals, it is difficult to maintain exactly the same loading throughout the whole support, and it is not uncommon to observe variations between final morphologies in different areas of the electrode. IL imaging circumvents this issue and in principle gives more precise information, provided that the act of imaging does not perturb the investigated reaction.

IL-SEM imaging was attempted by marking spots on the electrode and imaging region before and after catalysis (Figure 4.10). Unfortunately, it is clear that the SEM electron beam interacts with nanoparticles strong enough that for magnifications required to see individual nanocrystals, the morphological change is no longer the same. The sintering of original nanocrystals appears to be stopped, perhaps by the electron beam cross-linking the ligands and anchoring the particles this way (Figure 4.11).
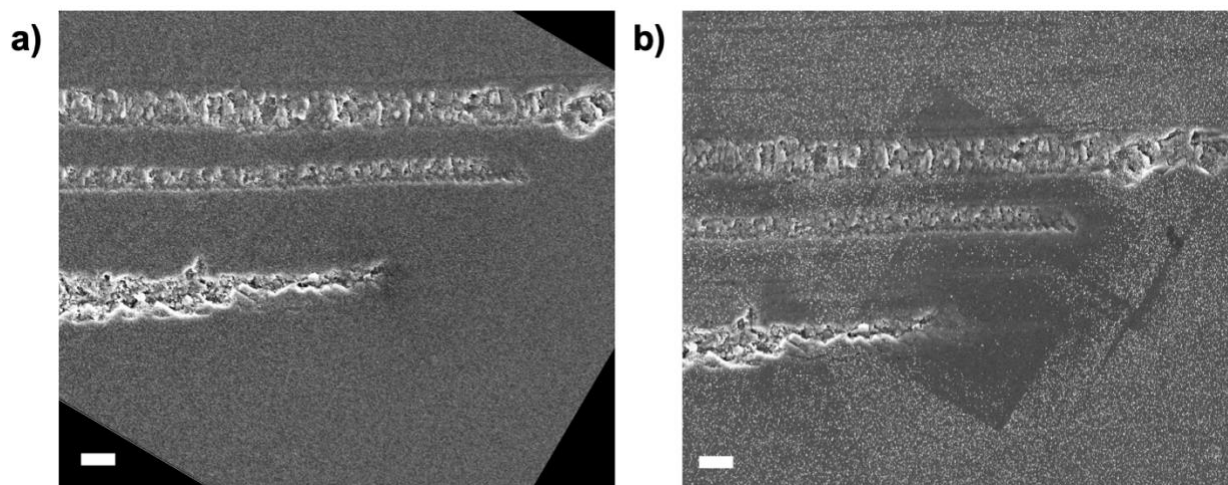
Figure 4.10. Identical location SEM imaging before and after catalysis
a) Electrode with spin-coated Cu nanocrystals before catalysis. Image rotated to present the same orientation of marks b) The same location on the electrode after catalysis (-1.05V vs. RHE for 20 min in CO_2). Scale bars correspond to 2 μm.
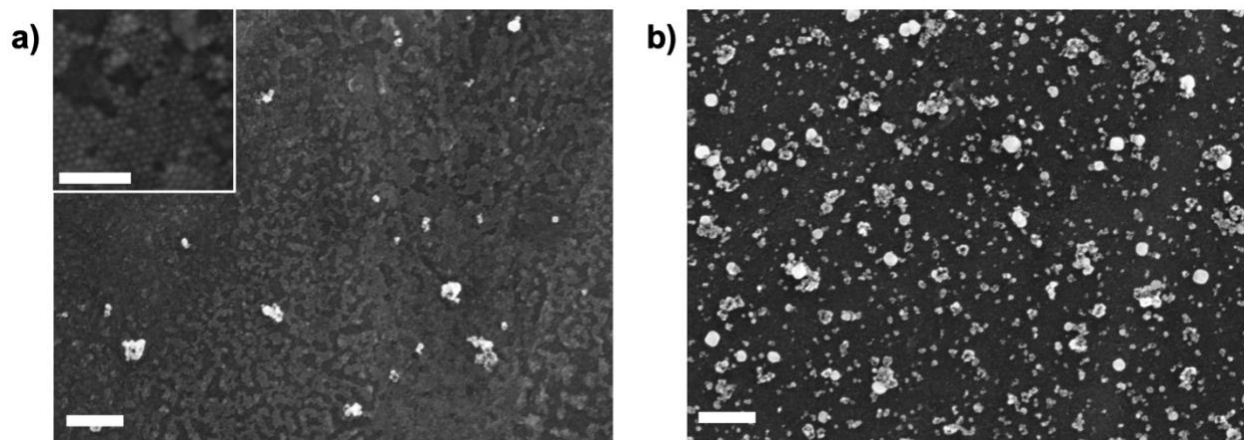
Figure 4.11. Electron beam effect on sintering

a) Region of the electrode imaged before catalysis with SEM. Inset: further magnification into this region displaying un-sintered particles (scale bar: 100 nm). b) Region of the electrode not imaged before catalysis – all particle sintered. Both scale bars correspond to 200 nm.

This experiment demonstrates that electron microscopy can perturb the investigated systems and it is crucial to perform control experiments to understand its effects. Since only extremely small fractions of the electrodes were imaged before catalysis, it could not have any effect on the catalytic runs. The effect was certainly caused by the electron beam and not, say, vacuum from the SEM chamber as other regions sintered normally, and we observed no macroscopic differences between electrodes exposed to vacuum and not before the electrolytic run. Furthermore, the dose of electrons provided during imaging, especially the current which increases with the magnification, can be used to control the amount of sintering to some extent (Figure 4.12).
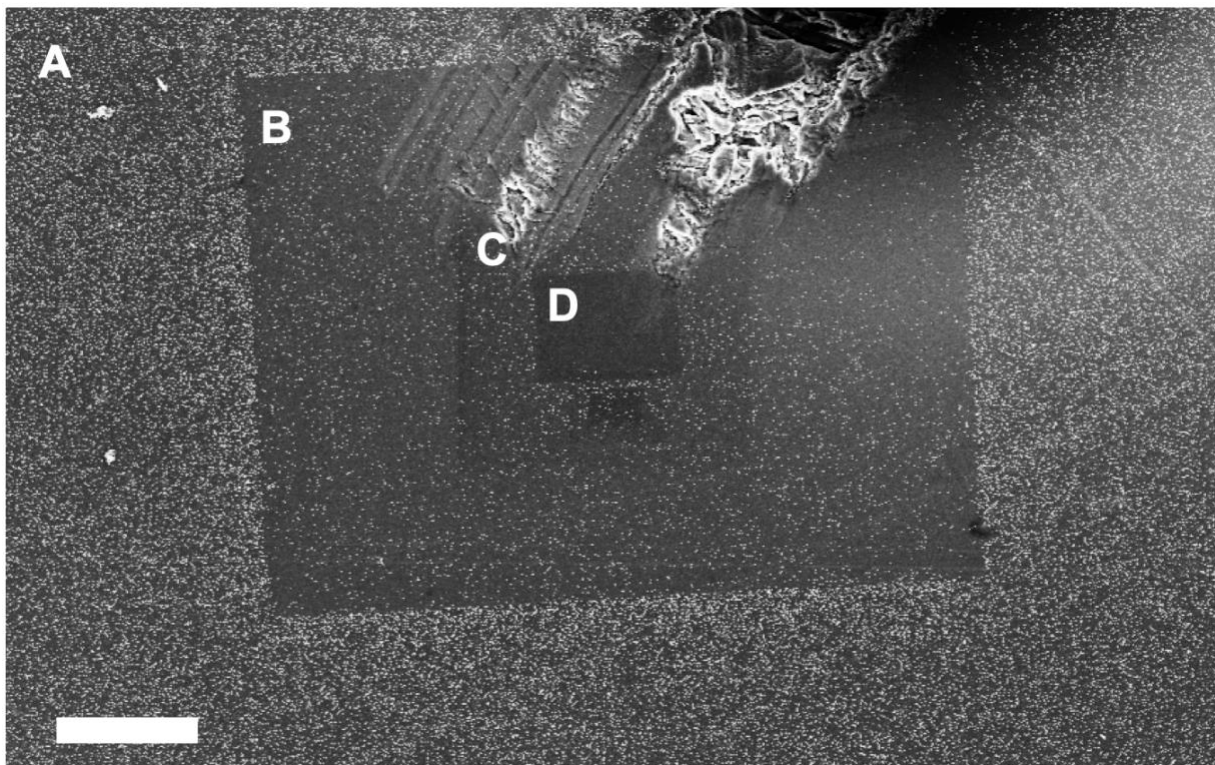
Figure 4.12. Controlled electron beam exposure before catalysis
Region A was not exposed to electron beam before catalysis, whereas regions B-D were, with an increasing electron dose and current. Region D was only exposed to 10 sec but highest magnification (50 kX), suggesting that current, i.e., dose per time, is more important for sintering control than the total dose. Scale bar corresponds to 10 μm.

The interaction of the electron beam with the surface of Cu nanocrystals is certainly complex as in some instances, the particles seem to have migrated out of the surface, leaving behind empty pores presumably formed from cross-linked ligands (Figure 4.13). Whether particles stay on the surface or not may perhaps be a factor of the exact received electron dose, ligand coverage, and catalytic conditions, but we chose not to probe the phenomenon in further detail as it is not the focus of our research. In theory, the electron beam could be used as a tool to prevent sintering, but particles covered in an organic layer are probably catalytically-inactive. In order to test this hypothesis, a substantially larger area of the electrode would have to be exposed to the electron beam, and since the effect occurs only at high magnifications (20kX+), it would take days in the SEM chamber which was unfeasible.
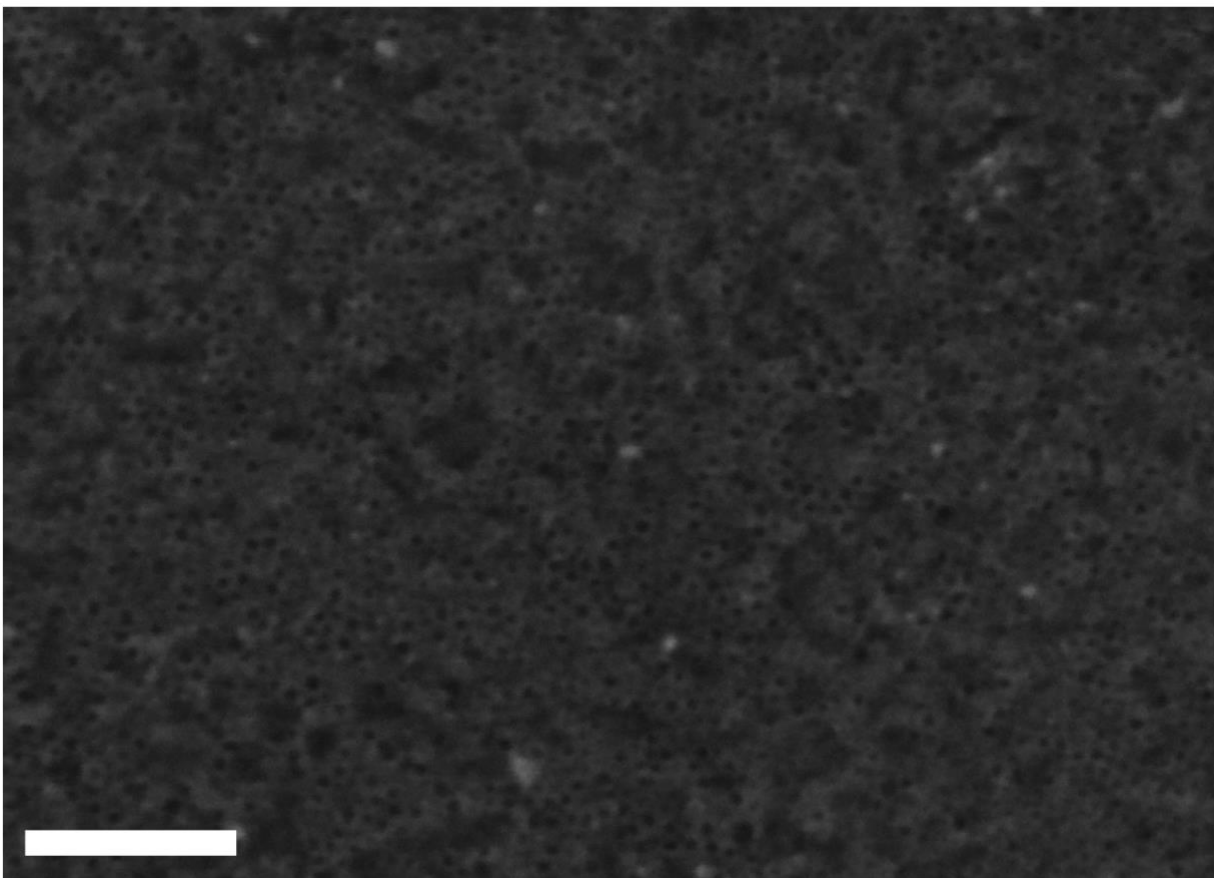
Figure 4.13. SEM image of electrode surface exposed to the electron beam before catalysis
The pores have approximately 6-7 nm in diameter, suggesting that they are templated by Cu nanoparticles. It is unclear what happened to the particles themselves but the material surrounded the pores is probably a result of ligand cross-linking by the electron beam. Scale bar corresponds to 100 nm. The effect was created by imaging the spot at 50kX magnification for 10 seconds before the catalysis.

Potentially, similar effects of ligand modification to prevent sintering could be reproduced with a different technique, such as gas plasma. The non-perturbating IL imaging is of more interest to this research projects and would require a non-electron imaging technique. Atomic force microscopy can be a potential solution. Finally, the effect described in this section is a good reminder that physical barriers, such as cross-linked ligands, can prevent sintering but it is crucial to keep access to the catalyst surface. Fully covered particles, while immune to sintering, will not display any catalytic activity either. Instead, porous nano-cages[99] or some other sophisticated solution may be a more promising solution.

4.6 Conclusion and future directions

While sintering occurring during electrochemical CO_2 reduction is not as widely studied as the matters of catalytic selectivity and efficiency, it remains a crucial component of the research because stability under operating conditions dictates the usefulness of a material to any real-life applications. In pursuit of more selective CO_2RR catalysts, scientists create more sophisticated

nano-engineered surfaces that are characterized by unusual structural motifs and highly uncoordinated sites, but these very structures are most likely to undergo morphological restructuring.

The first step to control the sintering, in our belief, is its understanding. Through control experiments involved bubbling argon instead of CO_2, it was demonstrated that the sintering occurs simply due to the reducing potential, perhaps due to ligand detachment that was documented with IRRAS and XPS, and is likely governed by a PMC mechanism as suggested previously.[114] However, CO_2 is not irrelevant for the sintering process, as without the molecule, there is no formation of larger, smooth and faceted Cu structures. Electron diffraction proves that such structures can be single-crystal which suggests that the binding of reaction intermediates, likely CO, changes the surface energy and increase atom mobility to "anneal" the crystals. We hope that these results will continue a broader discussion on the catalytic performance of tested materials that include the stability.

Future studies should involve the investigation of size distributions generated during the catalysis. In theory, PMC and AR processes have distinct kinetics and lead to significantly different particle size distributions (PSD).[122] The physics of AR has been described by Lifshitz–Slyozov–Wagner (LSW) theory which predicts a stationary PSD (i.e. whose shape won't change in time after reaching an equilibrium) with a long tail of particles smaller than the original size as well as a cut-off in the size distribution at a diameter smaller than the double of average diameter.[123] The size distribution for PMC is very different as it is skewed towards the tail of exceedingly larger particles and can be described by a log-normal distribution function.[124] In practice, it is often non-trivial to differentiate between the PSD of AR and PMC because the smallest particles that occur during ripening are unstable enough that they may coalesce and grow in a separate process. That being said, time-dependence studies should elucidate the sintering processes as well as describe more specifically on what time scale it is occurring.

Other factors worth exploring are the electric potential, size, and loading of the original nanocrystals, ligand nature and density, type of the support etc. Without a doubt, there are many variables available to change, which illustrates the complexity of the problem as well as the broad range of the possible outcomes. Clearly, this field will benefit from more theoretical frameworks just like creating fundamental concepts such as the scaling relationships of binding intermediates was crucial in improving the ability to think about the catalytic selectivity in CO_2 reduction. Simultaneously, we look forward to future efforts in sintering prevention, keeping in mind the critical need of keeping the surface accessible to binding intermediates.

4.7 Supplementary information
4.7.1 Used materials, synthesis, and electrochemical measurements

Materials
Copper(I) acetate (Sigma-Aldrich, 97%), n-Tetradecylphosphonic Acid (abbrev. as TDPA, Sigma-Aldrich, 97%), Trioctylamine (Sigma-Aldrich, 98%), Cesium Carbonate (Sigma-Aldrich, 99.995% trace metals basis), Carbon Dioxide (Praxair, 99.9% purity), Carbon Monoxide (Praxair, 99.99% purity), Argon (Praxair, 99.999% purity) Water (Milli-Q, 18.2 MΩ), Hexane (Sigma-

Aldrich, mixture of isomers, anhydrous, ≥99%), Ethanol (Sigma-Aldrich, pure, anhydrous, ≥99.5%), Isopropanol (Sigma-Aldrich, anhydrous, 99.5%).

Synthesis
Cu nanocrystals were synthesized by the same methods as described in Section 2.7.3.

Electrochemical measurements
Electrochemical measurements were performed with the same tools and methods as described in Section 3.5.2, except the nanoparticle loading which was optimized to a monolayer or less. This was achieved by spin-coating 80 µL of the nanocrystal solution, which was first deposited and then quickly spun at 1000 rpm for 50 sec. The film was then washed with 130 µL of ethanol, kept on the surface for 30 sec and then spun at 1000 rpm for 50 sec. Desired loading was optimized by analyzing SEM images and adjusting the concentration of the original nanocrystal solution (10-50mM). As ligand coverage was an important variable in the experiments, for the sake of reproducibility, all electrodes were prepared from a stock solution that underwent two centrifugation-resuspension cycles after the synthesis at 6500rpm for 5 min with ethanol:isopropanol (75:25 by volume) solution as the anti-solvent. Furthermore, glassy carbon disks were only polished with 1 µm alpha alumina (CH Instruments) and sonicated for 20 min in Milli-Q water to avoid any small alumina debris that could be faultily identified as Cu on SEM images.

All gases (CO_2, Ar, CO) were flowed at 5 sccm during chronoamperometry. For experiments with argon, the gas was passed through both chambers of the cell for 30 min before the application of voltage for pH equilibration. Since electrochemical runs passing CO and Ar displayed more current instability while applying -1.05V vs RHE than the CO_2 runs did, chronoamperometry was sometimes replaced with chronopotentiometry ensuring that the potential remained within the window of -1V and -1.1V vs RHE for most of the run. This change did not affect the observed morphologies.

4.7.2 Other characterization methods

All SEM experiments were performed using Zeiss Gemini Ultra-55 field emission SEM with an InLens detector, 5 kV accelerating voltage, and 3 mm working distance. For IL imaging, the surface of electrodes was scratched with a diamond scribe to mark the locations. Electron beam effect was probed by zooming in to the desired magnification (between 2kX and 100kX) and waiting for a desired amount of time (10 sec – 5 min).

For electron microscopy, material was transferred onto TEM grids using the techniques described in Section 3.5.3. Selected area electron diffraction was performed using a 200 kV Tecnai G2 T20 S-TWIN with a Gatan Rio 16 camera after ensuring that there is only one objects of interest in the aperture field of view. High-resolution TEM imaging was done using JEOL 2100-F 200 kV Field-Emission Analytical transmission electron microscope.

IRRAS spectra were recorded on a Bruker FT-IR spectrometer model Vertex 80 equipped with a LN2 cooled HgCdTe detector Kolmar model KMPV11-1-J2 with a 14 µm band gap or KMPV8-1-J2 with 8 µm bandgap, a computer-controlled reflection accessory Bruker model A513/QA, and

wire-grid polarizer model F350. The mirror angle of the IRRAS accessory was fixed at 70° and the grid polarizer switched between p and s polarization, and an aperture of 2.0 mm was used. Fifty spectra of 400 scans each at 2 cm^{-1} resolution were recorded and averaged. Sample single beam spectra with p polarization were divided by single beam spectra of reference sample (mirror) and the negative logarithm calculated. A corresponding absorbance spectrum for the s polarized configuration was computed and subtracted from the p polarized absorbance spectrum. From this result, a background was subtracted. Bands of residual atmospheric water vapor in the sample compartment were computationally eliminated as well.

XPS measurements were performed directly on the used electrodes using a Thermo Scientific K-Alpha Plus X-ray photoelectron spectrometer. The spectra were acquired with monochromatized Al Kα radiation and 400 μm beam size. Cu 2p and P 2p edges were quantified by fitting GL(30) peak shapes and using appropriate relative sensitivity factors.

References

(1)   Chu, S.; Cui, Y.; Liu, N. The Path towards Sustainable Energy. *Nat. Mater.* **2016**, *16*, 16–22.

(2)   Chorkendorff, I.; Dickens, C. F.; Seh, Z. W.; Kibsgaard, J.; Jaramillo, T. F.; Nørskov, J. K. Combining Theory and Experiment in Electrocatalysis: Insights into Materials Design. *Science* **2017**, *355*, eaad4998.

(3)   Arvia, A. J.; Bolzán, A. E.; Pasquale, M. A. Electrocatalysis: A Survey of Fundamental Concepts. In *Catalysis in Electrochemistry: From Fundamental Aspects to Strategies for Fuel Cell Development*; Santos, E., Schmickler, W., Eds.; The Wiley Series on Electrocatalysis and Electrochemistry; Wiley: Hoboken, NJ, USA, 2011; pp 17–66.

(4)   Bard, A. J.; Faulkner, L. R. *Electrochemical Methods: Fundamentals and Applications*, 2nd ed.; Wiley Textbooks, 2000.

(5)   Jiao, Y.; Zheng, Y.; Jaroniec, M.; Qiao, S. Z. Design of Electrocatalysts for Oxygen- and Hydrogen-Involving Energy Conversion Reactions. *Chem. Soc. Rev.* **2015**, *44*, 2060–2086.

(6)   van de Lagemaat, J.; Sargent, E. H.; Kelley, S. O.; Tao, L.; Bushuyev, O. S.; Dinh, C. T.; De Luna, P.; Saur, G. What Should We Make with CO2 and How Can We Make It? *Joule* **2018**, *2*, 825–832.

(7)   Kuhl, K. P.; Cave, E. R.; Abram, D. N.; Jaramillo, T. F. New Insights into the Electrochemical Reduction of Carbon Dioxide on Metallic Copper Surfaces. *Energy Environ. Sci.* **2012**, *5*, 7050.

(8)   Ma, S.; Sadakiyo, M.; Luo, R.; Heima, M.; Yamauchi, M.; Kenis, P. J. A. One-Step Electrosynthesis of Ethylene and Ethanol from CO2 in an Alkaline Electrolyzer. *J. Power Sources* **2016**, *301*, 219–228.

(9)   Singh, M. R.; Clark, E. L.; Bell, A. T. Effects of Electrolyte, Catalyst, and Membrane Composition and Operating Conditions on the Performance of Solar-Driven Electrochemical Reduction of Carbon Dioxide. *Phys. Chem. Chem. Phys.* **2015**, *17*, 18924–18936.

(10)   Hori, Y. Electrochemical CO2 Reduction on Metal Electrodes. *Mod. Asp. Electrochem.* **2008**, No. 42, 89–189.

(11)   Peterson, A.; Nørskov, J. Activity Descriptors for CO2 Electroreduction to Methane on Transition-Metal Catalysts. *J. Phys. Chem. Lett.* **2012**, *3*, 251–258.

(12) Montoya, J. H.; Shi, C.; Chan, K.; Nørskov, J. K. Theoretical Insights into a CO Dimerization Mechanism in CO2 Electroreduction. *J. Phys. Chem. Lett.* **2015**, *6*, 2032–2037.

(13) Kuhl, K. P.; Hatsukade, T.; Cave, E. R.; Abram, D. N.; Kibsgaard, J.; Jaramillo, T. F. Electrocatalytic Conversion of Carbon Dioxide to Methane and Methanol on Transition Metal Surfaces. *J. Am. Chem. Soc.* **2014**, *136*, 14107–14113.

(14) Rühle, S. Tabulated Values of the Shockley-Queisser Limit for Single Junction Solar Cells. *Sol. Energy* **2016**, *130*, 139–147.

(15) Zu, C.-X.; Li, H. Thermodynamic Analysis on Energy Densities of Batteries. *Energy Environ. Sci.* **2011**, *4*, 2614.

(16) Peterson, A. a.; Abild-Pedersen, F.; Studt, F.; Rossmeisl, J.; Nørskov, J. K. How Copper Catalyzes the Electroreduction of Carbon Dioxide into Hydrocarbon Fuels. *Energy Environ. Sci.* **2010**, *3*, 1311.

(17) Gurudayal; Bullock, J.; Srankó, D. F.; Towle, C. M.; Lum, Y.; Hettick, M.; Scott, M. C.; Javey, A.; Ager, J. Efficient Solar-Driven Electrochemical CO2 Reduction to Hydrocarbons and Oxygenates. *Energy Environ. Sci.* **2017**, *10*, 2222–2230.

(18) Li, Y.; Sun, Q. Recent Advances in Breaking Scaling Relations for Effective Electrochemical Conversion of CO2. *Adv. Energy Mater.* **2016**, *6*, 1600463.

(19) Shi, C.; Hansen, H. A.; Lausche, A. C.; Nørskov, J. K. Trends in Electrochemical CO2 Reduction Activity for Open and Close-Packed Metal Surfaces. *Phys. Chem. Chem. Phys.* **2014**, *16*, 4720–4727.

(20) Nørskov, J. K.; Rossmeisl, J.; Logadottir, A.; Lindqvist, L.; Kitchin, J. R.; Bligaard, T.; Jónsson, H. Origin of the Overpotential for Oxygen Reduction at a Fuel-Cell Cathode. *J. Phys. Chem. B* **2004**, *108*, 17886–17892.

(21) Montoya, J. H.; Peterson, A. A.; Nørskov, J. K. Insights into C-C Coupling in CO2 Electroreduction on Copper Electrodes. *ChemCatChem* **2013**, *5*, 737–742.

(22) Abild-Pedersen, F.; Greeley, J.; Studt, F.; Rossmeisl, J.; Munter, T. R.; Moses, P. G.; Skúlason, E.; Bligaard, T.; N\orskov, J. K. Scaling Properties of Adsorption Energies for Hydrogen-Containing Molecules on Transition-Metal Surfaces. *Phys. Rev. Lett.* **2007**, *99*, 16105.

(23) Calle-Vallejo, F.; Tymoczko, J.; Colic, V.; Vu, Q. H.; Pohl, M. D.; Morgenstern, K.; Loffreda, D.; Sautet, P.; Schuhmann, W.; Bandarenka, A. S. Finding Optimal Surface Sites on Heterogeneous Catalysts by Counting Nearest Neighbors. *Science* **2015**, *350*, 185–189.

(24) Cargnello, M. Colloidal Nanocrystals as Building Blocks for Well-Defined Heterogeneous Catalysts. *Chem. Mater.* **2019**, *31*, 576–596.

(25) Somorjai, G. A.; Li, Y. Impact of Surface Chemistry. *Proc. Natl. Acad. Sci.* **2011**, *108*, 917–924.

(26) Hu, L.; Peng, Q.; Li, Y. Selective Synthesis of Co3O4 Nanocrystal with Different Shape and Crystal Plane Effect on Catalytic Property for Methane Combustion. *J. Am. Chem. Soc.* **2008**, *130*, 16136–16137.

(27) Rodriguez, J. A. Physical and Chemical Properties of Bimetallic Surfaces. *Surf. Sci. Rep.* **1996**, *24*, 225–287.

(28) Wang, D.; Li, Y. Bimetallic Nanocrystals : Liquid-Phase Synthesis and Catalytic Applications. *Adv. Mater.* **2011**, *23*, 1044–1060.

(29) Montoya, J. H.; Seitz, L. C.; Chakthranont, P.; Vojvodic, A.; Jaramillo, T. F.; Nørskov, J. K. Materials for Solar Fuels and Chemicals. *Nat. Mater.* **2016**, *16*, 70–81.

(30)   Moulijn, J. A.; Van Diepen, A. E.; Kapteijn, F. Catalyst Deactivation: Is It Predictable? What to Do? *Appl. Catal. A Gen.* **2001**, *212*, 3–16.

(31)   Behafarid, F.; Roldan Cuenya, B. Towards the Understanding of Sintering Phenomena at the Nanoscale: Geometric and Environmental Effects. *Top. Catal.* **2013**, *56*, 1542–1559.

(32)   Goodman, E. D.; Schwalbe, J. A.; Cargnello, M. Mechanistic Understanding and the Rational Design of Sinter-Resistant Heterogeneous Catalysts. *ACS Catal.* **2017**, *7*, 7156–7173.

(33)   Hansen, T. W.; Delariva, A. T.; Challa, S. R.; Datye, A. K. Sintering of Catalytic Nanoparticles: Particle Migration or Ostwald Ripening? *Acc. Chem. Res.* **2013**, *46*, 1720–1730.

(34)   Inzelt, G. Crossing the Bridge between Thermodynamics and Electrochemistry. From the Potential of the Cell Reaction to the Electrode Potential. *ChemTexts* **2014**, *1*, 2.

(35)   Ahluwalia, R. K.; Arisetty, S.; Peng, J.-K.; Subbaraman, R.; Wang, X.; Kariuki, N.; Myers, D. J.; Mukundan, R.; Borup, R.; Polevaya, O. Dynamics of Particle Growth and Electrochemical Surface Area Loss Due to Platinum Dissolution. *J. Electrochem. Soc.* **2014**, *161*, F291–F304.

(36)   Ferreira, P. J.; la O', G. J.; Shao-Horn, Y.; Morgan, D.; Makharia, R.; Kocha, S.; Gasteiger, H. A. Instability of Pt∕C Electrocatalysts in Proton Exchange Membrane Fuel Cells. *J. Electrochem. Soc.* **2005**, *152*, A2256.

(37)   Tanaka, K. Chemical Reconstruction and Catalysis of Metal and Bimetallic Surfaces. *Surf. Sci.* **1996**, *357–358*, 721–728.

(38)   Thomas, L.; Ruban, A. V.; Skriver, H. L.; Kollár, J.; Clausen, B. S.; Topsøe, H.; Hansen, P. L. Atom-Resolved Imaging of Dynamic Shape Changes in Supported Copper Nanocrystals. *Science* **2002**, *295*, 2053–2055.

(39)   Eren, B.; Zherebetskyy, D.; Patera, L. L.; Wu, C. H.; Bluhm, H.; Africh, C.; Wang, L.-W.; Somorjai, G. A.; Salmeron, M. Activation of Cu(111) Surface by Decomposition into Nanoclusters Driven by CO Adsorption. *Science* **2016**, *351*, 475–478.

(40)   Manthiram, K.; Beberwyck, B. J.; Alivisatos, A. P. Enhanced Electrochemical Methanation of Carbon Dioxide with a Dispersible Nanoscale Copper Catalyst. *J. Am. Chem. Soc.* **2014**, *136*, 13319–13325.

(41)   Loiudice, A.; Lobaccaro, P.; Kamali, E. A.; Thao, T.; Huang, B. H.; Ager, J. W.; Buonsanti, R. Tailoring Copper Nanocrystals towards C2 Products in Electrochemical CO2 Reduction. *Angew. Chemie Int. Ed.* **2016**, *55*, 1–5.

(42)   Kim, D.; Kley, C. S.; Li, Y.; Yang, P. Copper Nanoparticle Ensembles for Selective Electroreduction of CO2 to C2 –C 3 Products. *Proc. Natl. Acad. Sci.* **2017**, *114*, 10560–10565.

(43)   Vasileff, A.; Xu, C.; Jiao, Y.; Zheng, Y.; Qiao, S. Z. Surface and Interface Engineering in Copper-Based Bimetallic Materials for Selective CO2 Electroreduction. *Chem* **2018**, *4*, 1809–1831.

(44)   Watanabe, M.; Shibata, M.; Kato, A. Design of Alloy Electrocatalysts for CO2 Reduction. *J. Electrochem. Soc.* **1991**, *138*, 3382–3389.

(45)   Clark, E. L.; Hahn, C.; Jaramillo, T. F.; Bell, A. T. Electrochemical CO2Reduction over Compressively Strained CuAg Surface Alloys with Enhanced Multi-Carbon Oxygenate Selectivity. *J. Am. Chem. Soc.* **2017**, *139*, 15848–15857.

(46)   Hoang, T. T. H.; Verma, S.; Ma, S.; Fister, T. T.; Timoshenko, J.; Frenkel, A. I.; Kenis, P. J. A.; Gewirth, A. A. Nanoporous Copper-Silver Alloys by Additive-Controlled

Electrodeposition for the Selective Electroreduction of CO2 to Ethylene and Ethanol. *J. Am. Chem. Soc.* **2018**, *140*, 5791–5797.

(47) Lum, Y.; Ager, J. W. Sequential Catalysis Controls Selectivity in Electrochemical CO2 Reduction on Cu. *Energy Environ. Sci.* **2018**, *11*, 2935–2944.

(48) Morales-Guio, C. G.; Cave, E. R.; Nitopi, S. A.; Feaster, J. T.; Wang, L.; Kuhl, K. P.; Jackson, A.; Johnson, N. C.; Abram, D. N.; Hatsukade, T.; et al. Improved CO2 Reduction Activity towards C2+ Alcohols on a Tandem Gold on Copper Electrocatalyst. *Nat. Catal.* **2018**, *1*, 764–771.

(49) De Luna, P.; Xie, H.; Liang, Z.; Wang, Z.; Sham, T.-K.; Bals, S.; Zou, C.; Bladt, E.; Hofkens, J.; Sinton, D.; et al. Dopant-Induced Electron Localization Drives CO2 Reduction to C2 Hydrocarbons. *Nat. Chem.* **2018**, *10*, 974–980.

(50) Ferrando, R.; Jellinek, J.; Johnston, R. L. Nanoalloys: From Theory to Applications of Alloy Clusters and Nanoparticles. *Chem. Rev.* **2008**, *108*, 845–910.

(51) Chaudhuri, R. G.; Paria, S. Core/Shell Nanoparticles: Classes, Properties, Synthesis Mechanisms, Characterization, and Applications. *Chem. Rev.* **2012**, *112*, 2373–2433.

(52) Pettifor, D. G.; Cottrell, A. H. *Electron Theory in Alloy Design*; Institute of Materials: London, 1992.

(53) Miedema, A. R.; de Boer, F. R.; Boom, R. Model Predictions for the Enthalpy of Formation of Transition Metal Alloys. *Calphad* **1977**, *1*, 341–359.

(54) Marks, L. D.; Peng, L. Nanoparticle Shape, Thermodynamics and Kinetics. *J. Phys. Condens. Matter* **2016**, *28*, 053001.

(55) Peng, H.; Qi, W.; Li, S.; Ji, W. Modeling the Phase Stability of Janus, Core-Shell, and Alloyed Ag-Cu and Ag-Au Nanoparticles. *J. Phys. Chem. C* **2015**, *119*, 2186–2195.

(56) Ozolins, V.; Wolverton, C.; Zunger, A. Cu-Au, Ag-Au, Cu-Ag, and Ni-Au Intermetallics: First-Principles Study of Temperature-Composition Phase Diagrams and Structures. *Phys. Rev. B* **1998**, *57*, 6427–6443.

(57) Wu, W.; Lei, M.; Yang, S.; Zhou, L.; Liu, L.; Xiao, X.; Jiang, C.; Roy, V. A. L. A One-Pot Route to the Synthesis of Alloyed Cu / Ag Bimetallic Nanoparticles with Different Mass Ratios for Catalytic Reduction of 4-Nitrophenol. *J. Mater. Chem. A* **2015**, *3*, 3450–3455.

(58) Shin, K.; Kim, H.; Mo, H. Catalytic Characteristics of AgCu Bimetallic Nanoparticles in the Oxygen Reduction Reaction. *ChemSusChem* **2013**, *6*, 1044–1049.

(59) Lee, C.; Kim, N. R.; Koo, J.; Lee, Y. J.; Lee, H. M. Cu-Ag Core-Shell Nanoparticles with Enhanced Oxidation Stability for Printed Electronics. *Nanotechnology* **2015**, *26*, 455601.

(60) Chatain, D.; Wynblatt, P.; Hagege, S.; Siem, E. J.; Carter, W. C. Wetting in Multiphase Systems with Complex Geometries. *Interface Sci.* **2001**, *9*, 191–197.

(61) Howe, J. M.; Mebed, A. M.; Chatterjee, K.; Li, P.; Murayama, M.; Johnson, W. C. Effect of Phase Fraction on the Tri-Junction in Two-Phase Nanoparticle Systems. *Acta Mater.* **2003**, *51*, 1359–1372.

(62) Yuan, C. W.; Shin, S. J.; Liao, C. Y.; Guzman, J.; Stone, P. R.; Watanabe, M.; Ager, J. W.; Haller, E. E.; Chrzan, D. C. Structure Map for Embedded Binary Alloy Nanocrystals. *Appl. Phys. Lett.* **2008**, *93*, 4–6.

(63) Johnson, K. L.; Kendall, K.; Roberts, A. D. Surface Energy and the Contact of Elastic Solids. *Proc. R. Soc. Lond. A.* **1971**, *324*, 301–313.

(64) Cahn, J. W.; Hilliard, J. E. Free Energy of a Nonuniform System. I. Interfacial Free Energy. *J. Chem. Phys.* **1958**, *28*, 258–267.

(65) Pellarin, M.; Issa, I.; Langlois, C.; Lebeault, M.-A.; Ramade, J.; Lermé, J.; Broyer, M.;

Cottancin, E. Plasmon Spectroscopy and Chemical Structure of Small Bimetallic Cu (1− x) Ag x Clusters. *J. Phys. Chem. C* **2015**, *119*, 5002–5012.

(66) Chen, Z.; Mochizuki, D.; Maitani, M. M.; Wada, Y. Facile Synthesis of Bimetallic Cu–Ag Nanoparticles under Microwave Irradiation and Their Oxidation Resistance. *Nanotechnology* **2013**, *24*, 265602.

(67) Tsuji, M.; Hikino, S.; Sano, Y.; Horigome, M. Preparation of Cu@Ag Core–Shell Nanoparticles Using a Two-Step Polyol Process under Bubbling of N2 Gas. *Chem. Lett.* **2009**, *38*, 518–519.

(68) Muzikansky, A.; Nanikashvili, P.; Grinblat, J.; Zitoun, D. Ag Dewetting in Cu@Ag Monodisperse Core−Shell Nanoparticles. *J. Phys. Chem. C.* **2013**, *117*, 3093–3100.

(69) Kim, N. R.; Shin, K.; Jung, I.; Shim, M.; Lee, H. M. Ag − Cu Bimetallic Nanoparticles with Enhanced Resistance to Oxidation : A Combined Experimental and Theoretical Study. *J. Phys. Chem. C.* **2014**, *118*, 26324–26311.

(70) Wadell, C.; Yasuhara, A.; Sannomiya, T. Asymmetric Light Absorption and Radiation of Ag–Cu Hybrid Nanoparticles. *J. Phys. Chem. C.* **2017**, *121*, 27029–27035.

(71) Anderson, B. D.; Tracy, J. B. Nanoparticle Conversion Chemistry: Kirkendall Effect, Galvanic Exchange, and Anion Exchange. *Nanoscale* **2014**, *6*, 12195–12216.

(72) Hung, L. L.; Tsung, C. K.; Huang, W.; Yang, P. Room-Temperature Formation of Hollow Cu2O Nanoparticles. *Adv. Mater.* **2010**, *22*, 1910–1914.

(73) Szłyk, E.; Piszczek, P.; Chaberski, M.; Goliński, A. Studies of Thermal Decomposition Process of Ag(I) Perfluorinated Carboxylates with Temperature Variable IR and MS. *Polyhedron* **2001**, *20*, 2853–2861.

(74) Madras, G.; McCoy, B. J. Temperature Effects on the Transition from Nucleation and Growth to Ostwald Ripening. *Chem. Eng. Sci.* **2004**, *59*, 2753–2765.

(75) Yin, M.; Wu, C.-K.; Lou, Y.; Burda, C.; Koberstein, J. T.; Zhu, Y.; O'Brien, S. Copper Oxide Nanocrystals. *J. Am. Chem. Soc.* **2005**, *127*, 9506–9511.

(76) Chee, S.; Lee, J. Preparation and Oxidation Behavior of Ag-Coated Cu Nanoparticles Less than 20 Nm in Size. *J. Mater. Chem. C* **2014**, *2*, 5372–5381.

(77) Soon, A.; Söhnel, T.; Idriss, H. Plane-Wave Pseudopotential Density Functional Theory Periodic Slab Calculations of CO Adsorption on Cu2O(1 1 1) Surface. *Surf. Sci.* **2005**, *579*, 131–140.

(78) Skriver, H. L.; Rosengaard, N. M. Surface Energy and Work Function of Elemental Metals. *Phys. Rev. B* **1992**, *46*, 7157–7168.

(79) Biesinger, M. C.; Lau, L. W. M.; Gerson, A. R.; Smart, R. S. C. Resolving Surface Chemical States in XPS Analysis of First Row Transition Metals, Oxides and Hydroxides: Sc, Ti, V, Cu and Zn. *Appl. Surf. Sci.* **2010**, *257*, 887–898.

(80) Gilbert, J. B.; Rubner, M. F.; Cohen, R. E. Depth-Profiling X-Ray Photoelectron Spectroscopy (XPS) Analysis of Interlayer Diffusion in Polyelectrolyte Multilayers. *Proc. Natl. Acad. Sci.* **2013**, *110*, 6651–6656.

(81) Cai, W.; Zhong, H.; Zhang, L. Optical Measurements of Oxidation Behavior of Silver Nanometer Particle within Pores of Silica Host. *J. Appl. Phys.* **1998**, *83*, 1705–1710.

(82) Pauly, N.; Yubero, F.; Tougaard, S. Quantitative Analysis of Satellite Structures in XPS Spectra of Gold and Silver. *Appl. Surf. Sci.* **2016**, *383*, 317–323.

(83) Besenbacher, F.; Nørskov, J. K. Oxygen Chemisorption on Metal Surfaces: General Trends for Cu, Ni and Ag. *Prog. Surf. Sci.* **1993**, *44*, 5–66.

(84) Cui, F.; Yu, Y.; Dou, L.; Sun, J.; Yang, Q.; Schildknecht, C.; Schierle-Arndt, K.; Yang, P.

Synthesis of Ultrathin Copper Nanowires Using Tris(Trimethylsilyl)Silane for High-Performance and Low-Haze Transparent Conductors. *Nano Lett.* **2015**, *15*, 7610–7615.

(85) Kang, Y.; Ye, X.; Murray, C. B. Size- and Shape-Selective Synthesis of Metal Nanocrystals and Nanowires Using CO as a Reducing Agent. *Angew. Chemie - Int. Ed.* **2010**, *49*, 6156–6159.

(86) Delogu, F. Free Energy Differences between Ag-Cu Nanophases with Different Chemical Order. *J. Phys. Chem. C* **2010**, *114*, 19946–19951.

(87) Linic, S.; Christopher, P.; Ingram, D. B. Plasmonic-Metal Nanostructures for Efficient Conversion of Solar to Chemical Energy. *Nat. Mater.* **2011**, *10*, 911–921.

(88) Lin, X. Z.; Teng, X.; Yang, H. Direct Synthesis of Narrowly Dispersed Silver Nanoparticles Using a Single-Source Precursor. *Langmuir* **2003**, *19*, 10081–10085.

(89) Rice, K. P.; Walker, E. J.; Stoykovich, M. P.; Saunders, A. E. Solvent-Dependent Surface Plasmon Response and Oxidation of Copper Nanocrystals. *J. Phys. Chem. C* **2011**, *115*, 1793–1799.

(90) Borgohain, K.; Murase, N.; Mahamuni, S. Synthesis and Properties of Cu2O Quantum Particles. *J. Appl. Phys.* **2002**, *92*, 1292–1297.

(91) Tao, A. R.; Habas, S.; Yang, P. Shape Control of Colloidal Metal Nanocrystals. *Small* **2008**, *4*, 310–325.

(92) Yang, C. C.; Mai, Y. W. Size, Dimensionality, and Constituent Stoichiometry Dependence of Physicochemical Properties in Nanosized Binary Alloys. *J. Phys. Chem. C.* **2013**, *117*, 2421–2426.

(93) Xiong, S.; Qi, W.; Cheng, Y.; Huang, B.; Wang, M.; Li, Y. Modeling Size Effects on the Surface Free Energy of Metallic Nanoparticles and Nanocavities. *Phys. Chem. Chem. Phys.* **2011**, *13*, 10648–10651.

(94) Qi, W. Nanoscopic Thermodynamics. *Acc. Chem. Res.* **2016**, *49*, 1587–1595.

(95) Chandross, M. Energetics of the Formation of Cu-Ag Core-Shell Nanoparticles. *Model. Simul. Mater. Sci. Eng.* **2014**, *22*, 075012.

(96) Puzder, A.; Williamson, A. J.; Zaitseva, N.; Galli, G.; Manna, L.; Alivisatos, A. P. The Effect of Organic Ligand Binding on the Growth of CdSe Nanoparticles Probed by Ab Initio Calculations. *Nano Lett.* **2004**, *4*, 2361–2365.

(97) Jing, H.; Large, N.; Zhang, Q.; Wang, H. Epitaxial Growth of Cu 2 O on Ag Allows for Fine Control Over Particle Geometries and Optical Properties of Ag–Cu 2 O Core–Shell Nanoparticles. *J. Phys. Chem. C* **2014**, *118*, 19948–19963.

(98) Huang, J.; Mensi, M.; Mantella, V.; Oveisi, E.; Buonsanti, R. Structural Sensitivities in Bimetallic Catalysts for Electrochemical CO2 Reduction Revealed by Ag–Cu Nanodimers. *J. Am. Chem. Soc.* **2019**, *141*, 2490–2499.

(99) Knossalla, J.; Paciok, P.; Göhl, D.; Jalalpoor, D.; Pizzutilo, E.; Mingers, A. M.; Heggen, M.; Dunin-Borkowski, R. E.; Mayrhofer, K. J. J.; Schüth, F.; et al. Shape-Controlled Nanoparticles in Pore-Confined Space. *J. Am. Chem. Soc.* **2018**, *140*, 15684–15689.

(100) Nørskov, J. K.; Bligaard, T.; Logadottir, A.; Kitchin, J. R.; Chen, J. G.; Pandelov, S.; Stimming, U. Trends in the Exchange Current for Hydrogen Evolution. *J. Electrochem. Soc.* **2005**, *152*, J23–J26.

(101) Goodpaster, J. D.; Bell, A. T.; Head-Gordon, M. Identification of Possible Pathways for C-C Bond Formation during Electrochemical Reduction of CO2: New Theoretical Insights from an Improved Electrochemical Model. *J. Phys. Chem. Lett.* **2016**, *7*, 1471–1477.

(102) Mavrikakis, M.; Hammer, B.; Norskov, J. K. Effect of Strain on the Reactivity of Metal

Surfaces. *Phys. Rev. Lett.* **1998**, *81*, 2819–2822.

(103) Jung, S.; McCrory, C. C. L.; Ferrer, I. M.; Peters, J. C.; Jaramillo, T. F. Benchmarking Nanoparticulate Metal Oxide Electrocatalysts for the Alkaline Water Oxidation Reaction. *J. Mater. Chem. A* **2016**, *4*, 3068–3076.

(104) Zhang, J.; Li, Z.; Fu, Q.; Xue, Y.; Cui, Z. The Size-Dependence of Electrochemical Thermodynamics of Metal Nanoparticles Electrodes in Theory and Experiment. *J. Electrochem. Soc.* **2017**, *164*, H828–H835.

(105) Sprunger, P.; Lægsgaard, E.; Besenbacher, F. Growth of Ag on Cu(100) Studied by STM: From Surface Alloying to Ag Superstructures. *Phys. Rev. B - Condens. Matter Mater. Phys.* **1996**, *54*, 8163–8171.

(106) Osowiecki, W. T.; Ye, X.; Satish, P.; Bustillo, K. C.; Clark, E. L.; Alivisatos, A. P. Tailoring Morphology of Cu-Ag Nanocrescents and Core-Shell Nanocrystals Guided by a Thermodynamic Model. *J. Am. Chem. Soc.* **2018**, *140*, 8569–8577.

(107) Hayden, B. E. Particle Size and Support Effects. *Acc. Chem. Res.* **2013**, *46*, 1858–1866.

(108) Wei, J.; Schaeffer, N.; Pileni, M. P. Ag Nanocrystals: 1. Effect of Ligands on Plasmonic Properties. *J. Phys. Chem. B* **2014**, *118*, 14070–14075.

(109) Lobaccaro, P.; Singh, M. R.; Clark, E. L.; Kwon, Y.; Bell, A. T.; Ager, J. W. Effects of Temperature and Gas-Liquid Mass Transfer on the Operation of Small Electrochemical Cells for the Quantitative Evaluation of CO2 Reduction Electrocatalysts. *Phys. Chem. Chem. Phys.* **2016**, *18*, 26777–26785.

(110) Lin, J.; Bell, A. T.; Resasco, J.; Jaramillo, T. F.; Clark, E. L.; Chung, L.-T.; Landers, A.; Hahn, C.; Walton, A. Standards and Protocols for Data Acquisition and Reporting for Studies of the Electrochemical Reduction of Carbon Dioxide. *ACS Catal.* **2018**, *8*, 6560–6570.

(111) Resasco, J.; Chen, L. D.; Clark, E.; Tsai, C.; Hahn, C.; Jaramillo, T. F.; Chan, K.; Bell, A. T. Promoter Effects of Alkali Metal Cations on the Electrochemical Reduction of Carbon Dioxide. *J. Am. Chem. Soc.* **2017**, *139*, 11277–11287.

(112) Hwang, T. L.; Shaka, A. J. Water Suppression That Works. Excitation Sculpting Using Arbitrary Wave-Forms and Pulsed-Field Gradients. *J. Magn. Reson. Ser. A* **1995**, *112*, 275–279.

(113) Grosse, P.; Gao, D.; Scholten, F.; Sinev, I.; Mistry, H.; Roldan Cuenya, B. Dynamic Changes in the Structure, Chemical State and Catalytic Selectivity of Cu Nanocubes during CO2 Electroreduction: Size and Support Effects. *Angew. Chemie - Int. Ed.* **2018**, *57*, 6192–6197.

(114) Huang, J.; Hörmann, N.; Oveisi, E.; Loiudice, A.; De Gregorio, G. L.; Andreussi, O.; Marzari, N.; Buonsanti, R. Potential-Induced Nanoclustering of Metallic Catalysts during Electrochemical CO2 Reduction. *Nat. Commun.* **2018**, *9*, 1–9.

(115) Ph.Buffat; J-P.Borel. Size Effect on the Melting Temperature of Gold Particles. *Phys. Rev. A* **1976**, *13*, 2287–2298.

(116) Ouyang, R.; Liu, J. X.; Li, W. X. Atomistic Theory of Ostwald Ripening and Disintegration of Supported Metal Particles under Reaction Conditions. *J. Am. Chem. Soc.* **2013**, *135*, 1760–1771.

(117) Manthiram, K.; Surendranath, Y.; Alivisatos, A. P. Dendritic Assembly of Gold Nanoparticles during Fuel-Forming Electrocatalysis. *J. Am. Chem. Soc.* **2014**, *136*, 7237–7240.

(118) Beverskog, B.; Puigdomenech, I. Revised Pourbaix Diagrams for Copper at 25 to 300°C. *J.*

Electrochem. Soc. **1997**, *144*, 3476–3483.

(119) Kwon, Y.; Lum, Y.; Clark, E. L.; Ager, J. W.; Bell, A. T. CO2 Electroreduction with Enhanced Ethylene and Ethanol Selectivity by Nanostructuring Polycrystalline Copper. *ChemElectroChem* **2016**, *3*, 1012–1019.

(120) Barmparis, G. D.; Lodziana, Z.; Lopez, N.; Remediakis, I. N. Nanoparticle Shapes by Using Wulff Constructions and First-Principles Calculations. *Beilstein J. Nanotechnol.* **2015**, *6*, 361–368.

(121) Hodnik, N.; Zorko, M.; Bele, M.; Hočevar, S.; Gaberšček, M. Identical Location Scanning Electron Microscopy: A Case Study of Electrochemical Degradation of PtNi Nanoparticles Using a New Nondestructive Method. *J. Phys. Chem. C* **2012**, *116*, 21326–21333.

(122) Datye, A. K.; Xu, Q.; Kharas, K. C.; McCarty, J. M. Particle Size Distributions in Heterogeneous Catalysts: What Do They Tell Us about the Sintering Mechanism? *Catal. Today* **2006**, *111*, 59–67.

(123) Wynblatt, P.; Gjostein, N. A. Supported Metal Crystallites. *Prog. Solid State Chem.* **1975**, *9*, 21–58.

(124) Granqvist, C. G.; Buhrman, R. a. Size Distributions for Supported Metal Catalysts Coalescence Growth versus Ostwald Ripening. *J. Catal.* **1976**, *42*, 477–479.